

# On Wind and Roughness over Land

Jacobus Wouter Verkaik

**Promotor:**

Prof. dr. A. A. M. Holtslag    Hoogleraar in de  
meteorologie en luchtkwaliteit  
Wageningen Universiteit

**Samenstelling promotiecommissie:**

Dr. A. C. M. Beljaars	European Centre for Medium-Range Weather Forecasts, Engeland
Dr. F. C. Bosveld	KNMI, De Bilt
Prof. dr. P. Kabat	Wageningen Universiteit
Prof. dr. M. C. Krol	Wageningen Universiteit
Prof. dr. H. F. Vugts	Vrije Universiteit Amsterdam

# On Wind and Roughness over Land

## Wind en Ruwheid boven Land

Jacobus Wouter Verkaik

Proefschrift  
ter verkrijging van de graad van doctor  
op gezag van de rector magnificus  
van Wageningen Universiteit,  
Prof. dr. M. J. Kropff,  
in het openbaar te verdedigen  
op dinsdag 25 april 2006  
des namiddags te vier uur in de Aula.

ISBN 90-8504-385-9

# Dankwoord

Mijn promotie, die 1994 begon, is in 2006 dan toch nog tot een einde gekomen. Wat een tijd! Zowel thuis als op de vakgroep als op het KNMI is ondertussen heel wat gepasseerd. Er zijn veel mensen aan wie dank verschuldigd ben dat ik er aan heb kunnen beginnen, en dat ik uiteindelijk heb kunnen doorzetten.

Allereerst Jolanda die in mij de inspiratie en motivatie weer naar boven bracht en me veel ruimte heeft gegeven. Mijn ouders wil ik bedanken voor alle support en de mogelijkheden die zij voor mij geschapen hebben om te studeren.

Ik wil Prof. Jon Wieringa bedanken voor de aanstelling in Wageningen en de introductie die hij me heeft gegeven in zijn netwerk. Ik wil Prof. Bert Holtslag bedanken voor het overnemen van de begeleiding en alle stimulerende discussies.

Het waren zeker niet de makkelijkste jaren van de Vakgroep meteorologie in Wageningen. Toch heb ik het er uitstekend naar mijn zin gehad. Dat komt voornamelijk door al die prettige mensen: mijn collega-promovendi Berenice Michels, Joost Nieveen en Bert Heusinkveld, Rushdi El-Kilani; eerder al de “grote” jongens en meisjes, Cor Jacobs, Bart van den Hurk, Anne Verhoef; en later ook de jonkies, Reinder Ronda, Wouter Meijninger en Bas van de Wiel (die uiteindelijk allemaal veel sneller gepromoveerd zijn dan ik); en de technici en staf Frits Antonysen, Kees van den Dries, Willy Hillen, Teun Jansen, Leo Kroon, Henk de Bruin, Michaël Saraber, Adrie Jacobs en Gerrie van de Brink.

Van het KNMI hebben met name Fred Bosveld, Gerard van de Vliet, Frans Renes en Sjaak Koster veel bijgedragen aan de meetcampagne. Aryan van Engelen heeft als hoofd van de Klimatologische Dienst mij de ruimte gegeven mijn proefschrift af te ronden in “de baas z’n tijd”.

Arjan van Dijk (destijds TU Delft) wil ik bedanken voor het gebruik van “zijn” windtunnel om daar de k-vanen in te testen.

Thanks to Charlotte Hasager who invited me a week to Risø (Denmark).

Shell heeft mijn ticket betaald naar het *12th symposium on boundary layers and turbulence* in Vancouver, Canada, juli 1997.

NWO betaalde mijn salaris gedurende de jaren in Wageningen (1994–1998).

Aan al deze mensen: **Veel, veel dank!**

Maar bovenal dank ik God, de Schepper, Vader van Jezus Christus, voor al deze dingen. Hem komt de eer toe voor alle goede dingen. Dingen waarop ik geen recht heb, maar toch heb gekregen. En Zijn goedheid en genade zijn nog steeds niet op.

Maar toen nam ik alles wat ik ondernomen had nog eens in ogeschouw, alles wat mijn moeizaam gezwoeg mij opgeleverd had, en ik zag in dat het allemaal maar lucht en najagen van wind was.

Prediker 2: 11 De nieuwe bijbelvertaling

# Abstract

The relation between wind, momentum flux, roughness and land-use in disturbed, non-homogeneous boundary layers is studied. Key questions are: “how is the roughness related to land-use?”, “how are wind and friction related to the upstream land-use and roughness?”, and “is Monin-Obukhov theory still useful over non-homogeneous terrain?”.

To address these questions wind profiles and momentum fluxes up to 180 m height were measured at the Cabauw tower in 1996. The K-Gill propeller vane (k-vane) was used as flux measuring device. Before installing it at Cabauw this instrument was intensively tested and analyzed. This was done using perturbation theory, wind tunnel tests, and a field comparison experiment. The k-vane’s response to a turbulent wind field is equal to that of a regular first-order sensor with a response length of 2.9 m. During the measurement campaign at Cabauw the k-vane and its electronics proved to be very vulnerable to atmospheric electricity and contamination.

The roughness in the Cabauw environment is determined from the wind speed profiles, the gustiness and the drag coefficient. The upper and lower part of the profile yield different roughness lengths, and so do the gustiness and the drag coefficients at different heights. The differences found are explained qualitatively by the difference in source area of the measurements and the inhomogeneities in the Cabauw environment. Within the range of the tower, the momentum and heat flux decrease significantly with height, so regular surface layer similarity relations may not apply. The dimensionless wind speed gradient is also influenced by distant roughness transitions. Nevertheless, when local scaling is applied, the wind speed gradient can still be described by the functions that apply in homogeneous surface layers, both in stable and unstable conditions.

To determine the roughness length at synoptic or climatological stations gustiness models can be used. The roughness information helps to interpret the wind speed data and to monitor the exposure of the station. The gustiness model that has been used for long at the Royal Netherlands Meteorological Institute (KNMI) was not suited for the modern digital recording techniques. A new gustiness model has been proposed. The differences between the old and the new model are assessed and evaluated using field cases.

The gustiness derived roughness lengths of the synoptic and climatological stations are used to validate a roughness map that is derived from a land-use map. The roughness map covers The Netherlands with a resolution of 0.5 km. This map is used as input to a downscaling method which corrects weather model wind forecasts for the influence of local roughness variations. The downscaling method is successfully validated using in situ wind measurements from an airport and the coastal zone.



# Contents

<b>Dankwoord</b>	<b>i</b>
<b>Abstract</b>	<b>ii</b>
<b>1 Introduction</b>	<b>1</b>
1.1 Wind matters . . . . .	1
1.2 Surface roughness and land-use . . . . .	2
1.3 Objectives and overview . . . . .	2
<b>2 Evaluation of the k-vane</b>	<b>5</b>
2.1 Introduction . . . . .	5
2.2 Instrument Description . . . . .	7
2.3 Interaction between Propeller and Vane Dynamics . . . . .	7
2.4 Wind Tunnel Experiments . . . . .	12
2.5 Field Comparison Experiment . . . . .	15
2.6 Evaluation of Instrument Response Errors . . . . .	18
2.7 Discussion . . . . .	21
2.8 Conclusions . . . . .	24
<b>3 Wind, momentum, and roughness at Cabauw</b>	<b>27</b>
3.1 Introduction . . . . .	27
3.2 Experiment . . . . .	28
3.3 Terrain description . . . . .	31
3.4 Data set . . . . .	32
3.5 Wind profiles and Fluxes . . . . .	34
3.6 Roughness lengths . . . . .	38
3.7 Discussion . . . . .	41
3.8 Summary and Conclusions . . . . .	43
<b>4 Evaluation of Two Gustiness Models</b>	<b>45</b>
4.1 Introduction . . . . .	45
4.2 Exposure correction . . . . .	47
4.3 Gustiness models . . . . .	48
4.4 Wieringa's gustiness analysis . . . . .	49
4.5 Beljaars's gustiness analysis . . . . .	51
4.6 Application of gustiness models . . . . .	56
4.7 Influence of atmospheric stability and blending height . . . . .	64
4.8 Conclusions . . . . .	66

<b>5</b>	<b>Downscaling of weather model forecasts</b>	<b>69</b>
5.1	Introduction . . . . .	69
5.2	Two-layer model of the ABL . . . . .	71
5.3	The roughness map . . . . .	73
5.4	Footprint model . . . . .	77
5.5	NWP-model data . . . . .	82
5.6	Verification . . . . .	84
5.7	Conclusions . . . . .	89
<b>6</b>	<b>Summary and Outlook</b>	<b>93</b>
6.1	Summary . . . . .	93
6.2	Outlook . . . . .	96
<b>A</b>	<b>Propeller Dynamics</b>	<b>99</b>
<b>B</b>	<b>Vane Dynamics</b>	<b>101</b>
<b>C</b>	<b>K-vane measurements at Cabauw</b>	<b>103</b>
C.1	Experimental Setup . . . . .	103
C.2	Data Acquisition . . . . .	103
C.3	Flow Distortion . . . . .	104
	<b>References</b>	<b>108</b>
	<b>Samenvatting</b>	<b>119</b>
	<b>Curriculum Vitae</b>	<b>123</b>

# Chapter 1

## Introduction

### 1.1 Wind matters

Wind is an important factor in daily life and weather forecasts give information on wind direction and strength to the general public. The planning of outdoor operations like aviation and navigation relies strongly on wind forecasts. The wind determines our experience of the ambient temperature (wind chill) as it increases ventilation. Moreover, the wind moves heat and pollutants from one place to another. So, the direction of the wind is strongly correlated with the weather type and air pollution level, especially in a coastal country like The Netherlands. Wind also provides power to mankind from the medieval windmills to modern wind farms. Wind can cause hazards as it whips up the waves or blows down trees or man-made constructions. The wind climate is in part responsible for the geomorphology of a region. Moreover, the long-term experience with the local wind climate has made man adapt to it. In modern society this process is formalized by means of assessments of extremes that cause particular risks, design wind speed for constructions, acceptable levels of wind nuisance in cities, wind power potential of specific locations, etc, etc. So, wind is a very important climate variable that can not be disregarded in every-day life.

Wind is moving air. The mechanisms that cause the air to move on global scales are air pressure differences and the rotation of the Earth. Large-scale pressure differences are caused by temperature differences. These temperature differences in turn are caused by the difference in warming by the sun between the equator and the poles. The rotation of the Earth prohibits that air simply flows from high- to low-pressure regions (Coriolis force). Instead, the wind moves around low-pressure areas (depressions) in wide circles. In the northern hemisphere the wind circles into depressions in counter-clockwise direction. By transporting heat from the equator to the poles depressions reduce the temperature gradient from the equator to the poles. On smaller scales wind can be generated by other thermal circulations such as sea breeze, valley winds, etc.

Close to the Earth's surface the wind is decelerated by friction and at the surface the wind will diminish completely. The atmospheric boundary layer (ABL) is the layer where the deceleration of the wind can be felt. Its height is mainly determined by the temperature gradient in the lower atmosphere (stability) and the roughness of the surface. In windy conditions however, roughness is most important. The layer where roughness is important can range from 50 m in stable conditions to  $\sim 1$  km in unstable conditions.

As the wind speed decreases through the ABL, the Coriolis force becomes smaller. Consequently the wind will be moving into the depression more and more instead of circling

around it. This means that the wind direction turns (it backs in the northern hemisphere) when descending through the boundary layer. The part of the ABL where the wind direction turns is often called the Ekman-layer. In the lowest part of the ABL the wind speed decreases rapidly when going down but there is no significant turning in wind direction. This part of the ABL is often called the surface layer. So the ABL can be represented by two layers: close surface there is a surface layer and on top of that is the Ekman-layer.

It is very important to many human activities to know the wind speed in the surface layer since at this level the wind exerts loads on (man made) structures, drifts ships and aircrafts, causes waves and water set-up, transports gases and aerosols, etc.

## 1.2 Surface roughness and land-use

The deceleration of the wind speed close to the surface is caused by the surface roughness. No matter how rough or smooth the surface is, the wind speed will always be close to zero at the surface and will approach its maximum value at the top of the ABL. The roughness, however, determines the rate at which the wind speed increases through the surface layer. So, the wind speed can differ significantly at 10-m height over surfaces with different roughness, while at 200 m height the wind speed over those surfaces can be closely the same.

In most areas large roughness changes can be found over relatively short distances. Consequently, there will also be large wind speed differences. For example, on the downwind side of a lake there will considerably more wind than on the upwind side. The depth of the layer adapted to the low surface roughness on the downwind side can be very small, however. The layer that is influenced by the new surface roughness is approximately ten times as small as the upwind fetch, and the layer that is fully adapted to the new roughness is approximately one hundred times as small as the upwind fetch (Bradley, 1968; Rao et al., 1974). This shows that it is necessary to know the surface roughness of the upstream fetch over a considerable distance to make an estimate of the local wind speed profile.

Roughness does not only decelerate the wind, it also causes turbulence. Turbulence strongly enhances the vertical transport (flux) of heat, moisture, and any substances contained in the air from or to the surface of the Earth. Although these processes takes place in a shallow layer at the surface, they are of major importance to weather, climate, and atmospheric chemistry (Sud et al., 1988).

Roughness can be expressed in the *roughness length*  $z_0$ . Among the smoothest surfaces are sea, sand and snow ( $z_0 \approx 10^{-4}$  m); the roughest surfaces can be found in city centers ( $z_0 \approx 1-2$  m) (Wieringa, 1993). The area-averaged roughness is increased by the number of roughness transitions (Schmid and Bünzli, 1995). So an area comprising 50% grass land and 50% woods will be rougher if the size of the lake and wood patches is smaller.

## 1.3 Objectives and overview

The relation between wind, roughness, and friction under different conditions of stability has been well established in the Monin-Obukhov (MO) similarity theory in the early '70s (Businger and Yaglom, 1971; Obukhov, 1971). The MO-theory was developed assuming spatial homogeneity and constant heat- and momentum fluxes (Garratt and Hicks, 1990; Kaimal and Wyngaard, 1990). However, homogeneous surfaces are very rare in the natural environment. Even over seemingly homogeneous locations heat and moisture fluxes may be

heterogeneous because of the inhomogeneous distribution of precipitation or soil moisture (Mahrt, 1996). The relation between land-use, roughness, fluxes, and wind over non-homogeneous terrain is still a subject of study today (Philip, 1997; De Jong et al., 1999; Mahrt et al., 2001; Baldauf and Fiedler, 2003; Kljun et al., 2004; Dellwik and Jensen, 2005). This thesis is also in that line. The key questions are: “how is the surface roughness related to land-use?”, “how are wind and friction related to the upstream land-use and roughness?”, and “is MO-theory still useful over non-homogeneous terrain?”.

The initial basis of the research project described in this thesis is a measurement campaign done in 1996 at Cabauw in the Netherlands. At Cabauw the Royal Netherlands Meteorological Institute (KNMI) operates a 213-m high meteorological tower (Monna and Van der Vliet, 1987; Van Ulden and Wieringa, 1996). Routine measurements are taken of the wind, temperature, and moisture profiles, as well as all kinds of surface fluxes. During the measurement campaign additional instruments were installed at three heights to measure the momentum and heat flux. The K-Gill propeller vane was used for this purpose. An extensive evaluation of the K-Gill propeller vane was conducted before the instruments were installed at Cabauw (Chapter 2). The results of this campaign have been analyzed and compared to studies previously done at Cabauw (Chapter 3). This is done by estimating the roughness length using various methods: from profiles, momentum flux measurements, and drag coefficients. The results are evaluated as function of wind direction. This is useful at Cabauw since the environment is not uniform in all directions.

Chapter 4 and 5 deal with the interpretation and estimation of local wind speed. Measurements of surface wind speed are strongly influenced by the terrain upstream of the measuring location. Two closely situated anemometers may report distinctively different wind speeds as the result of differences in the upstream land-use. This is a serious problem when doing a wind climate assessment based on surface measurements. However, if the upstream roughness can be determined, the influence of differences in roughness can be removed from the measurements. A clever way to determine the roughness at the measuring site is by doing an analysis of the gustiness. The gustiness reflects the changes in roughness as function of direction and time. Gustiness analysis has been used for many years at KNMI to correct measured wind speeds (Wieringa, 1976). However, new measuring techniques compelled the introduction of a different gustiness model (Beljaars, 1987a). To ensure that the introduction of a new gustiness model does not result in a discontinuity in the corrected wind speed the old and the new gustiness model have been compared (Chapter 4).

Current numerical weather prediction (NWP) models do not represent details of the flow or the surface smaller than  $\sim 10$  km. This implies that the wind speed in NWP-models is constant over boxes of  $(10 \text{ km})^2$ . Actually within such boxes numerous different types of land-use can be present, involving differences in roughness and wind speed. Satellite-derived information on land-use is nowadays available down to a resolution of  $\sim 10$  m. These data can be used to construct high-resolution roughness maps. Chapter 5 describes a method how this can be done and how NWP-model winds can be corrected using the high-resolution roughness map.

A summary and outlook are given in Chapter 6.



# Chapter 2

## Evaluation of the K-Gill Propeller Vane

Published in *Journal of Atmospheric and Oceanic Technology* **15**, p. 901–915, 1998.

### Abstract

Dynamic properties of the K-Gill Propeller Vane (k-vane) are assessed from perturbation theory, wind tunnel, and field comparison experiments. Measurement errors for average wind speed are negligible. The dynamic response of the k-vane can be described with a single response length that is the propeller's distance constant at  $45^\circ$  angle of attack. Measurement errors in longitudinal and vertical wind speed variances and the momentum flux due to propeller inertia can be described and corrected for as if the k-vane were a simple first-order system. Standard spectra as well as spectra measured by the k-vane itself can be used to calculate correction coefficients. In the latter case no information on atmospheric stability and boundary layer height is necessary. Transfer of lateral wind speed variance can be described as if the k-vane were a damped harmonic oscillator. Measurement errors in lateral wind speed variance, however, are usually negligible because loss of high-frequency variance is compensated by amplification of variance at the natural wavelength of the vane.

The propeller's distance constant and the vane's natural wavelength derived from the field comparison experiments are both smaller than those derived from the wind tunnel experiments. When the k-vane is used at elevated levels ( $z > 20$  m), however, measurement errors become small and the exact values of the distance constant and the natural wavelength become insignificant. Parameters derived from the field experiments for the 35301 model are a response length of 2.9 m, a natural wavelength of 7.8 m, and a damping ratio of 0.49. When the k-vane is used at levels higher than 20 m, the momentum flux lost due to instrument inertia will usually be less than 10%. This means that the k-vane is a suitable sensor for flux measurements on tall masts.

### 2.1 Introduction

The K-Gill Propeller Vane (k-vane) is an anemometer for measuring turbulent fluxes as well as mean flow properties. The k-vane consists of two propellers—one oriented  $45^\circ$  upward, the other  $45^\circ$  downward—that are aligned into the mean wind direction by a vane. From the angular velocities of the propellers, horizontal and vertical wind speed components can be calculated. From the instantaneous values of the horizontal and vertical wind speed, momentum fluxes can be calculated using the eddy correlation method. Advantages of this

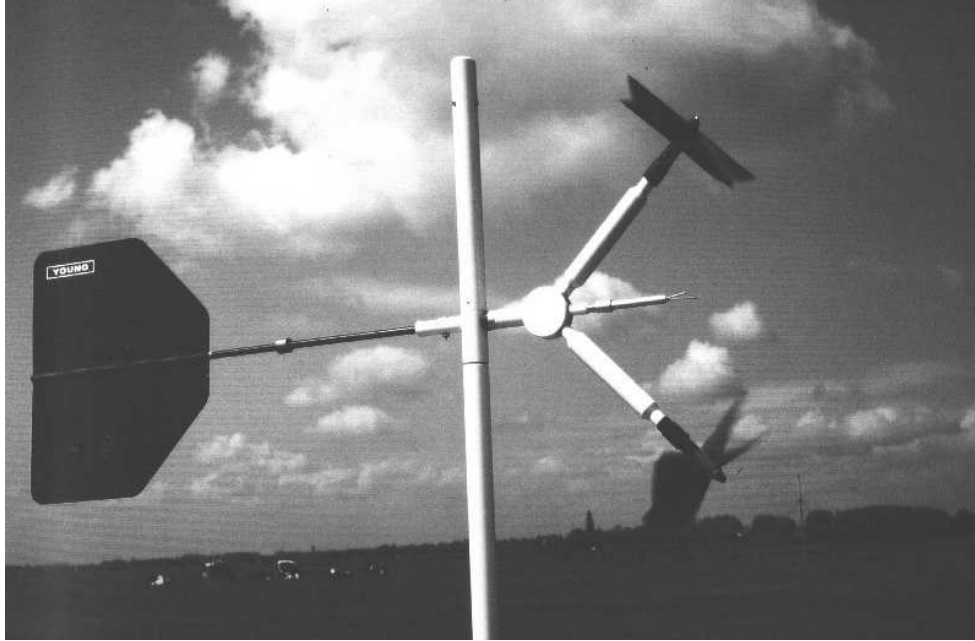


Figure 2.1: Picture of the K-Gill Propeller Vane.

design above its precursors, for example the Gill UVW system (Gill, 1975) or twin propeller-vane anemometers with a horizontal and a downward-looking propeller used earlier (Large and Pond, 1981; Large and Pond, 1982; Ataktürk and Katsaros, 1987), are (a) its symmetry for up- and downdrafts, (b), the propellers are operating at moderate angles of attack, so the cosine response is well defined and no stalling of the propellers occurs, and (c) there is no need to align the instrument in the mean wind direction. Extension of the main shaft above the pivot of the vane and propeller mounting has improved symmetry even more. A similar design has been presented by Desjardins et al. (1986), but the k-vane anemometer in its present form was first introduced by Ataktürk and Katsaros (1989). So far the k-vane has been used mainly to measure momentum fluxes over sea (Katsaros et al., 1987; Katsaros et al., 1993).

The k-vanes discussed in this paper are used in a research project concerning turbulent fluxes of momentum and sensible heat in the atmospheric boundary layer over heterogeneous terrain (Verkaik, 1997). Six k-vanes have been installed at three levels (20, 100, and 180 m) at the 213 m meteorological mast of the Royal Netherlands Meteorological Institute (KNMI) at Cabauw (Van Ulden and Wieringa, 1996). In this project k-vanes were preferred above for example sonic anemometers because the latter fail to operate in rain, wet snow, and heavy fog (Wyngaard, 1981a). Since our purpose was to operate continuously at Cabauw for at least a year, we could not consider using fair-weather instruments. Another operational advantage of the k-vane is that it does not need to be pointed into the wind, as is the case with many sonics.

One copy of model 35301 and seven copies of a special model 35301DTX (manufactured by R. M. Young Co., United States) have been tested in the wind tunnel. The 35301 model has also been tested in a field comparison experiment. The 35301 will be referred to as the “old” k-vane and the 35301DTX as the “DTX”.

The propellers and vane all have limited response times, so measurement errors can be expected when the k-vane is exposed to high-frequency turbulence. In the present article the magnitude of the errors due to k-vane inertia is assessed by perturbation theory,

wind tunnel, and field experiments. Based on the spectral behaviour of the k-vane, simple methods are presented to correct for instrument inertia.

## 2.2 Instrument Description

The total height of the k-vane (see Figure 2.1), including the base and extension tube, is 1.01 m, the distance from the top of the base (diameter 0.16 m) to the vane arm and propeller mounting is 0.60 m. The diameter of the main shaft is 29 mm, while the minimum distance from the main shaft to the propellers is 0.18 m. The vane arm extends 0.40 m from the main shaft and the vane dimensions are 0.30 m  $\times$  0.36 m. Sturdy carbon fibre thermoplastic (CFT) propellers are used (diameter 0.20 m, pitch 0.30 m).

Model 35301DTX is a slightly different version of model 35301. The original shafts of the propellers and vane have been replaced by stronger ones, the mounting of the propellers has been modified to ensure a 90° angle between the two propellers, and additional electric wires have been inserted to enable us to place thermocouple electronics in the extension tube above the pivot of the vane. We extended our k-vanes with electrolytic level sensors (Inclinometer NB3, AE Sensors, the Netherlands) and thermocouples. The level sensor can be used to correct for alignment errors, and the thermocouple enables the k-vane to measure sensible heat fluxes. We first intended to mount the level sensor at the beginning of the vane arm. This resulted in an erroneous reading of the level sensor since vane movements generate centripetal accelerations. A solution to this problem was found in mounting the level sensor inside the top of the extension tube on the axis of the main shaft.

## 2.3 Interaction between Propeller and Vane Dynamics

Propellers and vanes have been used for many years in meteorology and many articles have been devoted to their dynamical properties. Propeller dynamics, (appendix A) and vane dynamics (appendix B) relevant to the k-vane are briefly summarized. In this section the interaction between propeller and vane dynamics of the k-vane will be discussed.

### 2.3.1 K-vane Response to a Turbulent Wind Field

An excellent analysis of the interaction of propeller and vane dynamics for a propeller vane in a turbulent wind field was given by Zhang (1988). From perturbation theory he found an expression for the over- or underspeeding of the propeller vane in terms of propeller and vane parameters and turbulent wind velocity spectra. In this section the analysis will be extended so that it can also be applied to the k-vane. The overspeeding error, artificial vertical wind speed, and measured (co-)variances will be expressed in terms of the k-vane's propeller and vane parameters and spectra of atmospheric turbulence.

The propeller response equations, Eqs. A.2 and A.3, can be written as

$$S = c \omega \gamma_R R = \frac{c}{k} (VC(\psi) \cos \psi - \Delta u_f) = K (VC(\psi) \cos \psi - \Delta u_f), \quad (2.1)$$

where  $S$  is the output generated by the propeller and has dimension  $[c] \times \text{m s}^{-1}$ .  $\gamma_R$  and  $R$  are the propeller's pitch factor and radius and  $\omega$  is its angular velocity.  $V$  is the total

wind vector;  $C(\psi)$  is the cosine response function, where  $\psi$  is the angle of attack;  $\Delta u_f$  is the correction;  $K$ ,  $k$ , and  $c$  are calibration constants. The mean angle of attack of the wind on the k-vane propellers  $\psi = 45^\circ$ . When linearized at  $\psi = 45^\circ$ , Eq. A.4 yields

$$C(\psi) = C_0 - C_1 \Delta\psi = 0.83 - 0.3 \Delta\psi. \quad (2.2)$$

The accuracy of Eq. 2.2 is better than 3% when  $|\Delta\psi| < 15^\circ$ . When  $\bar{U}$  is along the positive  $x$ -axis, the angle of attack for the top propeller  $\psi_{\text{top}}$  is given by

$$|T| |V| \cos \psi_{\text{top}} = \mathbf{T} \mathbf{V}, \quad \mathbf{T} = \frac{1}{\sqrt{2}} \begin{pmatrix} \cos \beta' \\ \sin \beta' \\ -1 \end{pmatrix}, \quad \mathbf{V} = \begin{pmatrix} U + u' \\ v' \\ w' \end{pmatrix}, \quad (2.3)$$

where  $\beta$  is the direction of the vane measured from the positive  $x$ -axis and  $\vec{T}$  is a unit vector parallel to the propeller axis. Here  $U$  is the average wind speed and  $u'$ ,  $v'$ , and  $w'$  are turbulent wind speed fluctuations with zero average. Retaining only terms up to the second order, the angle of attack for the top propeller in a turbulent wind field can be written as

$$\Delta\psi_{\text{top}} = \psi_{\text{top}} - \pi/4 = \frac{w'}{U} - \frac{u'w'}{U^2} - \phi'\beta' + \frac{(\beta')^2 + (\phi')^2}{2}, \quad (2.4)$$

where  $\phi' = v'/U$ . For the bottom propeller only the sign of  $w'$  changes. From Eqs. 2.3 and 2.4 the along-axis wind component can be derived. Again, retaining only terms up to the second order this component equals

$$u_{\beta, \text{top}} = |V| C(\psi_{\text{top}}) \cos \psi_{\text{top}} = C(\psi_{\text{top}}) \vec{T} \cdot \vec{V} = \frac{C_0 U}{\sqrt{2}} \left[ 1 + \frac{u' - aw'}{U} + a\Lambda - \frac{C_1}{C_0} \left( \frac{(\phi')^2}{2} - \frac{(w')^2}{U^2} \right) \right], \quad (2.5)$$

where  $\Lambda = \phi'\beta' - (\beta')^2/2$  and  $a = 1 + C_1/C_0$ . Averaging this equation results in

$$\overline{u_{\beta, \text{top}}} = \frac{C_0 U}{\sqrt{2}} \left( 1 + a\bar{\Lambda} - \frac{C_1 \sigma_\phi^2}{C_0 2} + \frac{C_1 \sigma_w^2}{C_0 U^2} \right), \quad (2.6)$$

where  $\bar{\Lambda}$  represents the “ $v$ -error”. The positive correlation  $\overline{\phi'\beta'}$ , which may cause propeller vanes to overspeed due to vane motion, was overlooked by MacCready (1966). From Eqs. 2.5 and 2.6 it can be shown that

$$u'_{\beta, \text{top}} = \frac{u_{\beta, \text{top}} - \overline{u_{\beta, \text{top}}}}{\overline{u_{\beta, \text{top}}}} = \frac{u' - aw'}{U} + a(\Lambda - \bar{\Lambda}) - \frac{C_1}{C_0} \left( \frac{(\phi')^2 - \sigma_\phi^2}{2} - \frac{(w')^2 - \sigma_w^2}{U^2} \right). \quad (2.7)$$

Zhang (1988) derived the following expressions for the propeller response  $S$ :

$$\frac{D}{u_\beta} \frac{dS}{dt} = K(u_\beta - \Delta u_f) - S, \quad (2.8)$$

$$S = S_\beta (1 + s') = K(\overline{u_\beta} - \Delta u_f) (1 + s'), \quad (2.9)$$

$$\tau \frac{ds'}{dt} + s' = (1 + \epsilon) u'_\beta - s' u'_\beta + (1 + \epsilon) u'^2_\beta, \quad (2.10)$$

where  $\epsilon = \Delta u_t / \bar{u}_\beta$  and  $\tau = D / \bar{u}_\beta$ . Here  $D$  is the propeller's distance constant. Inserting Eqs. 2.7 in 2.10, neglecting  $\epsilon$ , and retaining only terms up the second order results in

$$\tau \frac{ds'_{\text{top}}}{dt} + s'_{\text{top}} = \left(1 - s'_{\text{top}} + \frac{u' - aw}{U}\right) \left(\frac{u' - aw'}{U}\right) + a(\Lambda - \bar{\Lambda}) - \frac{C_1(\phi')^2 - \sigma_\phi^2}{C_0} + \frac{C_1(w')^2 - \sigma_w^2}{C_0 U^2}. \quad (2.11)$$

For the bottom propeller again only the sign of  $w'$  changes. Averaging Eq. 2.11 yields correlations between  $s'$  and  $u'$  and between  $s'$  and  $w'$ . Evaluation of  $s'u'$  and  $s'w'$  starts with the approximation of Eq. 2.11, using first-order terms only

$$\tau ds'/dt + s' = u'/U - aw'/U. \quad (2.12)$$

Following the same procedure Busch and Kristensen (1976) used for the determination of cup anemometer overspeeding, we find

$$\overline{s'u'_{\text{top}}} = \frac{\sigma_u^2}{U} \int_0^\infty \frac{S_u(\omega)}{1 + (\omega\tau)^2} d\omega - a \frac{\overline{u'w'}}{U} \int_0^\infty \frac{C_{uw}(\omega)}{1 + (\omega\tau)^2} d\omega, \quad (2.13)$$

and

$$\overline{s'w'_{\text{top}}} = \frac{\overline{u'w'}}{U} \int_0^\infty \frac{C_{uw}(\omega)}{1 + (\omega\tau)^2} d\omega - a \frac{\sigma_w^2}{U} \int_0^\infty \frac{S_w(\omega)}{1 + (\omega\tau)^2} d\omega. \quad (2.14)$$

Here  $S_u$  and  $S_w$  are the variance spectra of  $u'$  and  $w'$  and  $C_{uw}$  is the co-spectrum of  $u'w'$ . The spectra are normalized so that  $\int_0^\infty S_{u,w}(\omega) d\omega = \int_0^\infty C_{uw}(\omega) d\omega = 1$ . Again for the bottom propeller only the sign of the second term in Eqs. 2.13 and 2.14 changes. The following expressions can now be derived from Eqs. 2.11, 2.13, and 2.14:

$$\overline{(s'_{\text{btm}} - s'_{\text{top}})^2} = 4a^2 \frac{\sigma_w^2}{U^2} \int_0^\infty \frac{S_w(\omega) d\omega}{1 + \tau^2 \omega^2}, \quad (2.15)$$

$$\overline{s'_{\text{btm}}} + \overline{s'_{\text{top}}} = 2 \frac{\sigma_u^2}{U^2} \left(1 - \int_0^\infty \frac{S_u(\omega) d\omega}{1 + (\omega\tau)^2}\right) \quad (2.16)$$

$$+ 2a^2 \frac{\sigma_w^2}{U^2} \left(1 - \int_0^\infty \frac{S_w(\omega) d\omega}{1 + (\omega\tau)^2}\right). \quad (2.17)$$

Instead of averaging the total horizontal wind speed and wind direction, the instantaneous horizontal wind speed and direction are decomposed in eastward and northward wind components. Rotation of  $\bar{v}'$  and  $\bar{w}'$  to zero can be done after a measurement interval has been completed. So the wind speed in the  $x$ -direction indicated by the k-vane is given by

$$U_m = U(1 + \delta) = \cos \beta' \cos \Delta\psi^\infty |V_m|, \quad (2.18)$$

where  $\Delta\psi^\infty$  is the measured inclination of the wind vector and  $\delta$  is the overspeeding error. Here  $|V_m|$  is the measured total wind speed,

$$V_m^2 = \left(\frac{S_{\text{top}}}{K(C_0 - C_1 \Delta\psi^\infty)}\right)^2 + \left(\frac{S_{\text{btm}}}{K(C_0 + C_1 \Delta\psi^\infty)}\right)^2. \quad (2.19)$$

The inclination of the wind vector  $\Delta\psi^\infty$  is calculated from the measured  $s'_{\text{btm}}$  and  $s'_{\text{top}}$ . To correct the measured responses for cosine response,  $\psi_{\text{btm}}$  and  $\psi_{\text{top}}$  must be known. Using an iterative process described by Ataktürk and Katsaros (1989)  $\Delta\psi^\infty$  can be solved. A necessary assumption to solve  $\Delta\psi^\infty$  is  $\Delta\psi_{\text{btm}} = -\Delta\psi_{\text{top}}$  or  $\psi_{\text{top}} + \psi_{\text{btm}} = \pi/2$ , which is only true when  $\phi' = \beta'$ . From Eq. 2.4 note that generally  $\psi_{\text{top}} + \psi_{\text{btm}} > \pi/2$ . This will result in two different errors: The total wind is not correctly decomposed in vertical and horizontal parts, and the cosine response correction is applied using a smaller angle of attack, resulting in an overestimation of the wind speed. From a first guess of  $\Delta\psi^{(1)}$  ( $= 0$ ) the next step of the iteration yields  $\Delta\psi^{(2)}$ :

$$\tan\left(\frac{\pi}{4} + \Delta\psi^{(2)}\right) = \frac{s'_{\text{btm}}}{1 + C_1/C_0\Delta\psi^{(1)}} \frac{1 - C_1/C_0\Delta\psi^{(1)}}{s'_{\text{top}}}.$$

Retaining only terms of the first order, this can be simplified to

$$\Delta\psi^{(2)} = \frac{1}{2}(s'_{\text{btm}} - s'_{\text{top}}) - \frac{C_1}{C_0}\Delta\psi^{(1)}.$$

The result of the iterative process will be

$$\Delta\psi^\infty = \frac{1}{2}(s'_{\text{btm}} - s'_{\text{top}}) \sum_{n=0}^{\infty} \left(-\frac{C_1}{C_0}\right)^n = \frac{s'_{\text{btm}} - s'_{\text{top}}}{2a}. \quad (2.20)$$

For fast propeller response ( $\omega\tau \ll 1$ ) this equation yields  $\Delta\psi^\infty = w'/U$ .

From Eqs. 2.6, 2.9, 2.19 and 2.20,  $V_m$  can now be calculated:

$$\begin{aligned} \frac{V_m}{U} = 1 + \frac{s'_{\text{btm}} + s'_{\text{top}}}{2} - \frac{(s'_{\text{btm}} + s'_{\text{top}})^2}{8} + \\ \frac{1}{4} \left(s'_{\text{btm}} - \frac{C_1}{C_0}\Delta\psi^\infty\right)^2 + \frac{1}{4} \left(s'_{\text{top}} + \frac{C_1}{C_0}\Delta\psi^\infty\right)^2 + \\ \frac{C_1}{2C_0}s'_{\text{top}}\Delta\psi^\infty - \frac{C_1}{2C_0}s'_{\text{btm}}\Delta\psi^\infty + \frac{C_1}{C_0}\frac{\sigma_w^2}{U^2} + \frac{C_1^2}{C_0^2}\frac{\sigma_w^2}{U^2} + a\bar{\Lambda} - \frac{C_1}{C_0}\frac{\sigma_\phi^2}{2}. \end{aligned} \quad (2.21)$$

Now  $\delta$  can be calculated from Eqs. 2.18 and 2.21:

$$\delta = \frac{s'_{\text{btm}} + s'_{\text{top}}}{2} + \frac{C_1}{C_0} \left( \frac{\sigma_w^2}{U} - \frac{(s'_{\text{btm}} - s'_{\text{top}})^2}{4a^2} \right) + a\bar{\Lambda} + \frac{C_1}{C_0}\frac{\sigma_\phi^2}{2} - \frac{(\beta')^2}{2}. \quad (2.22)$$

Averaging this equation yields [using Eqs. 2.16 and 2.15]

$$\begin{aligned} \bar{\delta} = \frac{\sigma_u^2}{U^2} \left(1 - \int_0^\infty \frac{S_u(\omega)d\omega}{1 + (\omega\tau)^2}\right) + \left(a^2 + \frac{C_1}{C_0}\right) \frac{\sigma_w^2}{U^2} \left(1 - \int_0^\infty \frac{S_w(\omega)d\omega}{1 + (\omega\tau)^2}\right) \\ - \frac{C_1}{2C_0}\sigma_\phi^2 \left(1 - \int_0^\infty \frac{1 - 2a/(a-1)(\omega/\omega_0)^2}{(1 - \omega^2/\omega_0^2)^2 + 4\zeta^2\omega^2/\omega_0^2} S_v(\omega)d\omega\right). \end{aligned} \quad (2.23)$$

The first term and the first part of the second term in Eq. 2.23 represent the propeller overspeeding; the second part of the second term is the result of the discrepancy between the measured and real (instantaneous) inclination angle. The real wind inclination is

usually larger than the measured inclination. Inclination of the wind vector will reduce the angle of attack on one propeller while increasing the angle of attack on the other. However, the increase in response of the former is larger than the decrease in response of the latter. So, the net effect will lead to an *increase* in the jointly measured horizontal wind speed. The correction to the total wind speed, which is applied using the measured inclination angle, is largest at zero inclination. When the inclination angle is underestimated, propeller responses are corrected using a too-large correction, resulting in an overspeeding error. The third term in Eq. 2.23 represents the total  $v$ -error. It is smaller than that derived by (Zhang, 1988) since decomposition of wind speed into horizontal components is done before averaging. In case of an infinitely fast propeller vane response, so that  $\omega\tau \ll 1$  and  $\beta' = \phi'$ ,  $\delta$  equals zero.

For the measured vertical wind speed, Eq. 2.18 changes to

$$\frac{w_m}{U} = \eta = \sin \Delta\psi^\infty \frac{|V_m|}{U} = \frac{s'_{\text{btm}} - s'_{\text{top}}}{2a} + \frac{(s'_{\text{btm}})^2 - (s'_{\text{top}})^2}{4a},$$

which yields after averaging

$$\bar{\eta} = \frac{\overline{u'w'}}{U^2} \left( 1 - \int_0^\infty \frac{C_{uw}(\omega)d\omega}{1 + (\omega\tau)^2} \right). \quad (2.24)$$

Note that  $\eta$  is always negative. Using the measured momentum flux we can write

$$-u_{*m}^2/U^2 = \overline{(U_m - \bar{U}_m)(w_m - \bar{w}_m)}/U^2 = \bar{\delta}\bar{\eta} - \bar{\delta}\bar{\eta}. \quad (2.25)$$

Evaluating this equation, all terms higher than the first in  $\delta$  and  $\eta$  can be neglected since no spectra higher than the second order are available. Equation 2.25 then yields

$$\frac{-u_{*m}^2}{U^2} = \frac{\overline{u'w'}}{U^2} \int_0^\infty \frac{C_{uw}(\omega)d\omega}{1 + (\omega\tau)^2}, \quad (2.26)$$

which is the regular first-order transfer function. In the same way the measured longitudinal and vertical wind speed variance can be expressed as

$$\frac{\sigma_{um}^2}{U^2} = \bar{\delta}^2 - \bar{\delta}^2 = \frac{\sigma_u^2}{U^2} \int_0^\infty \frac{S_u(\omega)d\omega}{1 + (\omega\tau)^2} \quad (2.27)$$

and

$$\frac{\sigma_{wm}^2}{U^2} = \bar{\eta}^2 - \bar{\eta}^2 = \frac{\sigma_w^2}{U^2} \int_0^\infty \frac{S_w(\omega)d\omega}{1 + (\omega\tau)^2}. \quad (2.28)$$

So for all variances the regular first order transfer function applies with a response length equal to the distance constant of the propeller at  $45^\circ$  angle of attack. The transfer of lateral wind speed variance is given by Eq. B.4.

### 2.3.2 Gyroscopic Stability Propellers

Wieringa (1967) and Busch et al. (1980) mention the possibility of the angular momentum of the propeller ( $L$ ) to be responsible for the gyroscopic stability of the vane. This applies,

however, only to propeller vanes that can swivel in two directions, which are called trivanes. For vanes that can rotate only about a single axis, gyroscopic stability of propellers is not possible, as will be explained below.

Vane movements will alter the direction of  $L$ , so  $dL/dt$  is in the horizontal plane. Therefore, forces that are induced by azimuthal movements act in the elevation direction on the propeller axis. The propeller vane or k-vane axis cannot be elevated. Azimuthal movements of trivanes, however, can change elevation angles and vice versa.

The only way gyroscopic stability could possibly influence vane dynamics is by increased friction, as a result of the torque, on the bearings that support the vane. However, these torques will be small compared to other torques on the vane. For  $U = 12.5 \text{ m s}^{-1}$  the k-vane propellers will rotate at  $150 \text{ rad s}^{-1}$ . To assess the moment of inertia of the propeller, a tiny load has been attached to the tip of one of the blades and then the period of oscillation has been determined. The moment of inertia found this way equals  $8.6 \times 10^{-5} \text{ kg m}^2$ . The angular momentum of the two propellers  $\vec{L}_{\text{prop } 1} + \vec{L}_{\text{prop } 2} = 1.8 \times 10^{-2} \text{ kg m}^2 \text{ s}^{-1}$ . Typical angular velocity of the vane equals  $0.75 \text{ rad s}^{-1}$ . So the torque on the propeller axis is  $1.4 \times 10^{-2} \text{ N m}$ . The torque on the vane blade at  $3^\circ$  from equilibrium equals  $0.4 \text{ N m}$  at this wind speed. So, in general, torques from gyroscopic stability are very small compared to torques on the vane blade; however, those torques are perpendicular. In the case of the k-vane, the torque by drag on the extension tube is probably much larger.

## 2.4 Wind Tunnel Experiments

### 2.4.1 Propeller Tests

The author has tested the CFT propellers (model 08254) in the wind tunnel of the Department of Meteorology of the Wageningen Agricultural University (WAU). This wind tunnel has an octagonal working section with a length of  $0.4 \text{ m}$  and a radius of  $0.2 \text{ m}$  (Monna, 1983). So it is just large enough to do propeller tests (radius  $0.1 \text{ m}$ ).

Step changes in wind speed were used to determine the propeller's response length. To perform step-down tests without significantly disturbing the mean flow, a fine cotton wire was wound round the propeller shaft. By pulling the wire the propeller was sped up like a top. This way propeller velocities of  $4 \text{ m s}^{-1}$  could be achieved. When the propeller is sped up in reverse direction, the same procedure can be used for step-up tests. Equation A.5 has been fitted to the measured response to determine the response time. Only the tail of the response curve, after 60% adaption, has been used.

Results are summarized in Figure 2.2. The response time  $\tau$  is plotted as function of  $U_\infty$ . The solid line corresponds to  $\tau = D/U_\infty$  with  $D = 3.0 \text{ m}$ , the overall average. From this figure it is clear that for small  $U_\infty$ 's,  $\tau$  is less than would be expected from  $D = 3 \text{ m}$  for both the step-up and step-down tests. The dashed curve gives the relative decrease of  $D$  for step-up tests in percentages. For  $U_\infty < 4 \text{ m s}^{-1}$   $D$  decreases with 30%, so at low wind speeds the propeller responds quicker.

Response times for step-down tests seem to be smaller than for step-up tests;  $D$  for step-down tests equals about half the value of  $D$  for step-up tests when  $U < 2 \text{ m s}^{-1}$ . A possible explanation is the friction of the bearings. This will increase the deceleration of the propeller and decrease its acceleration. However, the step-down response at low wind speeds is not very well described by Eq. A.5 and the scatter of individual measurements is considerable.

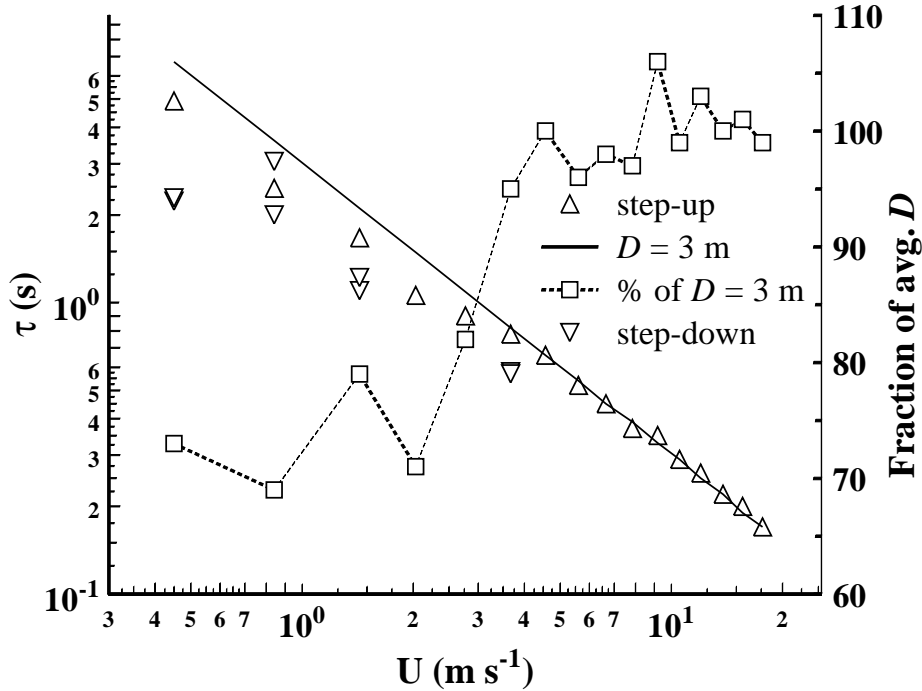


Figure 2.2: Dependence of  $D$  on  $U_\infty$ .

## 2.4.2 Vane Tests

### Determination of $\lambda_n$ and $\zeta$

The author has tested the k-vanes in the wind tunnel of Delft University of Technology, Faculty of Mechanical Engineering and Marine Technology, Laboratory for Aero- and Hydrodynamics. The open working section of this wind tunnel is 0.7 m in height, 0.9 m in width, and 1.6 m long. Vane tests were done with the propellers mounted on the k-vane. At several wind speeds the vane was given a deviation (less than  $15^\circ$ ) of its equilibrium position and then released. Vane and propeller responses were recorded using a Campbell 21X datalogger. This procedure was repeated twice for both back and veer wind deviations and for every k-vane used at Cabauw. Special care was given to the symmetry of the experimental setup since some k-vane tests suggested different response characteristics for back and veer wind.

Results are shown in Tables 2.2 and 2.1; standard deviations are given in parenthesis. The results have been evaluated by two methods. First, overshoot ratios and the time between successive overshoots have been determined. From Eq. B.6, the damping ratio  $\zeta$  can be calculated and the time between two successive overshoots multiplied by the wind speed equals the half damped wavelength ( $\lambda_d$ ). From this the natural wavelength ( $\lambda_n = \lambda_d \sqrt{1 - \zeta^2}$ ) can be calculated. Second, Eq. B.2 was fitted to the vane response by a least squares fitting procedure, and from this  $\lambda_n$  and  $\zeta$  were found. As can be seen from Tables 2.2 and 2.1, differences for back and veer wind were still found, but are not very significant. Not all k-vanes showed stronger damping for back wind deviations; some k-vanes showed equal response for both veer and back wind deviations. From this it can be concluded that asymmetric response is not caused by the wind tunnel but probably by the k-vane itself. However, no satisfactory explanation has been found for it.

Table 2.1: Vane properties model 35301DTX from wind tunnel tests.

		Overshoot		Least square method		Both	
Veer	$\lambda_n(\text{m})$	11	(2)	13	(1)	12	(2)
	$\zeta$	0.44	(0.09)	0.49	(0.09)	0.46	(0.09)
Back	$\lambda_n(\text{m})$	12	(3)	13	(1)	12	(2)
	$\zeta$	0.6	(0.1)	0.58	(0.09)	0.6	(0.1)
Both	$\lambda_n(\text{m})$	11	(2)	13	(2)	12	(2)
	$\zeta$	0.5	(0.1)	0.5	(0.1)	0.5	(0.1)

Table 2.2: Vane properties model 35301 from wind tunnel tests.

		Overshoot		Least square method		Both	
Veer	$\lambda_n(\text{m})$	13	(2)	13	(1)	13	(2)
	$\zeta$	0.48	(0.04)	0.51	(0.02)	0.50	(0.03)
Back	$\lambda_n(\text{m})$	15	(3)	12	(1)	14	(3)
	$\zeta$	0.58	(0.03)	0.59	(0.06)	0.58	(0.03)
Both	$\lambda_n(\text{m})$	14	(3)	13	(1)	13	(2)
	$\zeta$	0.53	(0.06)	0.55	(0.04)	0.54	(0.06)

### Torque on the vane as function of attack angle

The description of vane response as a damped harmonic oscillator is based on the assumption  $M = N\beta$ , where the torque  $M$  increases linearly with the angle of attack  $\beta$ . The validity of this assumption has been tested in a wind tunnel experiment. A fine cotton wire was attached to the end of the vane arm. Using a pulley and some little weights, a force could be applied to the vane arm. With the wind tunnel running at constant speed more weights were added. This procedure was repeated for two wind tunnel speeds ( $6.5 \text{ m s}^{-1}$  and  $10.1 \text{ m s}^{-1}$ ) and for two k-vanes. Results are shown in Figure 2.4. The ordinate is  $M/U^2$  and the abscissa is  $\beta$ . Two important features are clear from Figure 2.4. First,  $M/U^2$  does not increase linearly with  $\beta$ , rather a parabolic increase seem to fit the data. Second, in veer wind deviations (k-vane is turned in back wind direction),  $M/U^2$  increases faster compared to back wind deviations for these k-vanes. Dynamic tests of the same k-vane revealed slightly stronger damping for back wind deviations, which suggests the opposite.

From Figure 2.4 it seems there is a little offset in vane response for  $\beta > 0$ . If so, the vane would have an equilibrium position with  $\beta \neq 0$ . Regression results indicated only insignificant offsets, however. For  $\beta < 0$  least squares fitting yields  $M/U^2 = -(0.061 \pm 0.004)\beta$ , for  $\beta > 0$ ;  $M/U^2 = (0.045 \pm 0.003)\beta$ .

### Influence of propeller rotation on vane dynamics

To check empirically the theoretical considerations in section 2.3.2, vane response tests have been repeated with fixed propellers. In spite of the conclusion that no effect could be expected, there was a clear difference in vane response. Both  $\lambda_n$  and  $\zeta$  decreased to 9 (1) m and 0.43 (0.06), respectively, so the vane is indeed better damped when propellers

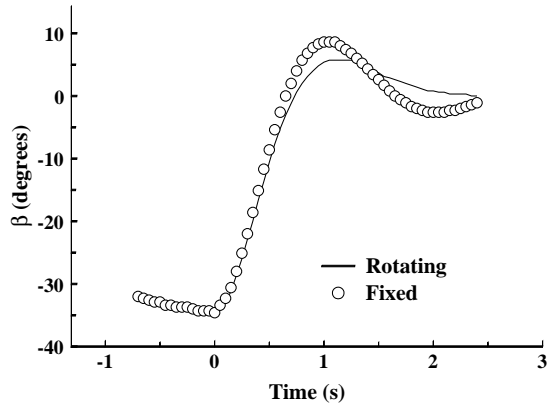


Figure 2.3: Influence of rotation propellers on vane-response.

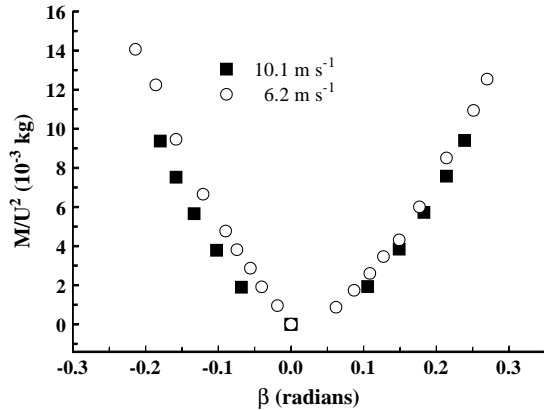


Figure 2.4:  $M/U^2$  as function of  $\beta$ .

are rotating. The same effect was observed earlier by (Wieringa, 1967). Scatter in  $\lambda_n$  is considerably less when propellers are fixed, especially using the least squares method. In Figure 2.3 the difference in response between fixed and rotating propellers can clearly be seen. When propellers are rotating, the vane is usually critically damped after the first overshoot. This behaviour cannot be described by Eq. B.2, which assumes equal overshoot ratios for successive overshoots. With propellers fixed the vane behaves much more in agreement with Eq. B.2 so the least squares method will be much more successful.

Flow distortion is certainly different with the propellers fixed than with propellers rotating or removed. The latter experiment was not carried out unfortunately. It is difficult to understand, however, how flow distortion by the propellers can have such a remarkable effect on the vane dynamics.

## 2.5 Field Comparison Experiment

### 2.5.1 Experimental Setup

A field comparison experiment was carried out in June and July 1994 at the meteorological site of WAU. The site has a free fetch of more than 20 obstacle heights in most directions (Bottema, 1995). A sonic anemometer (Solent A1012R2, Gill Instruments, United Kingdom) was used as reference instrument. The k-vane model 35301 and sonic were placed on top of a 20-m mast (diameter 0.15 m, open lattice structure), each on either side of a 1.5-m-long boom. The gap in the potentiometer of the k-vane was oriented toward the sonic ( $150^\circ$ ). Nearly 300 28-min runs of raw data have been collected at a sampling rate of 10.4 Hz and spectra were computed. Both the finite response of the sonic as well as the separation between the sensors are insignificant when compared to the distance constant of the k-vane (Bottema, 1995).

No instrument is free of error and neither is the Solent sonic anemometer. Flow distortion by the sonic probe may cause an overestimation of 4%–6% in mean wind speed and 20% in momentum flux, according to Grelle and Lindroth (1994). Mortensen and Højstrup (1995), on the other hand, report a too-low response of the Solent for all wind speed components. However, most effects of flow distortion by the Solent show periodic behaviour (period  $120^\circ$ ). In the data selection used in the present analysis no such periodic

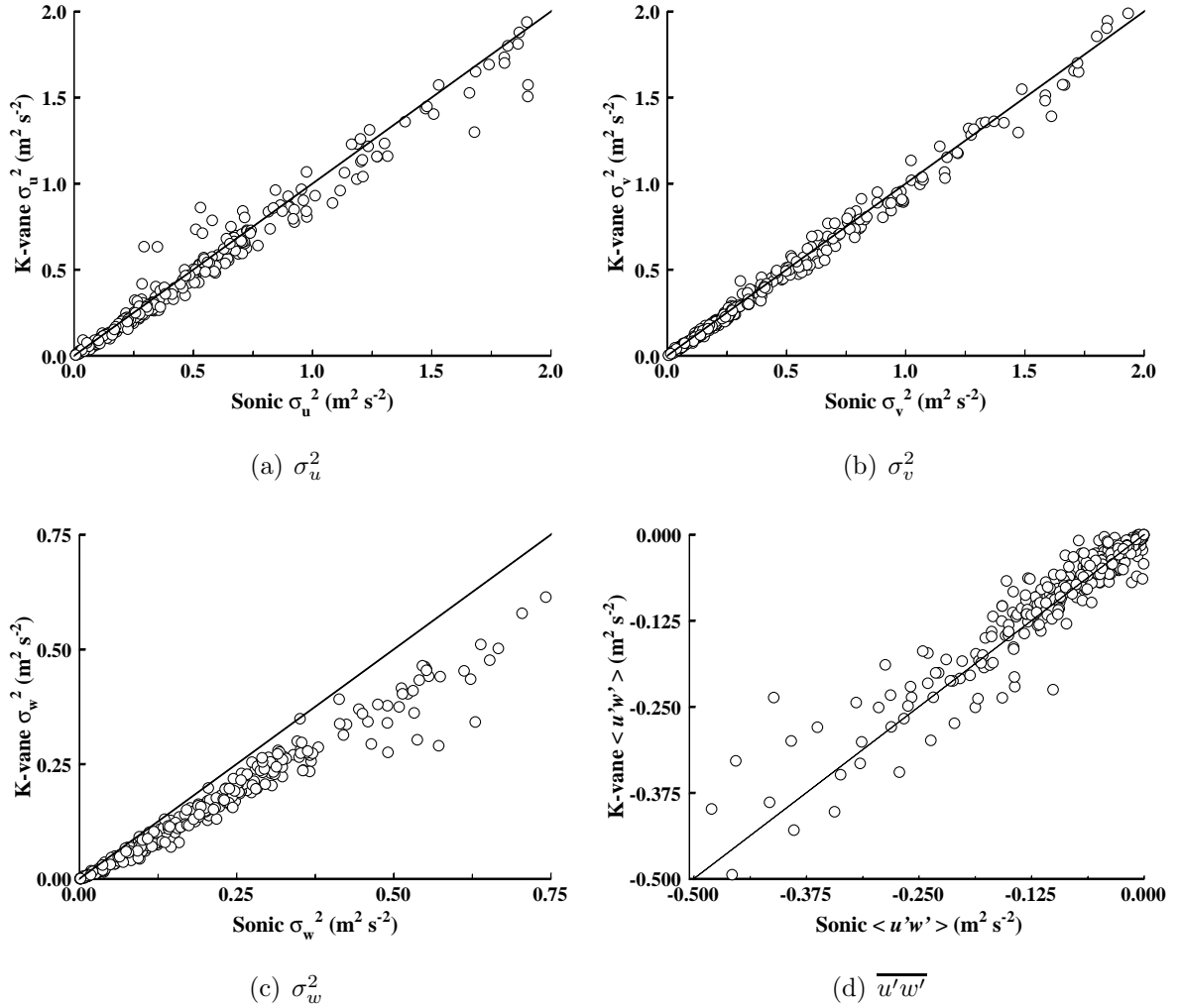


Figure 2.5: Comparison of the wind speed variances and momentum flux measured by the k-vane and sonic. Data were selected on stationarity and undisturbed fetch.

effects were found. So the effect of flow distortion by the Solent on the results is expected to be small, and no corrections were applied to the Solent data.

## 2.5.2 Statistical Results

In total 139 h of data were collected. Situations with weak wind were dominant, only 20% satisfied  $U > 4 \text{ m s}^{-1}$ . About 60% of the time unstable situations occurred, and almost 65% of the time the wind did not have a very disturbed fetch. From every 28-min file averages and (co-)variances have been calculated in three approximately 10-min blocks. No detrending was done. The 28-min averages of  $\overline{v'}$  and  $\overline{w'}$  were rotated to zero. A run was considered stationary when the average total wind speed of all three blocks was within 20% of the 28-min average. From the total data set regression coefficients were determined. Results are summarized in Table 2.3. None of the offset coefficients ( $c_0$ ) was significantly different from zero. Therefore only the uncertainty in  $c_0$  ( $\Delta c_0$ ) is given.

The absolute accuracy of wind direction by the vane was not determined since the absolute alignment of both sonic and k-vane is rather difficult. The overall average wind direction difference was put at zero. The standard deviation of all 10-min averages differ-

ences equalled  $0.8^\circ$ , so the accuracy of the vane is better than  $1^\circ$ . Large differences in wind direction were restricted to low wind speeds. Maximum differences in the selections  $U \geq 1, 2, \text{ and } 4 \text{ m s}^{-1}$  were  $5^\circ, 3^\circ, \text{ and } 2^\circ$ , respectively.

Table 2.3: Results from the field comparison experiment. Regression parameters  $c_0$  and  $c_1$  from equation  $k\text{-vane} = c_0 + c_1 \times \text{sonic}$ .  $c_0 = 0$  in all cases.

	$\Delta c_0$	$c_1$	$\Delta c_1$	$r^2$
$U$	0.06	1.013	.001	.999
$V$	0.02	0.993	.002	.996
$W$	0.02	0.95	.01	.92
$\sigma_u^2$	0.11	1.011 (0.966)	.003	.99
$\sigma_v^2$	0.06	0.998	.004	.99
$\sigma_w^2$	0.02	0.769	.004	.98
$\overline{u'w'}$	0.03	0.957 (0.91)	.009	.93

The k-vane-measured  $\sigma_w$  and  $\overline{u'w'}$  are less than the sonic-measured values. The highest loss is found for  $\sigma_w$  ( $-23\%$ ), as can be expected, since the contribution of high frequencies is most dominant in the  $w$ -spectrum. The k-vane-measured  $\sigma_u$  and  $\sigma_v$  are not systematically less than the sonic-measured values. This is due to the dominance of low-frequency variance in the  $u$ - and  $v$ -spectra, for which the k-vane’s limited response time is insignificant. Moreover, loss of high-frequency  $v$ -variance is partially compensated by amplification of variance at the natural wavelength of the vane. The relative high regression coefficients for  $\sigma_u$  and  $\overline{u'w'}$  appear to result from a few 10-min blocks with extraordinarily high values. The wind direction from most of these high-flux blocks is located in strongly disturbed fetch sectors. When data are selected on stationarity and strongly disturbed wind sectors are excluded, the regression coefficients of  $\sigma_u^2$  and  $\overline{u'w'}$  both decrease with 4% (see values in parenthesis in Table 2.3).

Scatter plots of the data selected on wind direction and stationarity are shown in the Figure 2.5. There seems to be no minimum wind speed to ensure reliable measurements. The selection on stationarity, however, tends to reject low wind speed situations. The minimum wind speed in this selection is  $0.3 \text{ m s}^{-1}$ .

### 2.5.3 Determination of K-vane Properties from Spectra

After selection on minimum wind speed ( $2 \text{ m s}^{-1}$ ), stationarity and wind direction (undisturbed fetch), average  $\overline{v'}$  and  $\overline{w'}$  were rotated to zero. No windowing or detrending was done. Spectra were calculated from segments containing  $2^{13}$  data points (approximately 13 min) at 20 frequency bands.

Transfer functions can be calculated by dividing the k-vane spectra by the sonic spectra. Transfer of  $\sigma_u$ ,  $\sigma_w$ , and  $\overline{u'w'}$  are dominated by the propeller dynamics and can be accurately approximated by the simple first-order equation [Eq. A.6]. The time “constant” is  $D_{45^\circ}/U$ , where  $D_{45^\circ}$  is the propeller’s distance constant at  $45^\circ$  angle of attack. The transfer of  $\sigma_v$  is dominated by the vane dynamics and can be approximated by a regular second-order equation [Eq. B.3].

Equations A.6 and B.3 have been fitted using least squares method to the observed transfer functions calculated from the selected data;  $D_{45^\circ}$  was found to be  $2.9 \text{ m}$  ( $\pm 0.5$

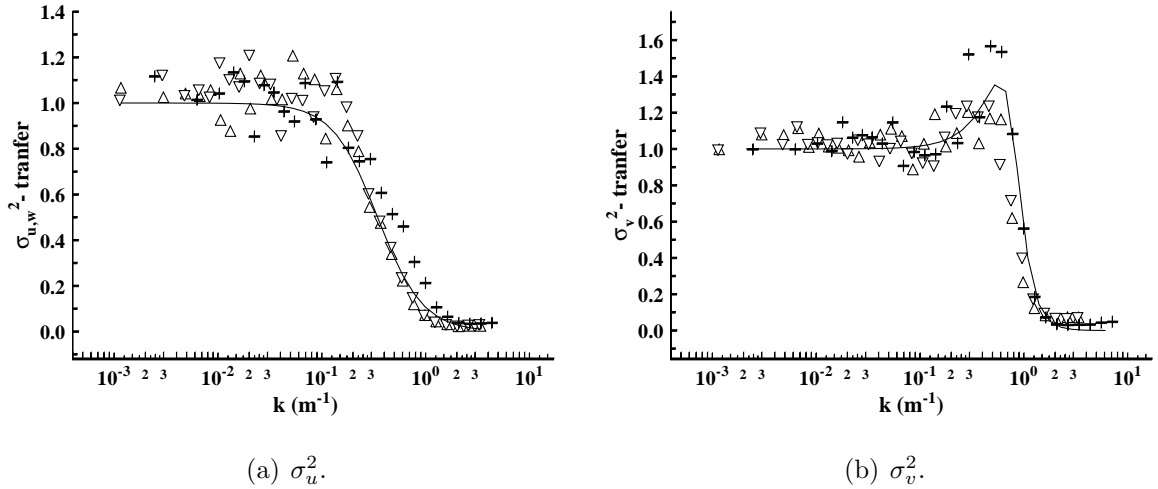


Figure 2.6: Measured and fitted transfer functions of the k-vane.

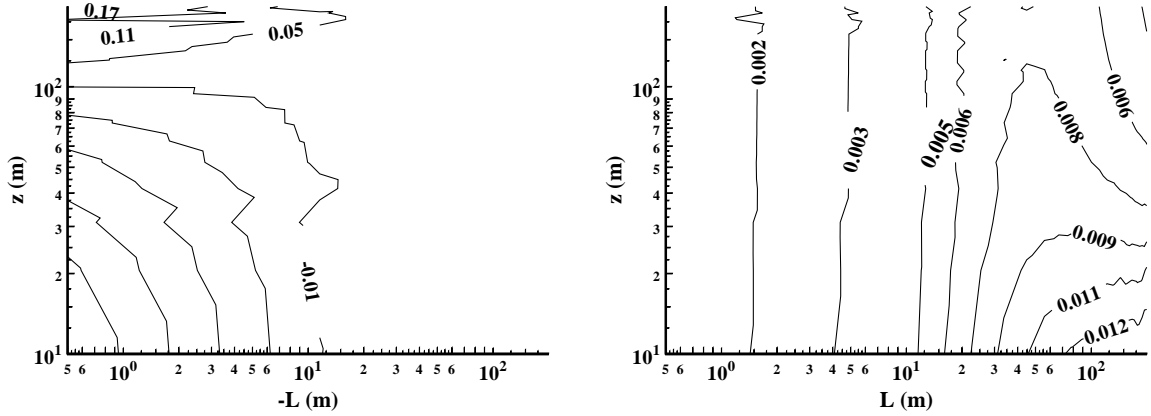
m),  $\lambda_n = 7.8$  m ( $\pm 0.9$  m), and  $\zeta = 0.49$  ( $\pm 0.05$ ). The fitted transfer function of  $\sigma_u^2$ ,  $\sigma_w^2$ , and  $\overline{u'w'}$  is plotted in Figure 2.6(a) together with the measured transfer functions of  $\sigma_u^2$  for three different runs. In Figure 2.6(b) measured and fitted transfer functions of  $\sigma_v^2$  are plotted.

## 2.6 Evaluation of Instrument Response Errors

The k-vane overspeeding and the ratio of measured to actual (co-)variances can be estimated from the k-vane parameters and spectra of atmospheric turbulence. Standard spectra for stable stratification were taken from Olesen et al. (1984); for unstable stratification spectra from Højstrup (1982) were used. Co-spectra of  $\overline{u'w'}$  were taken from Kaimal et al. (1972). Since the propeller and vane response is faster for higher wind speeds, all errors scale with  $U$ . Wind speed variances in the surface layer, however, scale with  $u_*$  and the boundary layer height  $z_i$ . To relate  $U$  to  $u_*$  for different heights, the log-linear wind law with stability corrections was used (Garratt, 1992, cf. chapter 3). Relations for  $\sigma_{u,v,w}$  for unstable stratification were taken from Højstrup (1982), and for stable stratification values from Kaimal and Finnigan (1994, cf. chapter 2) were adopted. In correspondence to the site at which the k-vanes are used, a roughness length ( $z_0$ ) of 0.1 m was taken and  $z_i$  was set at 1000 m.

### 2.6.1 K-vane Overspeeding

The k-vane parameters derived from the field experiment ( $D = 2.9$  m,  $\lambda_n = 7.8$  m,  $\zeta = 0.49$ ) were used to estimate the overspeeding. In Figs. 2.7(a) and 2.7(b) the total overspeeding is plotted for heights from 10 to 200 m as a function of stability ( $L$  is Obukhov length). Calculations for stable stratification are only meant for estimation of the order of magnitude of the overspeeding since surface layer scaling does certainly not apply over the whole height range in these conditions. Except for very unstable conditions, when the turbulence intensities become very large, k-vane overspeeding or underspeeding is less than a few percent. Note, however, that here again the parameterizations used for the turbulence intensities and spectra are out of their range of validity.



(a) Unstable stratification.

(b) Stable stratification.

Figure 2.7: K-vane overspeeding in stable and unstable stratification

From Eq. 2.24 note that  $\bar{\eta}$  usually will be negligible. The integral will obtain values from 0.9 in neutral conditions to 0.98 in very unstable conditions;  $(u_*/U)^2$  is usually of the order of magnitude  $10^{-2}$ , so the resulting  $w_m/U$  will be even one order of magnitude smaller.

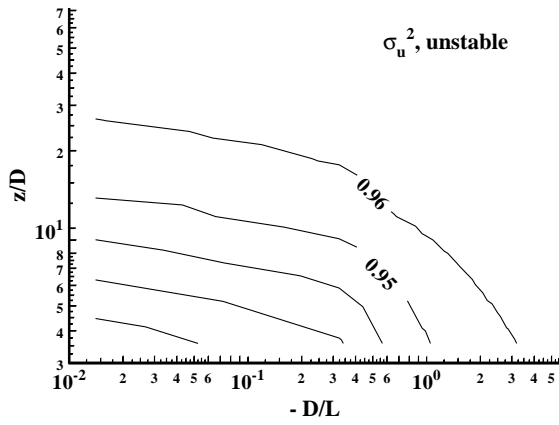
## 2.6.2 Correction of variances and momentum flux

The measured fractions of second-order moments have been estimated by integrating the product of the k-vane transfer functions and the relevant spectra. In Figure 2.8 the results are plotted for different values of  $z/D$  and  $D/L$ .  $D$ ,  $\lambda_n$ , and  $\zeta$  were taken from the field experiment, where  $z_i = 1000$  m and  $z_0 = 0.1$  m. For  $\overline{u'w'}$  (Figure 2.9) the spectrum of Moore (1986) is used. It represents an average of the unstable spectra described by Kaimal et al. (1972).

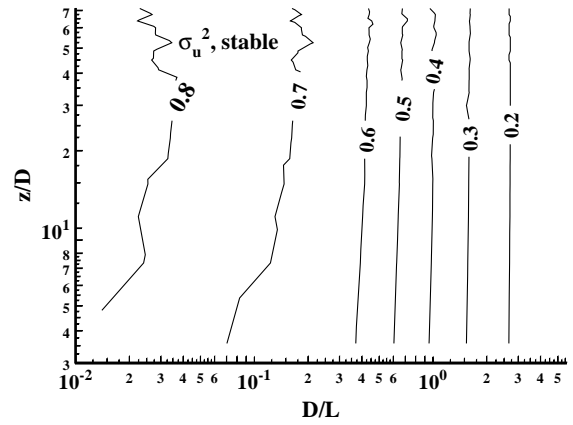
Although  $D$  from the field experiments is significantly smaller than that from the wind tunnel tests, the expected loss in (co-)variance is not significantly different when  $D_{45^\circ} = 3 \text{ m}/\sqrt{\cos 45^\circ} = 3.6$  m is used, which is the result from wind tunnel tests. At 10 m height the difference for  $\overline{u'w'}$  is only 3%, and it becomes even smaller at larger altitudes. Even for  $\sigma_w^2$ , which has the highest contribution of high-frequency turbulence, the difference remains smaller than 5% in nearly neutral conditions. For  $\sigma_u^2$  and  $\sigma_v^2$  differences are smaller than 2% in all circumstances. So the exact value of  $D$  does not seem to be critical at higher altitudes. In fact, the value  $z_i$ , which is hardly ever known, is of the same importance for  $\sigma_u^2$  and  $\sigma_v^2$ . When  $z_i$  values of 500 or 1500 m are used, differences up to 5% in the estimated losses are possible.

When  $z/L$  and  $z_i$  are available, the measured variances and momentum flux can be corrected using the estimated losses from the standard spectra. This has been done for the data selected on stationarity and undisturbed fetch. Again regression coefficients were calculated. The results are summarized on the left-hand side of Table 2.4. When compared to the results of the uncorrected data (Table 2.3), it can be seen that part of the lost variances and momentum flux can be restored without increasing scatter.

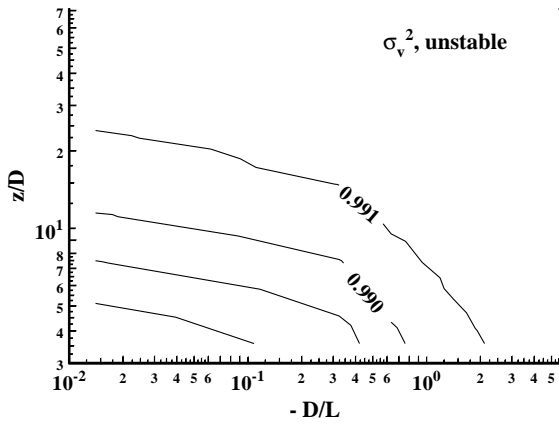
When standard spectra do not apply, spectra measured by the k-vane itself may be used to correct for loss of variance. Variance spectra can be divided by the appropriate transfer function and the resulting spectra can be integrated to obtain corrected variances.



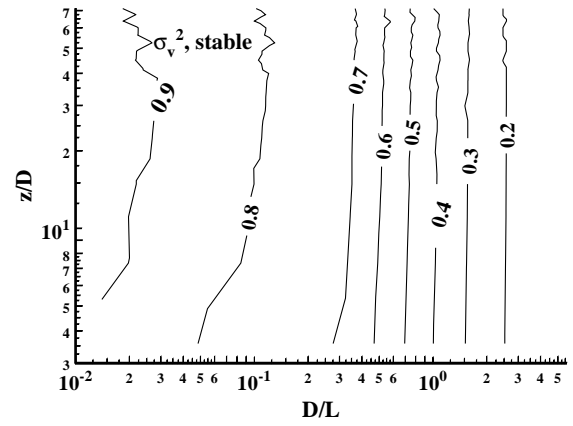
(a)



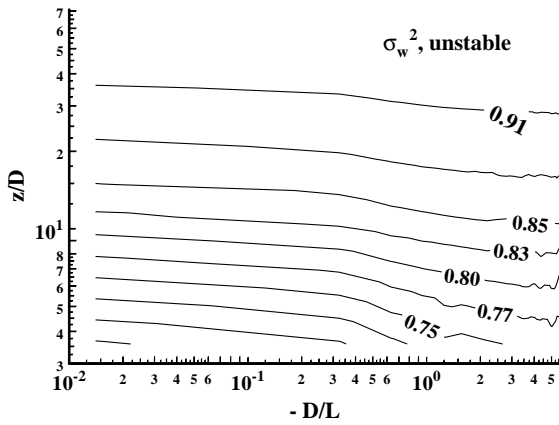
(b)



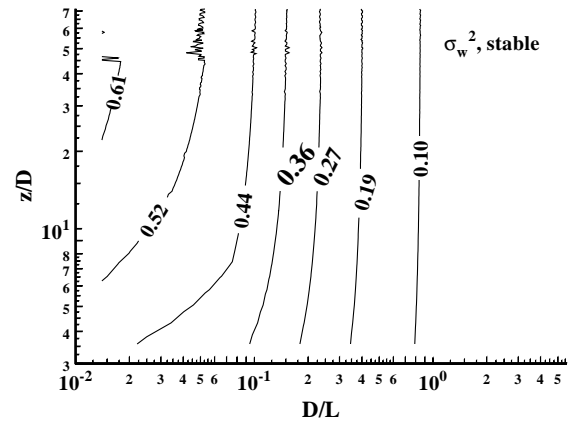
(c)



(d)



(e)



(f)

Figure 2.8: Measured fractions of  $\sigma_u^2$ ,  $\sigma_v^2$ , and  $\sigma_w^2$  in stable and unstable conditions estimated from standard spectra.

Integration has to be truncated at the high-frequency end where the signal-to-noise ratio or the transfer function is very low. In this analysis, integration was truncated when the transfer function was below 0.04. The results are summarized on the right-hand side of Table 2.4.

Except for  $\sigma_w$  the two methods yield comparable results. When standard spectra are used, the corrections for  $\sigma_w$  become very large in stable conditions because of the dominance of high-frequency variance. This way noise in the measurements is also amplified. On average, however, this leads to a  $c_1$  close to 1 but a somewhat lower correlation coefficient. Amplification of noise is explicitly avoided when calculating the correction coefficients from the measured spectra. This may be the reason why the resulting  $\sigma_w$  is lower.

Table 2.4: Regression parameters for the corrected data. Spectra were taken from literature (left-hand side) or spectra measured by the k-vane itself were used (right-hand side).

	Standard spectra				Measured spectra			
	$\Delta c_0$	$c_1$	$\Delta c_1$	$r^2$	$\Delta c_0$	$c_1$	$\Delta c_1$	$r^2$
$\sigma_u^2$	0.09	1.038	.009	.98	0.06	1.017	.005	.992
$\sigma_v^2$	0.06	1.010	.007	.99	0.05	1.002	.005	.992
$\sigma_w^2$	0.05	1.03	.01	.95	0.02	0.930	.007	.98
$\overline{u'w'}$	0.03	0.96	.02	.90	0.03	0.94	.02	.87

## 2.7 Discussion

### 2.7.1 Minimum wind speed

The threshold wind speed of a propeller with well-maintained bearings is of the order of 0.1–0.2 m s<sup>-1</sup>. From the scatter plots (Figure 2.5), including many runs with  $U$  between 0.3 and 1 m s<sup>-1</sup>, it can be concluded that the minimum wind speed the k-vane needs for reliable measurements is of the same order of magnitude. When bearings wear during long-term field experiments, however, the threshold wind speed will increase and the sensitivity of the propellers will decrease. To exclude any influence of friction at low rotation speed, situations with  $U$  below 1–2 m s<sup>-1</sup> should not be considered. Note that the propeller response deviates in the wind tunnel from its regular response when  $U$  is below 4 m s<sup>-1</sup>.

### 2.7.2 Bottema’s results

Bottema (1995) tested the k-vane’s propellers (model 08254) in the wind tunnel of WAU before the field comparison experiment took place. He found the calibration of propellers was in agreement with their pitch, and no significant deviations of  $k$  from unity [see Eq. A.2] could be measured. The threshold wind speed  $U_{\text{thr}}$  and correction  $\Delta u_f$  both equalled 0.2 m s<sup>-1</sup>. The best fit of measured cosine response was expressed in goniometric functions, inspired by the expansion formulation in Busch et al. (1980), and was given in Eq. A.4.

Bottema determined the distance constant at 2.5 m and claims that the dependence on angle of attack agreed with

$$D(\psi) = D(0^\circ) / \sqrt{\cos \psi}.$$

From this one would expect  $D = 2.9$  m for 45° angle of attack. Bottema, however, reports a value of 3.5 m for  $D_{45^\circ}$ . For large wind speed drops, he reports a faster propeller response.

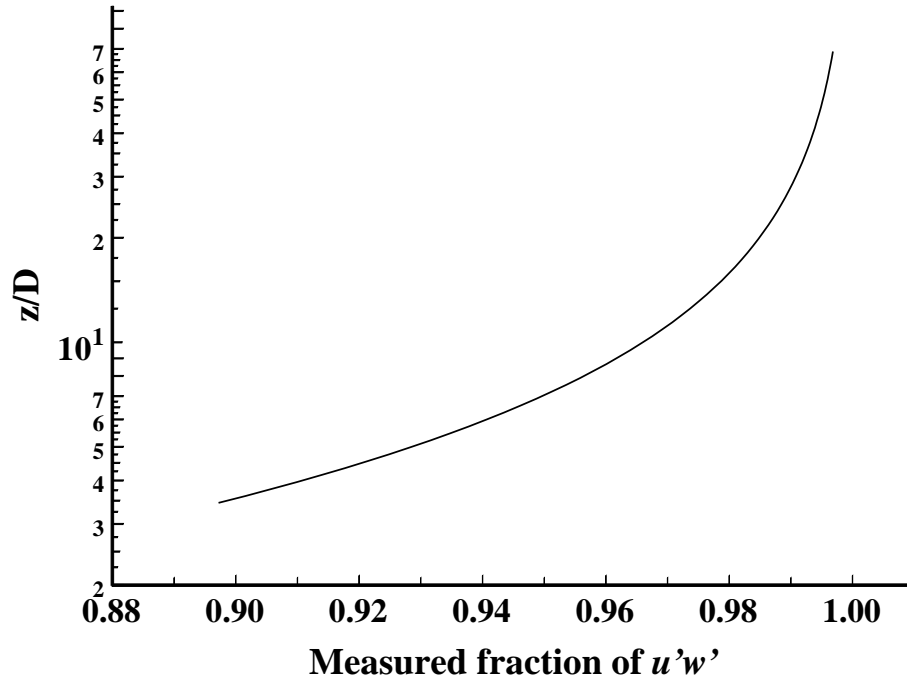


Figure 2.9: Measured fraction of  $\overline{u'w'}$  calculated from literature spectra for unstable conditions.

These step-down tests were performed by poor-man methods such as quickly opening the wind tunnel door or by speeding up the propeller by motor and V-belt and then suddenly pushing the belt away.

Because of the size of the k-vane (length of arm and blade 0.7 m, working section wind tunnel 0.40 m  $\times$  0.40 m), vane tests could hardly be done in the WAU wind tunnel. For want of something better, Bottema still evaluated vane properties from experiments in this wind tunnel. His reported values of the natural wavelength  $\lambda_n$  and the damping ratio  $\zeta$  vary considerably with wind speed. Bottema argues that the most reliable estimates of  $\lambda_n$  and  $\zeta$  were made at low wind speeds because of undesirable oscillation phenomena at high wind speeds. At  $U = 2 \text{ m s}^{-1}$  he found  $\lambda_n = 4 \text{ m}$  and  $\zeta = 0.4$ .

### 2.7.3 Propeller Response at Low Wind Speeds

The smaller  $D$  for both step-up and step-down changes (Figure 2.2) can be the result of the size of the step change. Doing tests at low wind speeds usually means applying small wind speed changes as well, especially for the step-down tests. Hicks (1972) found that “the time required for a propeller to respond to sudden increases in wind speed increases with the magnitude of the fluctuation”. In other words, at low wind speeds, applying small wind speed changes, the propeller responds quicker.

This also explains the smaller  $D$  and larger  $D_{45^\circ}$  found by Bottema. He used wind tunnel speeds of 2, 4 and 6  $\text{m s}^{-1}$  when doing step response tests and found a  $D$  of 2.4, 2.7 and 2.8 respectively (Bottema 1997, personal communication). This is in close agreement with Figure 2.2. The reported average value for  $D$  is biased because the wind speeds used were too low. Since the propeller response is less when it is inclined to the flow, Bottema

probably used a larger wind tunnel speed when assessing  $D_{45^\circ}$ . The resulting response length will be larger because of this larger wind tunnel speed.

The faster propeller response for wind speed decreases compared to wind speed increases will reduce the overspeeding of the propeller. If the difference between step-up and step-down response times as well as the magnitude of the wind speed fluctuations was to be large, the step-down response time could even be smaller than for a step-up time. In that case the propeller could underspeed.

### 2.7.4 Field Versus Laboratory Response

For both propeller and vane it seems that the field response is faster than the tunnel response, resulting in a smaller  $D$  and  $\lambda_n$ . For the propellers discussed in this report  $D = 3.0$  m (wind tunnel), and  $D_{45^\circ} = 2.9$  m (field experiment), which do not correspond at all to the observed increase of  $D$  with angle of attack. The parameters found for the vane are  $\lambda_n = 7.8$  m,  $\zeta = 0.49$  (field comparison) and  $\lambda_n = 13$  m,  $\zeta = 0.54$  (wind tunnel). A reason for the difference may be that the wind tunnel used is too small for the present propellers. However, other researchers also found a faster response in the field than in the laboratory (Fichtl and Kumar, 1974; Pond et al., 1979). Because in a turbulent wind field there are no step changes, the propeller will usually be closer to its equilibrium response. Hicks's (1972) results suggest that the faster field response may be caused by the smaller wind speed changes that are applied. On the contrary, Horst (1973) explained a *larger*  $D$  found from field experiments as the result of the increase of  $D$  with angle of attack. Since the field comparison results show less scatter and the *field* performance is thought to be of major importance, the author recommends using these results only when assessing instrument response parameters.

Katsaros et al. (1993) obtained propeller and vane parameters from *laboratory* tests. The natural wavelength and damping ratio they reported compare well to those found from our *field* comparison experiment. The vane they used, however, had slightly different dimensions. The distance constant they reported (2.2 m) is small. From their report it is not clear whether this is the distance constant at  $0^\circ$  angle of attack. If so,  $D_{45^\circ}$  is approximately 2.6 m, which is close to the value of 2.9 m found from the *field* comparison experiment.

### 2.7.5 Simple Methods for the Estimation of Vane Parameters

For simple vanes Wieringa (1967) derived formulas to estimate their dynamic parameters from the dimensions and weight of the vane (see appendix B). For the k-vane  $S = 0.094$  m<sup>2</sup> (area of the vane blade),  $r_v = 0.48$  m (distance from the vane pivot to one-quarter of the blade chord), and  $J_{old} = 0.086$  kg m<sup>2</sup> (moment of inertia of the vane). The latter has been assessed by attaching a little weight on the vane and then measuring the period of oscillation. This experiment has been repeated for several weights at different distances from the pivot of the vane. To reduce damping by the vane, the blade was twisted  $90^\circ$ .

When an infinite aspect ratio is assumed, the torque parameter  $a_v$  equals  $2\pi$ , where  $N/U^2 = 0.18$  kg,  $\lambda_n = 4.4$  m, and  $\zeta = 0.34$ . These values compare rather well with the values Bottema (1995) found ( $N/U^2 = 0.16$  kg,  $\lambda_n = 4$  m, and  $\zeta = 0.4$  at  $U = 2$  m s<sup>-1</sup>). Since the blade of the k-vane approximates a square, the aspect ratio is not infinite. In fact,  $a_v = 2.0$  (span of the vane blade  $b = 0.36$  m). In that case  $\lambda_n$  and  $\zeta$  should equal 6.0

m and 0.25 respectively. When using the results of section 2.4.2 on the torque on the vane as function of angle of attack,  $\lambda_n = 8$  m and  $\zeta = 0.2$ .

The presence of the propellers and their mounting can certainly not be neglected in case of the k-vanes. The presence of surface before the pivot of the vane will increase  $\lambda_n$  as well as  $\zeta$ . The area of the projection of the surface before the pivot on a vertical plane  $S_w$  is estimated at  $0.02 \text{ m}^2$  and the distance of the aerodynamic centre to the vertical axis  $r_w$  is 0.2 m. This results in an increase of almost 5% in  $\lambda_n$  and of 9% in  $\zeta$  (Wieringa and Van Lindert, 1971).

These formulas apply to simple vanes, however. The shape of the propellers and their mounting does not resemble that of a vane. This may explain the large difference, especially in  $\zeta$ , between the estimated vane parameters and the measured parameters.

## 2.8 Conclusions

From the field experiment it can be concluded that k-vane's measurements of average wind speed and direction are very accurate. Overspeeding or artificial vertical wind speed will generally be very small. Overspeeding could be significant in conditions of very high instability. These occasions usually are accompanied by very low wind speeds. Then the correction  $\Delta u_f$ , which is usually neglected, and the different propeller response at these wind speeds may mask any overspeeding.

Both perturbation theory and a field comparison experiment show that the k-vane behaves as a first-order sensor. The only relevant instrument parameter for measured variances and fluxes is  $D_{45^\circ}$ , the response length at  $45^\circ$  angle of attack (2.9 m for the 35301 model). This parameter can best be determined from a field comparison experiment, not from wind tunnel tests. Wind tunnel tests show much scatter, and the resulting parameters do not correspond very well to those from the field comparison experiment. When used above 20 m height, however, the exact value of  $D_{45^\circ}$  is of insignificant importance.

Transfer functions of the (co-)variances can be described by the regular first-order [Eq. A.6,  $\sigma_u^2$ ,  $\sigma_w^2$ , and  $\overline{u'w'}$ ] or second order [Eq. B.3,  $\sigma_v^2$ ] equations. These transfer functions together with standard spectra can be used to estimate the loss of (co-)variance. To do so a stability parameter and boundary layer height are necessary. After this correction the velocity variances correspond well to those measured by a sonic anemometer. In very stable conditions the corrections may become large, increasing scatter in the corrected results.

Instead of standard spectra, spectra measured by the k-vane itself can be used to calculate corrections for the measured (co-)variances. In that case no information on atmospheric conditions is necessary. Using this method high-frequency variance may not be fully restored, resulting in lower estimates of  $\sigma_w$ . On average both methods yield fluxes and variances that are correct within 10%.

## Acknowledgments

The author would like to thank Prof. Jon Wieringa for setting up this project and for good advice at various stages while writing this paper. The author would also like to thank Dr. Marcel Bottema who prepared and started the field comparison experiment. Arjan van Dijk from the Delft University of Technology helped me doing the wind tunnel tests at his department. In carrying out the experiments many of the technical staff of the meteorology department of WAU were of great help. I would like to especially mention

Bert Heusinkveld and Frits Antonysen. Also many thanks to Fred Bosveld from the KNMI, members of the Meteorology Department of WAU, and the reviewers who carefully read the manuscript and gave lots of valuable comments.

The investigations were (in part) supported by the Netherlands Geosciences Foundation (GOA) with financial aid from the Netherlands Organisation for Scientific Research (NWO), project no. 750.194.15.



# Chapter 3

## Wind profiles, momentum fluxes and roughness lengths at Cabauw revisited

In review in *Boundary-Layer Meteorology*, 2006. Co-author: A. A. M. Holtslag

### Abstract

This paper describes the results of a measuring campaign focusing on wind speed and momentum fluxes in the atmospheric boundary layer up to 200 m. The measurements were conducted in 1996 at the Cabauw site in the Netherlands. Momentum fluxes are measured using the K-Gill Propeller Vane. Estimates of the roughness length are derived using various techniques from the wind speed and flux measurements, and the observed differences are explained by considering the source area of the meteorological parameters. A clear rough-to-smooth transition is found in the wind speed profiles at Cabauw. The internal boundary layer reaches the lowest k-vane (20 m) only in the south-west direction where the obstacle-free fetch is about 2 km. The internal boundary layer is also reflected in the roughness lengths derived from the wind speed profiles. The lower part of the profile ( $< 40$  m) is not in equilibrium and no reliable roughness analysis can be given. The upper part of the profile can be linked to a large-scale roughness length. Roughness lengths derived from the horizontal wind speed variance and gustiness have large footprints and therefore represent a large-scale average roughness. The drag coefficient is more locally determined but still represents a large-scale roughness length when it is measured above the local internal boundary layer. The roughness length at inhomogeneous sites can therefore be determined best from drag coefficient measurement just above the local internal boundary layers directly, or indirectly from horizontal wind speed variance or gustiness. In addition the momentum and heat flux along the tower are analyzed and these show significant variation with height related to stability and possibly surface heterogeneity. It appears that the dimensionless wind speed gradients scale well with local fluxes for the variety of conditions considered, including the unstable cases.

### 3.1 Introduction

This paper describes an experiment set up to further investigate profiles of wind speed, fluxes, flux-profile relationships, and roughness lengths at relatively high altitudes in the atmospheric boundary layer (ABL) at Cabauw (The Netherlands). The 213-m high tower

offers excellent opportunities for boundary-layer research and many studies have been done on the roughness and flux-profile relationships (Van Ulden and Wieringa, 1996; Beljaars and Bosveld, 1997). Nieuwstadt (1978) fitted profiles of wind speed and temperature measured along the tower to the flux-profile relationships. In the west direction, the most open sector at Cabauw, he found large discrepancies between the fluxes from the profiles and direct flux measurements. Beljaars (1982) showed that about half of the momentum flux can be attributed to form drag on the wind breaks in the Cabauw environment. Close to the tower the surface is free of obstacles. Consequently, momentum fluxes close to the surface are lower than those aloft and the local roughness length is much smaller than the large-scale roughness length.

Using a small data set Beljaars et al. (1983) showed that the momentum flux increases 40% between 3.5 and 22.5 m for wind directions with wind breaks in the upstream terrain. The dimensionless wind speed gradient in the lowest 10 m is closer to literature values when it was increased by 40% for those directions. Nieuwstadt (1984) used Cabauw data and showed that in stable boundary-layers the dimensionless gradient scales with the local fluxes of momentum and heat instead of the surface fluxes. Holtslag (1984) estimated the momentum and heat flux at the surface from data that are available at standard synoptic stations. He estimated wind speed profiles up to 200 m and compared them to observations at the tower. Beljaars (1987b) estimated the large-scale roughness lengths from observations of the standard deviation of the horizontal wind speed in the surface layer and found values between 0.04–0.15 m depending on wind direction.

In the present study we elaborate on the results of Beljaars et al. (1983), however, our data set is much larger. We investigate whether the flux-profile relationships are valid in the disturbed boundary-layer and explore the use of local scaling in stable and unstable conditions. Note that only few papers deal with the validation of local scaling of wind and temperature gradients in unstable conditions. Sorbjan (1986) tested local scaling for the dimensionless wind speed ( $\phi_m$ ) and temperature gradient ( $\phi_h$ ) using a small data set from Minnesota. Yumao et al. (1997) tested local scaling for  $\phi_m$  and  $\phi_h$  for an urban and a rural site near Nanjing. Recently, Steeneveld et al. (2005) tested local scaling at Cabauw for temperature and humidity profiles.

In this paper we test local scaling for  $\phi_m$  at Cabauw. Although the landscape at Cabauw is fairly open, there are frequent wind breaks and scattered villages causing a strong disturbance of the surface layer (Beljaars, 1982). The density and distance of the disturbances is different for different wind directions. In addition, we compute the surface roughness using several methods. We investigate how the roughness lengths relate to the fluxes, wind speed profiles and their footprint areas. We re-evaluate the results of Nieuwstadt (1978) and explain the discrepancies he observed between momentum fluxes from profiles and direct flux measurements. Our flux measurements include momentum and sensible heat fluxes. In this paper we focus on the wind speed profile and momentum flux. We present the results of the summer period (May–October). During this period wind conditions were close to their climatological normals.

## 3.2 Experiment

The Royal Netherlands Meteorological Institute (KNMI) has conducted ABL observations at the Cabauw site since the early seventies. The tower is a solid cylinder with 2 m diameter. It is 213 m high and has booms in three direction (10°, 130°, 250°) at intervals of 20 m.



Figure 3.1: Roughness lengths in gray scale for the Cabauw environment  $[(10 \text{ km})^2]$ . The circle in the center of the figure indicates the tower position. Pixel size  $(25 \text{ m})^2$ .

The booms extend 9.4 m beyond the surface of the cylinder. At the end of the north and south-west pointing booms two lateral extensions (1.5 m) carry four plugs. The routine observations include profiles of meteorological parameters (e.g. wind speed and direction, temperature, moisture) and a number of surface parameters (e.g. radiation, precipitation). Table 3.1 gives details on the installed instruments (Monna and Van der Vliet, 1987; Van der Vliet, 1998).

From the routine surface layer observations the friction velocity and sensible heat flux are computed using the flux-profile relationships for homogeneous terrain (Dyer, 1974). These observations are referred to as the surface layer observations of  $u_{*SL}$  [ $\text{m s}^{-1}$ ] and  $H_{SL}$  [ $\text{W m}^{-2}$ ] in this paper.  $H_{SL}$  and  $u_{*SL}$  are computed from the wind speed at 10 m, a tabulated effective roughness length relevant for the particular wind direction, and the difference in temperature between 1.5 and 10 m (Wessels, 1984).

The roughness length ( $z_{0std}$ , [m]) has been derived from the ratio of the standard deviation of the longitudinal wind speed variations ( $\sigma_u$ ) to the wind speed in 10-min averaging periods measured during neutral conditions at 10 m height (Beljaars, 1987a; Beljaars, 1988). From  $u_{*SL}$  and  $H_{SL}$  the surface layer stability parameter (Obukhov length) is calculated from  $L = -u_*^3 \theta c_p \rho / \kappa g H$ . Here  $\theta$  is the temperature [K],  $\rho c_p$  is the product of the specific heat and density of air [ $\text{J K}^{-1} \text{m}^{-3}$ ], and  $g$  is the acceleration of gravity [ $\text{m s}^{-2}$ ].

In 1996 the routine measurements were completed with direct flux measurement at the tower. K-Gill Propeller Vanes were used to measure momentum and sensible heat fluxes. The k-vane is an instrument comprising two propellers, one oriented  $45^\circ$  upward, the other  $45^\circ$  downward, and a vane to aim the propellers into the main wind direction. They have been equipped with a thermocouple to measure the heat flux. The k-vane is a first order response instrument with a response length of 2.9 m. Details on the k-vane can be found

in Verkaik (1998). The averaging period is 30 minutes for both the k-vane measurements and the routine Cabauw measurements. Data on the atmospheric boundary layer (ABL) height is not available for the major part of our data set.

Table 3.1: Instrumentation at the Cabauw tower during the summer of 1996.

Element	Height (m)	Direction	Instrument
Temperature	0.6, 1.5, 10, 20, 40, 80, 140, 200	south-east	Thermocouple (melting ice reference at 0.6 and 200 m)
Wind	10, 20, 40, 80, 140, 200	south-west, north	Propeller vane (Gill 8002DX)
Momentum and heat fluxes	20, 100, 180	south-west, north	K-Gill propeller vane (Young 35301)

Table 3.2: Wind direction sectors for Data Analysis.

north	315°–45°	regularly spaced wind breaks, 1–2 km spacing, on pasture making a shelterbelt landscape
east	45°–105°	a chain of small villages making up a uniform rough landscape
south	105°–165°	orchards, dikes and the river bed making up a rather complex, scattered rough terrain
west	180°–240°	nearly smooth, open landscape

Table 3.3: Stability Classes for Data Analysis.

1. Unstable		$L^{-1} < -(200 \text{ m})^{-1}$
2. Slightly Unstable	$-(200 \text{ m})^{-1} \leq$	$L^{-1} < 0$
3. Slightly Stable	$0 <$	$L^{-1} \leq (200 \text{ m})^{-1}$
4. Stable	$(200 \text{ m})^{-1} <$	$L^{-1}$

Table 3.4: Data selection rules, number of 30-min runs, and percentages of data coverage.  $U$ : wind speed,  $\theta$ : temperature, and  $D$ : wind direction.

Total	8832	100%
$U_{\text{SL},20} \geq 3 \text{ m s}^{-1}$	6163	70%
$\theta_{\text{SL},20}$ and $D_{\text{SL},20}$ present	5503	62%
no precipitation	5092	58%
$u_{*\text{SL}}$ present	4835	55%
$D$ within selected directions	3670	42%
$U_{\text{kv}} \geq 3 \text{ m s}^{-1}$ at each height	$\approx 2500$	$\approx 30\%$

Wind speed measurements at the tower suffer from flow distortion. For that reason two anemometers are placed at each level, one on the north (on the most right plug of the right lateral extension) boom and one on the south-west boom (on the most left plug on the left lateral extension). The anemometer which is best exposed is used in the analysis. At 20 m and below the building at the base of the tower causes flow distortion as well (Wessels, 1983). The octagonal shaped building is 3.8 m high and has a diameter of 17.3 m. For that reason the wind speed measurements at 10 and 20 m are not measured at the main tower but at auxiliary masts 29 m in south-east and 73 m in the north-west direction of the main tower. However, the flux measurements at 20 m are done at the main tower. Comparison of the momentum and heat flux measurements at each level as function of wind direction shows that the flow distortion by the tower and the building does not affect the flux measurement significantly, not even at the 20-m level.

When planning the measurement campaign the k-vanes were preferred to sonic 3-D anemometers as they were considered better all-weather flux probes and, at that time, a cheaper alternative. The measurements continued throughout the summer of 1996. Due to frequent malfunctioning of the k-vane's electronics, however, the data set has many gaps.

### 3.3 Terrain description

The Cabauw tower is situated in the central river delta in the south-western part of the Netherlands ( $52^{\circ}58'18''$  N,  $4^{\circ}55'37''$  E). It is surrounded by meadows ( $> 80\%$  grass). The North Sea is about 50 km away in the north-west direction. Close to the tower the surface consists mainly of short grass with several small villages, scattered farms, rows of trees and bushes. Maps of the Cabauw environment have been published in Holtslag (1984), Monna and Van der Vliet (1987), and Van Ulden and Wieringa (1996).

A map of the roughness in the Cabauw environment is plotted in Fig. 3.1. The roughness map is derived from the land-use map LGN3+ of the Dutch environmental research institute Alterra (De Wit et al., 1999). LGN3+ is a raster file covering the whole of the Netherlands with a resolution of  $(25 \text{ m})^2$ . LGN3+ is derived from Landsat-TM satellite images from 1995 and 1997 and topographical information. Over forty land use types are distinguished of which 15 are present in the Cabauw environment. Despite the high resolution of the LGN3+-images, narrow roughness elements like tree lines may not be distinguished. For example, most roads in the Cabauw environment are lined with trees which are rarely detected. Even so, complex terrain features, like the riverbanks, are not recognized. To each land-use type a roughness length adopted from literature is assigned (Wieringa, 1993). Note that these roughness lengths usually refer to homogeneous areas, while they are applied to inhomogeneous terrain here.

Fig. 3.1 shows that southwest of the tower is the only sector that is open and nearly free of obstacles for several kilometers. To the north there is a road with houses and trees comprising a windbreak-like obstacle at a minimum distance to the tower of about 0.5 km. Farther upstream pasture continues until again there is a road with houses and trees at about 3 km. To the east is the village Lopik at a distance of 1 km. In this direction the local road continues and so do the built-up areas and trees. To the southeast lies a complex terrain with roads, orchards, and the river bed. From inspection of the land-use map four wind direction sectors are distinguished for the Cabauw site (see Table 3.2). The data set will split up in these wind direction sectors to assess the influence of differences in the upstream terrain on the profiles and fluxes.

### 3.4 Data set

As the k-vanes need some wind to operate properly, only those cases are selected where the wind speed measured at 20 m by the tower and the k-vanes at all levels is equal to or larger than  $3 \text{ m s}^{-1}$ . Runs with significant precipitation are also excluded, *i.e.* the amount of precipitation is less than 0.1 mm, and the duration is less than 1 min per 30-min interval. Next the routine measurements of the wind direction and temperature at 20 m and the friction velocity must be available.

Table 3.4 shows how the number of 30-min runs available for analysis is reduced by the selection rules. While the highest possible number of 30-min runs in the summer period is 8832, about 2500 momentum flux runs (30% data coverage) and 2000 heat flux runs (25%) are available for analysis at each level. For the determination of the roughness lengths the following addition criteria are used to exclude cases with shallow boundary layers (Korrell et al., 1982): wind direction turning with height is less than  $20^\circ$ , the friction velocity is larger than  $0.15 \text{ m s}^{-1}$ , and the wind speed gradient must be positive.

The surface layer Obukhov length ( $L$ ) has been used to split up the data set in four stability classes (see Table 3.3). The distribution of the runs over the stability and wind direction classes is given in Table 3.5 and 3.6. Table 3.5 and 3.6 show that stable conditions prevailed during the measuring campaign. The number of runs in the east sector is substantially less than for the other sectors.

To determine at what time of day the selected stability subsets are taken, for each subset  $\cos(2\pi \text{ time}/2400)$  and  $\sin(2\pi \text{ time}/2400)$  are averaged. The phase angle of the resulting vector indicates the preferential time and its length is a measure for this preference. In case all events would occur at the same time the vector would have unity length, in case the events would be randomly distributed over time the vector would have a length close to zero. For all k-vane heights and wind direction sectors together the results are (1146, 0.77) for unstable, (1236, 0.58) for slightly unstable, (2140, 0.14) for slightly stable and (2307, 0.57) for stable conditions. It is clear that the (slightly) unstable subset comprises many samples taken round or before noon. It can be expected that the ABL is shallow and rapidly growing. In those cases the selection of wind speeds larger than  $3 \text{ m s}^{-1}$  favors conditions with strong entrainment (Driedonks and Tennekes, 1984; Pino et al., 2003). The stable subset is dominated by samples taken round midnight and the slightly stable subset has a small surplus of samples taken in the early evening.

In addition to the selection criteria listed above, we have also used the criteria given by Korrell et al. (1982) to identify the measurements taken in the surface layer. This confirmed that especially in stable conditions at 100 and 180 m a large number of the observations is actually above the surface layer.

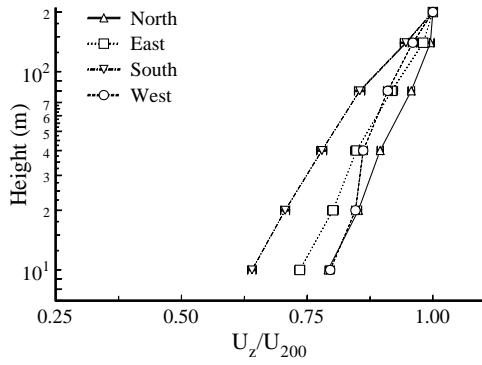
Malfunction of the k-vanes has been a serious problem. The main cause for this has been frequent breakdown of the electronics in the photochopper of the propeller. Although the exact reason never became clear, it is probably due to atmospheric electricity. At our demand the Young company replaced the plastic propeller shafts by stronger metal shafts. Because of this atmospheric electricity could be conducted into the photochopper electronics. Later during the experiment spark bridges were used in the photochopper unit and after that this failure occurred less often. Other causes of drop-out were short-circuit in the thermocouple amplifiers, broken thermocouples by rain or hail and computer failure.

Table 3.5: Numbers of 30-min runs for the analysis of the momentum flux.

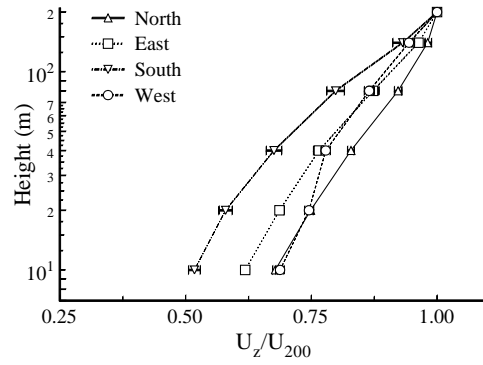
Stability class	Height (m)	Wind direction sector				All sectors
		1	2	3	4	
Unstable	20	260	39	121	210	630
	100	315	33	124	214	686
	180	247	60	110	98	515
	All heights	822	132	355	522	1831
Slightly unstable	20	227	82	45	177	531
	100	243	12	44	161	460
	180	198	85	42	104	429
	All heights	668	179	131	442	1420
Slightly stable	20	113	93	26	213	445
	100	141	5	27	177	350
	180	109	98	27	130	364
	All heights	363	196	80	520	1159
Stable	20	231	167	318	357	1073
	100	295	118	299	371	1083
	180	250	211	308	262	1031
	All heights	776	496	925	990	3187
Totals		2629	1003	1491	2474	7597

Table 3.6: Numbers of 30-min runs for the analysis of the sensible heat flux.

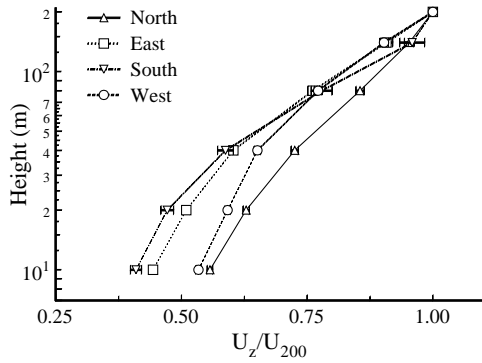
Stability class	Height (m)	Wind direction sector				All sectors
		1	2	3	4	
Unstable	20	225	33	78	113	479
	100	315	28	106	200	649
	180	217	36	89	91	433
	All heights	787	97	273	404	1561
Slightly unstable	20	220	82	38	101	441
	100	243	10	44	155	452
	180	153	76	36	102	367
	All heights	616	168	118	358	1260
Slightly stable	20	111	93	21	149	374
	100	141	4	26	173	344
	180	88	96	22	130	336
	All heights	340	193	69	452	1054
Stable	20	219	164	210	228	821
	100	295	100	286	351	1032
	180	190	147	262	244	843
	All heights	704	411	758	823	2696
Totals		2447	869	1218	2037	6571



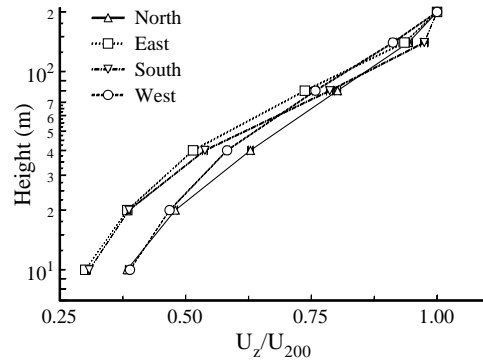
(a) Unstable,  $1/L < -0.005 \text{ m}^{-1}$



(b) Slightly unstable,  $-0.005 \text{ m}^{-1} < 1/L < 0$



(c) Slightly stable,  $0 < 1/L < 0.005 \text{ m}^{-1}$



(d) Stable,  $1/L > 0.005 \text{ m}^{-1}$

Figure 3.2: Scaled wind speed profiles.  $U_z$  has been scaled by  $U_{200}$  (routine Cabauw measurement).

### 3.5 Wind profiles and Fluxes

Profiles of wind speed ( $U$ ), normalized with the wind speed at 200 m are plotted in Figure 3.2 for all wind direction sectors and stability classes. Per wind direction sector and stability class each measuring point comprises at least 5 runs (usually much more). The ratio ( $R$ ) of the wind speed at height  $z$  to that at 200 m has been calculated by fitting the equation  $U_z = R \times U_{200}$  using a  $\chi^2$ -procedure. The uncertainty in  $U$  is assumed to be 10% in this analyses, with the uncertainty of the 10% percentile wind speed in the data set as a minimum.

From the velocity profiles it can be seen that the retardation of the wind speed is the strongest in the south sector and not in the east sector, which is usually considered to be the roughest sector. In the north sector the retardation is comparable to that of the west sector, which is considered to be the smoothest. Also evident is the strong curvature in these profiles, especially in stable conditions. At 40 m, in (slightly) unstable and slightly stable conditions a knee in the velocity profile can be seen in the west sector suggesting a rough-to-smooth transition in surface roughness.

Ratios of friction velocity measured by k-vanes to that of the surface layer are plotted

in Fig. 3.3. In the unstable, well mixed, ABL  $u_{*kv}$  is close to  $u_{*SL}$  and can be considered approximately constant with height. The relative momentum flux divergence increases with increasing stability. In the stable ABL  $u_*$  at 180 m has decreased to 50% of its surface value. The divergence is probably due to the finite depth of the ABL. In the east direction  $u_{*kv}$  at 20 m is larger than  $u_{*SL}$  for all stabilities. In this direction the upstream fetch is heavily disturbed close to the tower. This is reflected by the  $u_{*kv}$ -measurements, while  $u_{*SL}$  represents a large-scale friction velocity. In west and in the south direction  $u_{*kv}$  is smaller than  $u_{*SL}$  at 20 m. In these directions there are few obstacles in the towers vicinity.

In general Monin-Obukhov similarity theory is based on the assumption that momentum and heat fluxes do not change throughout the surface layer, and the surface layer is defined as the ‘constant flux layer’. Fig. 3.3 shows that there is a strong momentum flux divergence, except for the unstable cases. A strong divergence was also found for the sensible heat flux (Fig. 3.4). The daytime flux divergence (unstable conditions) may partially be caused by entrainment. The data selection excludes low wind speed and consequently low  $u_*$ -values to ensure that the k-vanes are operating properly. Moreover, the data set includes many situations with unstable, shallow boundary layers in the early morning hours with a growing convective boundary layer. These conditions are in favor of strong entrainment and the entrainment heat flux can be about 20–50% of the surface heat flux (Driedonks and Tennekes, 1984; Pino et al., 2003). With an ABL-height of 500 m the heat flux may become zero at a height of only 400 m. The application of the surface layer criteria of Korrell et al. (1982) indicates that indeed the ABL has often been shallow and a significant portion of the measurements are done above the surface layer, where the momentum and heat fluxes are expected to decrease. Under such conditions we can not expect that Monin-Obukhov similarity theory is still applicable.

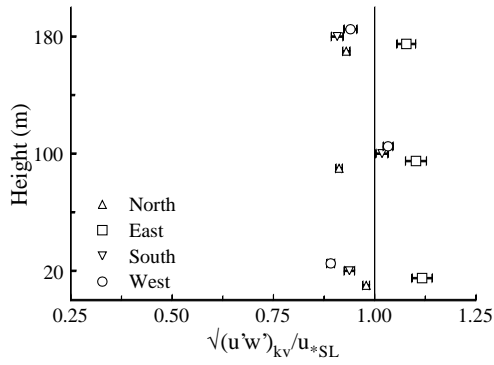
Let us explore the dimensionless wind speed gradient using  $\partial U/\partial z$  from the tower measurements:

$$\phi_m \left( \frac{z}{L} \right) = \frac{kz}{u_*} \frac{\partial U}{\partial z}. \quad (3.1)$$

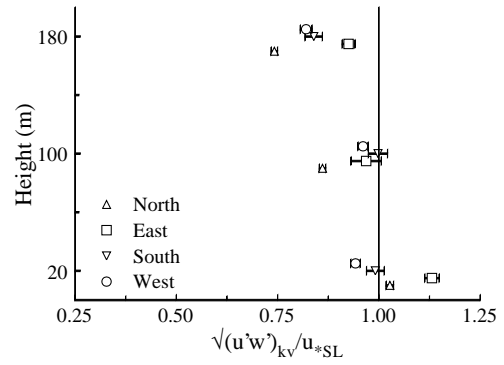
Here we analyze our data by using both the local values for  $u_*$  and  $L$  (so called local scaling) as well as the surface layer values for  $u_*$  and  $L$ . Since the fluxes become smaller with height and the scatter increases as well, only the k-vane fluxes at 20 and 100 m are analyzed. Following Nieuwstadt (1984) the wind speed profile is fitted to the function  $U = a_1 + a_2z + a_3z^2 + a_4 \ln z$ . From this fitted profile  $\partial U/\partial z$  is computed at 20 or 100 m. The averages of  $z/L$  and  $\phi_m$  are plotted in Figs. 3.5a and 3.5c for the surface layer scaling results. The data have been averaged in bins each containing 20 runs. The standard deviation of the mean of  $\phi_m$  has been plotted as error bar. For comparison Dyer’s (1974) stability function is also plotted. In addition to the usual data selection, positive wind speed gradients were required ( $\partial U/\partial z > 0$ ), and cases with  $u_* < 0.15 \text{ m s}^{-1}$  were rejected to ensure that  $\phi_m$  is well defined.

At 20 m  $\phi_m$  is lower than Dyer’s curve. Only in the south direction, the most complex and rough sector, in unstable conditions  $\phi_m$  is larger than Dyer’s curve. With increasing stability the difference between  $\phi_m$  and Dyer’s curve increases. At 100 m there are less measuring points, especially in the east sector there are few. The scatter in the data is also larger. In all directions  $\phi_m$  has increased compared to the 20-m level. In the north and west direction  $\phi_m$  is still close to Dyer’s curve for neutral and unstable cases. In the south sector  $\phi_m$  is far above Dyer’s curve over the whole range of stabilities.

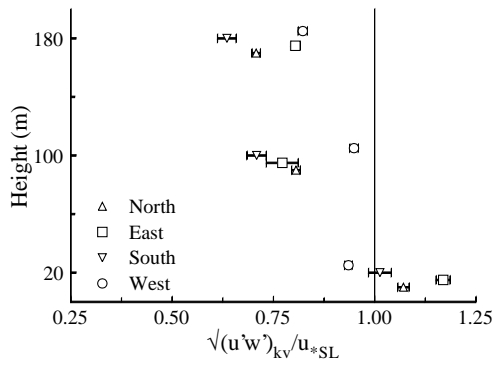
In Eq. 3.1  $u_*$  and  $L$  can also be computed from the k-vane measurements (local scaling). As shown in Figs. 3.5b and 3.5d local scaling reduces the scatter in  $\phi_m$  considerably. At



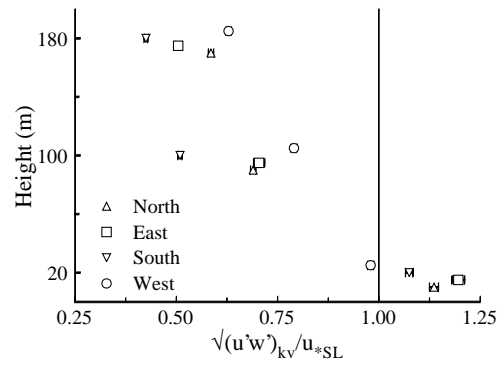
(a) Unstable,  $1/L < -0.005 \text{ m}^{-1}$



(b) Slightly unstable,  $-0.005 \text{ m}^{-1} < 1/L < 0$

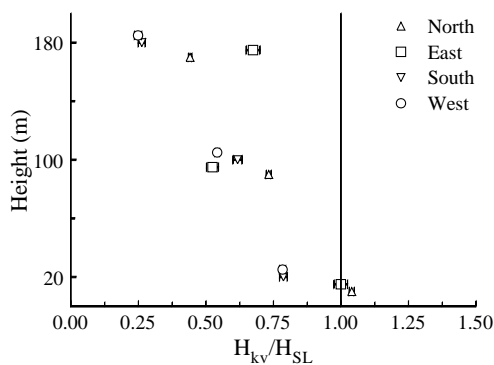


(c) Slightly stable,  $0 < 1/L < 0.005 \text{ m}^{-1}$

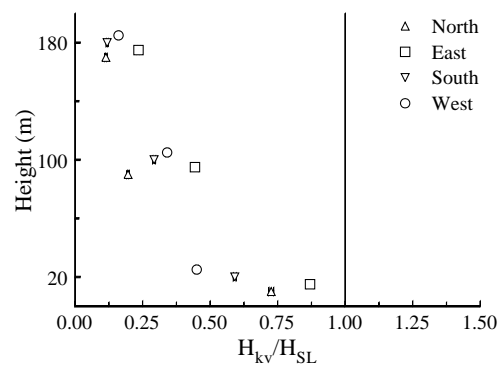


(d) Stable,  $1/L > 0.005 \text{ m}^{-1}$

Figure 3.3: Friction velocity as measured by the k-vanes normalized with the surface layer friction velocity.

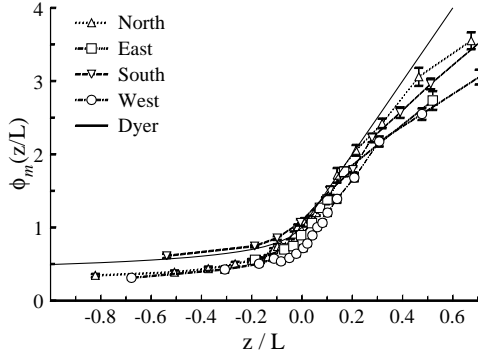


(a) Unstable,  $1/L < -0.005 \text{ m}^{-1}$

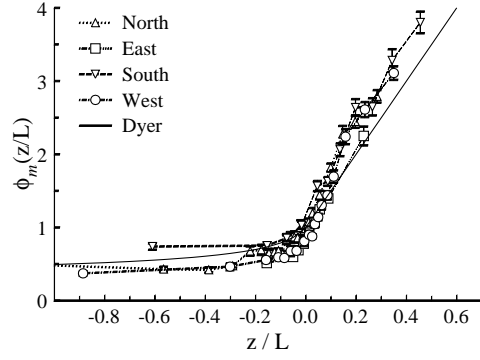


(b) Stable,  $1/L > 0.005 \text{ m}^{-1}$

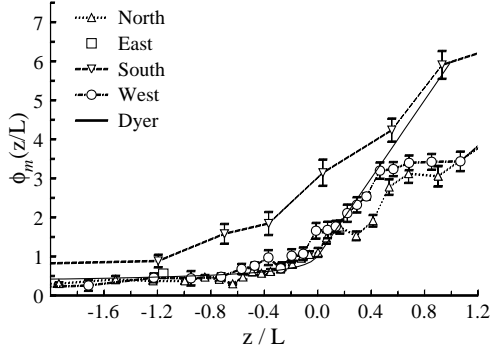
Figure 3.4: Sensible heat flux as measured by the k-vanes normalized with the surface layer heat flux.



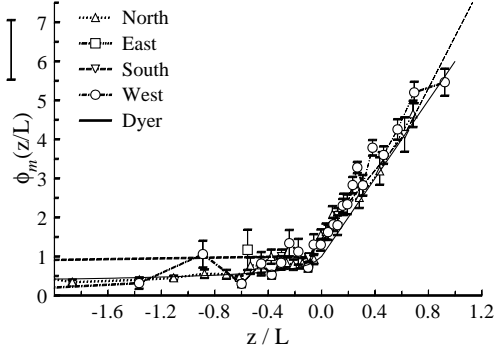
(a) Surface layer scaling; 20 m



(b) Local scaling; 20 m



(c) Surface layer scaling; 100 m



(d) Local scaling; 100 m

Figure 3.5: Dimensionless wind speed gradients calculated from k-vane fluxes at 20 and 100 m for the four wind direction sectors. Note that  $u_*$  and  $L$  are calculated from the surface layer fluxes (a and c), and from the fluxes measured by the k-vane itself (b and d).

both 20 and 100 m  $\phi_m$  collapses to a single curve, also for the south sector. In neutral and unstable cases  $\phi_m$  is still below Dyer's curve at 20 m. Although the fluxes at 20 m are still close to their surface layer values, Fig. 3.5b shows that local scaling performs slightly better, especially in stable cases. Fig. 3.5d shows that at 100 m local scaling performs much better than surface layer scaling. Figs. 3.3a and 3.4a show that at 100 m the difference between surface-layer scaling and local scaling is primarily caused by the difference in heat flux.

Note that  $\phi_m$  and  $z/L$  both contain the factor  $\kappa z/u_*$  (see Eq. 3.1). Consequently the correlation that is found in Fig. 3.5 may partially be an artifact. In Fig. 3.6  $dU/dz$  is plotted against  $(u_*/\kappa z)(z/L) = \kappa u_*/L = (g/\theta)\overline{w'\theta'}/u_*^2$  for the 100-m level for surface layer- and local scaling. This way of plotting is free of artificial correlation. Fig. 3.6 confirms that the good performance is not artificial and that there is less scatter when local scaling is used.

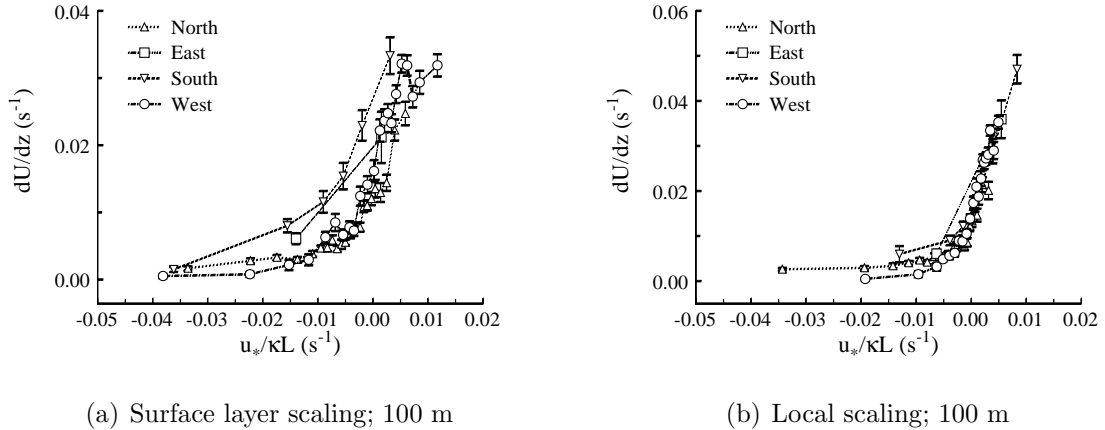


Figure 3.6: As Fig. 3.5 but now for the wind speed gradient  $dU/dz$  versus  $u_*/\kappa L$ . In this plot any artificial correlation is avoided.

## 3.6 Roughness lengths

In this section several methods to determine the aerodynamic roughness length ( $z_0$ ) are compared. The roughness length can be computed from wind speed profiles, gustiness analysis, and the drag coefficient. All these methods may result in different estimates of  $z_0$  as they have different source areas.

The footprint or source area is the surface effectively determining the level or gradient of a meteorological parameter downstream. It can be described by sophisticated weighting functions and is a function of height, stability, and roughness itself. In neutral conditions the area with the maximum contribution lies upwind at a distance of about ten times the measuring height. The width of the source area is about  $20^\circ$ – $30^\circ$ . Atmospheric instability shrinks the source area and makes it come closer (Van Ulden, 1978; Schmid and Oke, 1990; Horst, 1999; Schmid and Lloyd, 1999; Kljun et al., 2004).

The larger the source area of a meteorological parameter, the more this entity will represent a large-scale average. The largest eddies in the ABL are also those that adapt slowest of all to changes in surface properties (Højstrup, 1981; Beljaars, 1987b). The longitudinal velocity variance in the surface layer ( $\sigma_u^2$ ) is mostly determined by the largest eddies. For that reason  $z_{0\text{std}}$  represents the best large-scale average of all roughness lengths.

### 3.6.1 Roughness lengths from Profiles

Using Nieuwstadt's (1978) method the wind speed profile at Cabauw is analyzed as function of wind direction. Nieuwstadt minimized the function

$$\Phi(u_*, \theta_*) = \Phi_u / \Delta u^2 + \Phi_\theta / \Delta \theta^2, \quad \text{where} \quad (3.2)$$

$$\Phi_u = \sum_{i=2}^{N_U} [U_{z_i} - U_{z_{\text{ref}}} - u(z_i, u_*, \theta_*) + u(z_{\text{ref}}, u_*, \theta_*)]^2, \quad (3.3)$$

and

$$\Phi_\theta = \sum_{j=2}^{N_\theta} [\theta_{z_j} - \theta_{z_{\text{ref}}} - \theta(z_j, u_*, \theta_*) + \theta(z_{\text{ref}}, u_*, \theta_*)]^2. \quad (3.4)$$

Here  $\Delta u$  and  $\Delta\theta$  are the measuring errors in the wind speed  $U$  and temperature  $\theta$  respectively, and  $\theta_* = -H/\rho c_p u_{*prof}$  is the temperature scale, where  $u_{*prof}$  is the profile derived friction velocity,  $u(z, u_*, \theta_*)$  and  $\theta(z, u_*, \theta_*)$  are the log-linear functions for wind speed and temperature and  $N_U$  and  $N_\theta$  are the number of heights at which wind speed temperature are measured respectively. The subscript ‘ref’ refers to the lowest level used in the profiles. Nieuwstadt used estimates of  $z_0$  and added  $U(z_0) = 0$  to his profile. We will not do so, as the profiles are used to determine  $z_0$ . Dyer’s (1974) stability functions and the integrated log-linear functions  $\Psi_M$  and  $\Psi_H$  as presented by Garratt (1992) are adopted here. For  $U$  the total horizontal wind vector has been used. The fitted wind speed profile is extrapolated to  $U(z_0) = 0$  to derive the roughness length. Any zero plane displacement, which is expected to be small and of minor importance when computing  $z_0$ , is neglected (Nieuwstadt, 1978; Kustas and Brutsaert, 1986; Grant and Mason, 1990; Grant, 1991). In addition to the basic selection criteria, we applied the criteria of Korrell et al. (1982) as well, to ensure all profiles were within the surface layer and we analyzed only the slightly unstable cases.

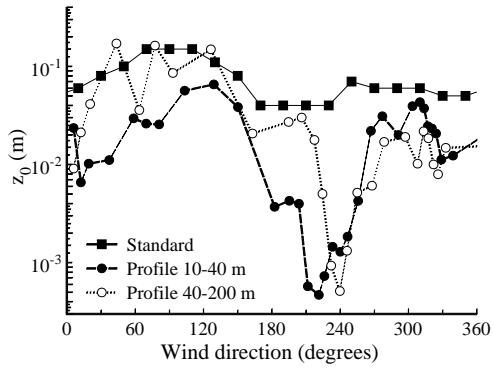
In Fig. 3.7a the resulting roughness lengths  $z_{0prof}$  are plotted. It is computed using two different height intervals: 10–40 m and 40–200 m. Every point represents the average over 30 estimates of  $z_{0prof}$ . For comparison  $z_{0std}$  is plotted as well. Fig. 3.7a shows that the higher profile yields similar roughness lengths to  $z_{0std}$  in most directions where, apparently, the 40-m level is not influenced by the rough to smooth transition close to the tower for those directions. Only in the south-west sector  $z_{0prof}$  drops to values that are far too low to be realistic. In this direction the roughness length is smaller than 1 mm. Such small roughness lengths can only be found over very smooth surfaces (water, sand, snow covered land). This indicates that the profiles in this sector at Cabauw are strongly disturbed. The lower profile yields smaller roughness lengths than the higher profile except for the sectors from west to north. This profile also yields very  $z_0$ -values in the south-west direction. In most directions the free fetch is not long enough, less than a few hundreds of meters, to accelerate the 10-m wind. However, in the south-west direction the fetch is longer (0.5–2 km), resulting in a very low estimate of  $z_{0prof}$ . The low  $z_{0prof}$  in the upper profile shows that the local IBL has reached the 40-m level in the direction  $240^\circ$ . The unrealistically low  $z_0$ -values in the lower profile, however, show the equilibrium boundary layer has not reached the 40-m level in this direction yet. Fig. 3.7a also shows that directions with distinct roughness values can be very narrow. This indicates that the source areas for these measurements are very narrow as well.

### 3.6.2 Roughness lengths from the drag coefficient

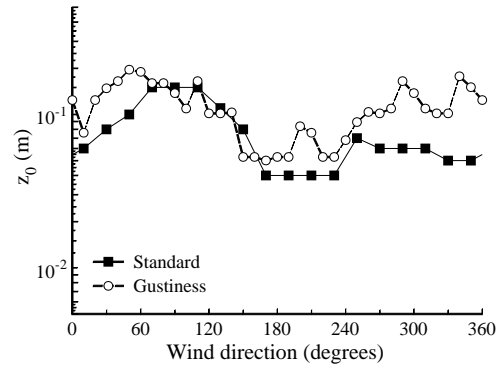
The drag coefficient,  $C_d \equiv (u_*/U)^2$ , can be used to estimate the roughness length using the logarithmic wind speed profile. From the logarithmic wind speed profile it follows that  $C_d$  is a function of  $z$ ,  $z_0$ , and stability:

$$\sqrt{C_d} = \frac{\kappa}{\ln z/z_{0drag} - \Psi_M(z/L) + \Psi_M(z_{0drag}/L)}. \quad (3.5)$$

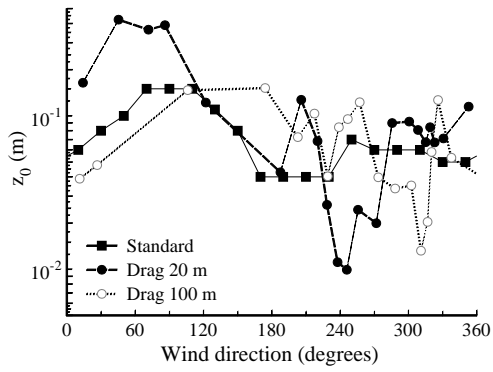
An advantage of this approach is that measurements need to be done only at a single level. A disadvantage is the need for measurements or estimates of the momentum flux. Fortunately,  $u_*$  can be estimated from  $\sigma_u$  or the gustiness. Both can be assessed by regular anemometers. The routine Cabauw roughness length as shown in Fig. 3.7a is an example of the application of this method. Gustiness records have been available since the early



(a) Roughness lengths from profile measurements using different height intervals compared to  $z_{0std}$ .



(b) Roughness lengths from gustiness measurements at 10 m compared to  $z_{0std}$ .



(c) Roughness lengths from the drag coefficient measurements at 20 m and 100 m compared to  $z_{0std}$ .

Figure 3.7: Roughness lengths estimated using various methods at the Cabauw site.

seventies at most Dutch wind stations. These records proved very useful in wind climate research to monitor the quality of stations (Wieringa, 1976; Verkaik, 2000).

From the present data set the roughness lengths found from direct observations of  $u_*/U$  or the gustiness can be compared to those from  $\sigma_u$ . The gustiness derived roughness length ( $z_{0\text{gust}}$ ) has been calculated using the routine measurements at 10 m per  $10^\circ$ -wide bins. In Fig. 3.7b  $z_{0\text{gust}}$  is plotted and compared to  $z_{0\text{std}}$ . For most directions  $z_{0\text{gust}}$  is similar or larger than  $z_{0\text{std}}$ . Compared to  $z_{0\text{prof}}$  it shows very little directional variation.

Using the k-vane measurements at 20 and 100 m  $z_{0\text{drag}}$  has been calculated. The same data selection as for the profiles has been done. In Fig. 3.7c  $z_{0\text{drag}}$  is plotted. The directional variation in  $z_{0\text{drag}}$  is larger than that of  $z_{0\text{std}}$  and  $z_{0\text{gust}}$ . It is possible to indicate the surface features causing the profile of  $z_{0\text{drag}, 20\text{m}}$ . The peak in the north-east direction is caused by farms and trees at 300 m distance. The peak at  $190^\circ$  is caused by trees and orchards (0.5–1.5 km). A little more to the south of that there is a small window overlooking the river bed. This is a very smooth area. In the south-west direction roughness lengths in the order of centimeters are found. This roughness length corresponds to that of grassland and this direction is also the direction with the largest free fetch over grassland.

At 100 m  $z_{0\text{drag}}$  is in the range 0.01–0.10 m for most directions. The 100-m roughness length shows a noisy profile in the west directions. However, assuming that the 100-m observation are not influenced by the closest windbreaks, the low  $z_0$  in direction  $300^\circ$  coincides with a very smooth upwind fetch starting  $\simeq 1$  km from the tower (see Fig. 3.1). The low  $z_0$  in the north direction, however, cannot be explained easily. In the east direction  $z_0$  is clearly smaller at 100 m than at 20 m, indicating that the 100-m footprint is mainly overlooking the village Lopik in the east.

## 3.7 Discussion

### 3.7.1 Flux-profile relationships

At 20 m  $\phi_m$  is lower than Dyer’s curve in most directions when using surface layer scaling. When using local scaling in unstable cases  $\phi_m$  is lower as well. A low  $\phi_m$  indicates that  $\partial U/\partial z$  is small compared to  $u_*$ , typical for situations after a rough-to-smooth change (Rao et al., 1974). Fig. 3.5a can be compared with figures 5 and 7 from Beljaars et al. (1983) where also low values for  $\phi_m$  were found.

Deviations of the regular flux-profile relationships in very stable conditions using surface layer scaling have been observed frequently. Local scaling has been more successful in these cases (Holtslag and Nieuwstadt, 1986; Holtslag and De Bruin, 1988; Beljaars and Holtslag, 1991; Vickers and Mahrt, 1999). Local scaling can also be applied to  $\phi_m$  in unstable condition at homogeneous sites (Sorbjan, 1986; Yumao et al., 1997). Fig. 3.5b and 3.5d however, show that local scaling of  $\phi_m$  also applies in the disturbed boundary layer at Cabauw. If the underestimation of  $\phi_m$  at 20 m is explained by the rough-to-smooth transition, then Fig. 3.5d shows that at 100 m the flux-profile relationships seem to reflect an equilibrium ABL as long as local scaling is applied.

Comparing eddy-correlations measurements at 3.5 and 22.5 m Beljaars et al. (1983) found that there is an increase in friction velocity with height, except for those directions which are really free of obstacles. Heat and moisture fluxes are about the same at both levels for all directions. These observation confirmed the assumptions of Beljaars (1982), firstly, the heat flux throughout the surface layer is constant in spite of perturbed profiles,

and, secondly, the exchange coefficients for momentum and heat are modified in the same way by obstructions. The success of local scaling suggests that these reasonings still hold at 100 m and despite the strong flux divergence.

Our data selection for unstable conditions is in favor of situations with developing boundary layers in the morning hours in combination with wind shear. The strong heat flux divergence in unstable conditions indicates that the boundary layer is heating up (Fig. 3.4). Moreover, the entrainment rate is expected to be relatively high (Pino et al., 2003), so the heat flux becomes negative at a relatively low height. Whereas the heat flux becomes negative by entrainment in the upper part of the ABL, the momentum flux is enhanced. This explains why, in contrast to the heat flux, there is little divergence in momentum flux (Fig. 3.3).

### 3.7.2 Wind speed profiles and Local roughness

The rough-to-smooth transition at Cabauw causes a knee in the wind speed profile. The knee is best seen in the west sector (Fig. 3.2), where the extent of the obstacle-free fetch is large enough for the the IBL to reach the 20-m level. For most directions the present data set is too coarse to do a detailed analysis of the IBL-structure of the Cabauw site. From earlier research it was found that near-neutral wind speed profiles at Cabauw show a knee around 20 m in the south-west direction, and around 10 m in the east direction. Both the lower and upper part of the profile is logarithmic (Beljaars, 1982). Wieringa (1976) reported that the upper profiles corresponded to the gustiness derived roughness lengths. This is confirmed by Fig. 3.7b.

At Cabauw the friction velocity is routinely computed from the large-scale roughness  $z_{0\text{drag}}$  and the wind speed at 10 m. For most directions this method is accurate. However, in the south-west sector the 10-m wind is well within the local IBL. Here the wind speed is adapted to the smooth grass-covered land, whereas the roughness length still represents the high, large-scale average. This results in an overestimation of the friction velocity and hence the wind speed (gradient) as was seen in Nieuwstadt (1978).

Nieuwstadt (1978) compared the friction velocity from his profile method with direct flux measurements at 20 m. The large-scale roughness length  $z_{0\text{std}}$  was added to the profile ( $U(z_0) = 0$ ). For most directions the profile  $u_*$  and the directly measured  $u_*$  were in agreement. However, for the south-west direction the directly measured  $u_*$  was smaller than that from the profiles. Nieuwstadt used  $z_0 = 0.07$  m for this direction. He suggested that the roughness length used in this direction was too high. Actually, the roughness length Nieuwstadt used was not too high, but it corresponded only to the upper profile and so did the estimated  $u_*$ . The 20-m level is within the local IBL in this direction and the measured  $u_*$  does not correspond to the upper profile.

Meteorological research masts are often placed at sites selected for their undisturbed terrain. Therefore the local roughness is usually smaller than the large-scale roughness. Cabauw is such an example, but at Boulder similar results are found (Korrell et al., 1982; Bowen, 2000).

### 3.7.3 Roughness footprints

Significant differences in roughness length are found from different height intervals for wind speed profiles, or when the roughness length is computed from the gustiness, turbulence intensity, or the drag coefficient. The differences have to be explained by the differences in

footprint between these methods in combination with the inhomogeneities of the Cabauw environment.

The source area for the 10–40 m profile is expected to be similar to those for eddy-covariance measurements done at  $\sqrt{z_{\text{high}}z_{\text{low}}} = 20$  m. Its source area weight function is falling off rapidly at a distance of 0.5–1 km (Horst, 1999). On this scale the Cabauw environment is very disturbed resulting in a very changeable lower profile  $z_{0\text{prof}}$  (Fig. 3.7a). The  $z_{0\text{drag}}$  is much less changeable with direction (Fig. 3.7c). Only in the south-west direction, where the IBL over smooth grass encloses the 20-m level,  $z_{0\text{drag}}$  represents the local roughness of grass. A similar difference in momentum flux between 3.5 and 22.5 m height was found by Beljaars et al. (1983). Later Schmid and Oke (1990) showed that the source area for the 22.5-m level comprises many obstacles upstream, while for the 3.5-m level the source area is much smoother. So, although the footprints of  $z_{0\text{drag}}$  and the lower  $z_{0\text{prof}}$  are expected to be similar, the lower  $z_{0\text{prof}}$  is corrupted by the wind speed at 10 m which will be enclosed in the local IBL in more directions than the 20-m level. The 20-m level  $z_{0\text{drag}}$  on the other hand, yields local roughness lengths only if the IBL reaches to that level, and yields large-scale roughness lengths otherwise.

From the spectral point of view gusts are the result of the superposition of several eddies of different sizes. Whereas the largest eddies contribute most significantly to  $\sigma_u$ , the gust is also determined by smaller eddies because of the small time scale of gusts. This means that the source area for  $z_{0\text{gust}}$  may also be a superposition of large-scale and local roughness. Fig. 3.7c shows that  $z_{0\text{gust}}$  is exceeded by  $z_{0\text{drag}}$  in directions where nearby roughness is present. In other directions it is comparable to  $z_{0\text{std}}$ . There seems to be a correlation, however, between  $z_{0\text{gust}}$  and  $z_{0\text{drag}}$ : every peak in  $z_{0\text{drag}}$  is accompanied by a peak in  $z_{0\text{gust}}$ . So, the footprint of  $z_{0\text{gust}}$  seems to be superposition of local and large-scale roughness indeed, and its footprint is larger than that of  $z_{0\text{drag}}$ .

### 3.8 Summary and Conclusions

The findings of this paper show that the k-vanes are capable of measuring momentum fluxes with sufficient accuracy provided that they are not used at low altitudes. However, the k-vanes proved vulnerable to atmospheric electricity and contamination of the bearings supporting the propellers.

Overall this study confirms the conclusions of earlier studies at Cabauw. In addition we have analyzed fluxes and wind profiles along the tower not explored before up to heights of 100 m. The wind speed profiles in the Cabauw environment are disturbed by the rough-to-smooth transition that can be found in all directions eventually. Only in the south-west direction the free-fetch extends so far that the equilibrium boundary layer over the grass covered land reaches high enough to enclose the flux measurements at 20 m.

Except for unstable cases the momentum flux in our data selection shows significant divergence. The heat flux divergence is even more pronounced. Our data set comprises many cases where the measurements are done above the surface layer. In addition, in unstable conditions the entrainment rate can be expected to be large. This is due to our data selection procedure which is in favor of conditions with developing boundary-layers in the morning hours with significant shear. It is reconfirmed that in stable boundary layers the regular flux-profile relationships are valid provided that local scaling is used. Also in unstable conditions it appears that scaling of the profiles with local fluxes works well, even in directions where the upstream terrain causes strong disturbances of the boundary layer.

We analyzed the roughness lengths using three methods. This showed that every method has his own footprint resulting in every different estimates of the roughness length depending on the method used. The roughness lengths derived at Cabauw from wind speed profiles depend strongly on the height range over which the profile is taken. The lower profiles ( $< 40$  m) are disturbed by the IBL caused by the local rough-to-smooth transition. Roughness lengths from these profiles are completely invalid. The higher profile yields roughness lengths that can be considered area-averaged values, provided that the lower measuring points are not disturbed by the local IBL. Gustiness derived roughness lengths seem to aggregate both nearby and distant roughness elements and is often the largest of the roughness estimates examined here. The roughness from drag coefficients exhibits more local characteristics than the gustiness. However, if the drag coefficient is measured above the local IBL it yields roughness values that are close to the large-scale area-average. At inhomogeneous sites like Cabauw the roughness length can be estimated best by measuring the drag coefficient just above the local internal boundary layers. Indirect ways for determining the drag coefficient like measurements of the gustiness or the standard deviation of horizontal wind speed fluctuations give similar results. These methods are less sensitive to local disturbances of the surface layer than profile derived roughness lengths. The latter are easily disturbed by terrain inhomogeneities resulting in unrealistic values for the roughness lengths.

## Acknowledgments

This project was undertaken by the Meteorology and Air Quality Section of Wageningen University (WU) in collaboration with the Royal Netherlands Meteorological Institute (KNMI). It was originally initiated under the supervision of Prof. Dr. J. Wieringa. We are indebted to the technical staff of both KNMI (Sjaak Koster and Frans Renes among others), and WU (Bert Heusinkveld and Frits Antonysen among others), for helping setting up the k-vane measurements. Also thanks to the scientific staff of the Atmospheric Research group of KNMI for making available the profile data. Special thanks to Fred Bosveld for providing the data-acquisition software. The investigations were (in part) supported by the Netherlands Organization for Scientific Research (NWO), project no. 750.194.15.

# Chapter 4

## Evaluation of Two Gustiness Models for Exposure Correction Calculations

Published in *Journal of Applied Meteorology* **39**, p. 1316–1326, 2000.

### Abstract

Gustiness models from Wieringa and Beljaars are evaluated. The models are used to relate the gustiness from wind speed records to the local roughness length. The roughness length is used to apply exposure corrections to sheltered wind stations. The gustiness models are mutually compared and the influence of measuring chain inertia and the measuring period on the measured gusts is evaluated. Beljaars's model is used to estimate the wind speed at elevated levels from wind speed and gustiness records measured close to the surface. Uncertainties in the computation of roughness lengths from gustiness records are also evaluated. For measuring periods of one hour the exposure corrections from the two models are equal over smooth terrain. Over rough terrain Beljaars's gustiness model yields smaller corrections, differences up to 10% are possible. For 10-min periods Beljaars's corrections are 3–10% smaller than those of Wieringa. Other uncertainties, resulting from the assumption of neutral stratification and a value for the blending height, are smaller than 5%.

### 4.1 Introduction

When wind speed observations measured at different locations are compared, corrections for differences in site exposure are necessary. For this purpose, information on the local roughness or the distribution of obstacles and roughness patches in the station's environment is a prerequisite. Different methods for site exposure corrections are available. Wieringa (1986; 1996) used observed gustiness data for exposure correction computation. When detailed information on the station's environment is available, it can be used to estimate the local wind speed profile. This was done, for example by Wolfson and Fujita (1989), using obstruction angles as measured from panoramic photographs. Troen and Petersen (1989) developed a method with inclusion of an internal boundary layer model which make the method applicable in regions downwind of major roughness changes, e.g. the coastal zone. Miller et al. (1998) use a combination of an internal boundary layer model, a model

for topographic effects and an altitude factor to correct the UK anemographs for site exposure. A problem is that the station's environment may change in time. Growing trees or approaching built-up areas may cause a gradual increase in surface roughness. For climatological records of wind speed these changes are usually poorly documented.

An abundance of information on the local boundary layer structure can be extracted from raw turbulence data, even when measured at a single height (Sozzi et al., 1998). For operational meteorological stations this kind of data will generally not be available. Roughness lengths can also be derived from profile measurements of average wind speed when these are available for the site of interest. This will usually not be the case for regular meteorological stations, however.

The roughness at a meteorological site can be deduced from the turbulent wind speed fluctuations. In the neutral, homogeneous surface layer the horizontal wind speed  $U$  is a logarithmic function of height  $z$  (Tennekes, 1973)

$$U = \frac{u_*}{\kappa} \ln \frac{z}{z_0}, \quad (4.1)$$

where the von Karman constant  $\kappa = 0.4$  (Frenzen and Vogel, 1995b), and  $u_*$  is the friction velocity, related to the momentum flux,  $u_*^2 = -\overline{u'w'}$  ( $u'$  and  $w'$  are turbulent fluctuations of the horizontal and vertical wind speed respectively). In surface layers over homogeneous terrain  $z_0$  is well defined and  $u_*$  is constant with height. The standard deviation of horizontal wind speed  $\sigma_u$  scales with  $u_*$  and is a function of stability ( $L$ , Monin-Obukhov length) and the boundary layer height ( $z_i$ )

$$\sigma_u/u_* = c(z/L, z_i/L), \quad (4.2)$$

with  $c \simeq 2.2$  in the neutral limit ( $|L| \rightarrow \infty$ ). When  $\sigma_u$  and  $U$  are measured simultaneously, combination of Eqs. 4.1 and 4.2 yields the roughness length. Horizontal wind speed fluctuations in the surface layer are partially generated locally through mechanical turbulence, and are partially the result of eddies with the size of the boundary layer height. Since large eddies adjust only slowly to new surface properties,  $\sigma_u$  is influenced by an upwind fetch with the magnitude of the boundary layer height (Højstrup, 1981; Beljaars, 1987b).

Climatological records of wind speed usually do not include  $\sigma_u$ -observations. Only recently Automatic Weather Stations (AWS) do record  $\sigma_u$ , and this will simplify the computation of exposure corrections considerably in the future. Earlier data sets provide gustiness measurements only. This is the only parameter that has been recorded routinely at meteorological stations that carries turbulence information.

Wieringa's gustiness model, presented in Wieringa (1973; 1976; 1977), was explicitly derived for the purpose of exposure corrections and applied in the wind climate assessment of the Netherlands (Wieringa and Rijkoort, 1983). However, this model cannot be used when the wind speed is discretely sampled, as is the case at the stations of the Royal Netherlands Meteorological Institute (KNMI) since the early 90's. Beljaars's model, presented in Beljaars (1987a; 1988), seems a good alternative for Wieringa's model, but Beljaars did not use his model for site exposure corrections. The purpose of the present paper is to compare the two models and assess the possible difference in resulting roughness and exposure correction estimates. Gustiness data from three inland stations in the Netherlands are analyzed. Exposure corrections are necessary when the station's environment is inhomogeneous. Strictly speaking the application of Monin-Obukhov similarity theory (M-O theory) is not appropriate over inhomogeneous terrain, but for want of something better

it will be used throughout this paper. Wieringa assumes a Gaussian distribution for the instantaneous wind speed ( $U(t)$ ) and Beljaars assumes that  $U(t)$  and its time derivative ( $\partial U/\partial t$ ) are joint Gaussian. Turbulence in the atmospheric boundary layer is not fully Gaussian as  $\partial U/\partial t$  is not normally distributed (Panofsky and Dutton, 1984). Kristensen et al. (1991) argue, however, that  $U(t)$  and  $\partial U/\partial t$  are uncorrelated and that their joint probability may still be Gaussian.

The present study is a contribution of KNMI to the HYDRA-project (RIKZ<sup>1</sup>/RIZA<sup>2</sup>). In the HYDRA-project the hydraulic boundary conditions are assessed for safety testing of the Dutch dams. Updating of the Dutch wind climate assessment by Wieringa and Rijkoort (1983) is one of the main goals of the KNMI contribution.

## 4.2 Exposure correction

Exposure corrections can be made when the local roughness length is known (Wieringa 1976, 1977, 1986, 1996, Oemraw 1984), as will be explained next. The measured wind speed  $U_m$  at height  $z_m$  is extrapolated from the surface to a level  $z_b$  using the logarithmic velocity profile (Eq. 4.1). The wind speed at  $z_b$  ( $U_b$ ) is assumed to be horizontally constant, and the level  $z_b$  is therefore called the “blending height”: the effects of all surface inhomogeneities have blended into the mean flow. The wind speed at the blending height can be estimated from

$$U_b = U_m \frac{\ln z_b/z_0}{\ln z_m/z_0}. \quad (4.3)$$

This wind speed can now be used to calculate the “potential wind speed”: the wind speed at  $z_{\text{ref}} = 10$  m height over open terrain (grass,  $z_{0\text{ref}} = 0.03$  m):

$$U_p = U_b \frac{\ln z_{\text{ref}}/z_{0\text{ref}}}{\ln z_b/z_{0\text{ref}}}. \quad (4.4)$$

The potential wind speed is a reference wind speed, free of local effects. The exposure correction factor  $S$  is given by the ratio of  $U_p/U_m$ :

$$S = \frac{U_p}{U_m} = \frac{\ln z_b/z_0}{\ln z_m/z_0} \frac{\ln z_{\text{ref}}/z_{0\text{ref}}}{\ln z_b/z_{0\text{ref}}}. \quad (4.5)$$

In Figure 4.1 the wind speed profiles are plotted for the case  $z_0 = 0.5$  m,  $z_m = z_{\text{ref}} = 10$  m, and  $z_b = 60$  m. The uncertainties that are inherent to this method concerning  $z_b$  and the influence of stability on  $U$  and  $c$  are assessed in section 4.7. As was already stated, M–O theory is used even though this may not be quite exact over heterogeneous surfaces.

In the process of exposure correction computation, gustiness analysis is an additional step to come to the ratio  $\sigma_u/U$ . When direct observation of  $\sigma_u$  become available one might expect an increased accuracy in  $z_0$ -estimation. However, Barthelmie et al. (1993) estimated the wind speed at higher level on a mast from the wind speed at 12 m. They compared profile, gustiness, standard deviation methods, and  $z_0$ -evaluation from land-use maps and found that direct measurements of  $\sigma_u/U$  yielded the worst results of all methods.

---

<sup>1</sup>Rijksinstituut voor Kust en Zee = National Institute for Coastal and Marine Management

<sup>2</sup>Rijksinstituut voor Integraal Zoetwaterbeheer en Afvalwaterbehandeling =  
Institute for Inland Water Management and Waste Water Treatment

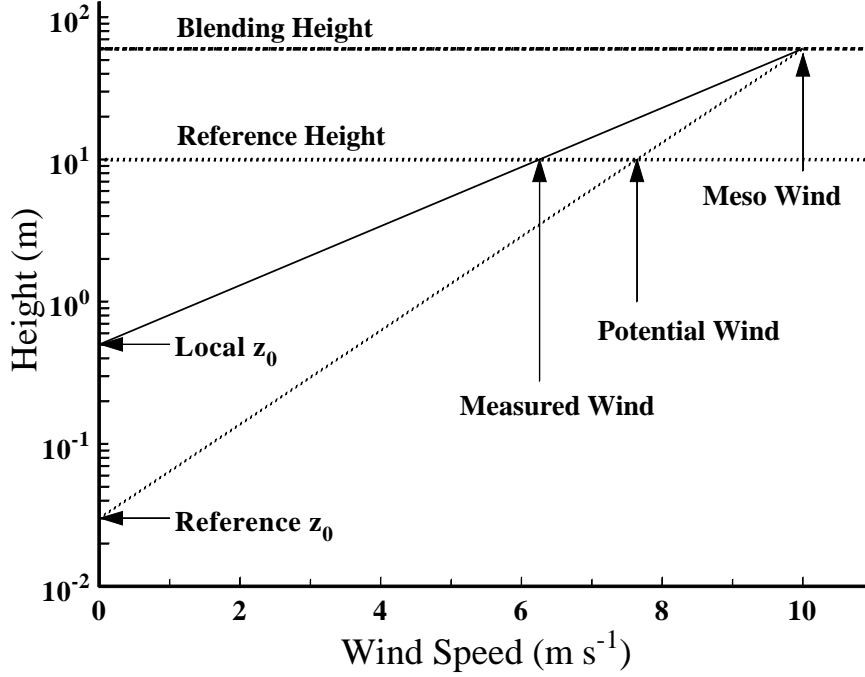


Figure 4.1: Wind speed profile with local  $z_0 = 0.5$  m and  $z_m = z_{\text{ref}} = 10$  m.

### 4.3 Gustiness models

The gustiness parameter  $G$  is defined as follows

$$G \equiv \frac{U_{\text{max}}}{\bar{U}}, \quad (4.6)$$

where  $\bar{U}$  is the average wind speed during the period that the gust  $U_{\text{max}}$  appeared. The normalized gust

$$u_x = \frac{U_{\text{max}} - \bar{U}}{\sigma_u}, \quad (4.7)$$

is solely determined by the variance spectrum of atmospheric turbulence (which is a function of stability), and the anemometer–transmission–recorder system which comprises the “measuring chain”. The measuring chain can be considered as a filter with certain time- and/or length scales, associated with the response length of the anemometer and the response time of the recorder. When neutral stability is assumed and the time- and length scales of the measuring chain are known, the average  $\overline{u_x}$  or median  $\langle u_x \rangle$  of  $u_x$  can be computed. From the logarithmic wind speed profile (Eq. 4.1) and the relation between  $u_*$  and  $\sigma_u$  (Eq. 4.2), we can express  $G$  as function of  $z_0$

$$\frac{\sigma_u}{\bar{U}} = \frac{c\kappa}{\ln z/z_0}, \quad \text{so} \quad (4.8)$$

$$G = 1 + \frac{U_{\text{max}} - \bar{U}}{\bar{U}} = 1 + \frac{\sigma_u}{\bar{U}} \frac{U_{\text{max}} - \bar{U}}{\sigma_u} = 1 + \frac{c\kappa}{\ln z/z_0} u_x. \quad (4.9)$$

Note that if we use  $c = 2.5$ ,  $c\kappa = 1$ . The filtering of the wind speed signal by the measuring chain will modify the shape of the spectrum, attenuating more strongly the

higher frequencies. This effect reduces  $G$  and  $\langle u_x \rangle$ . The inertia of the measuring chain also changes the apparent value of  $\sigma_u/\bar{U}$  by a factor  $A$ . This attenuation can be expressed as  $\sigma_{um}/\sigma_u$ , where  $\sigma_{um}^2$  is the variance that will be transmitted by the measuring chain. As in the gustiness models that will be considered this factor  $A$  is accounted for in different ways, it is not included in Eq. 4.9.

Wieringa (1973) and Beljaars (1987a) derived expressions for  $u_x$ . Wieringa's model has less statistics, only a random-data exceedance criterion with expanded physical modeling, while Beljaars's derivation is more statistically based. Both incorporate the effect of filtering on the measured gustiness, since only gustiness parameters together with a duration or length specification (spatial or temporal filtering) are useful. Wieringa only considers the process of analogue recording, Beljaars discusses also discrete sampling. Next both methods will be outlined.

## 4.4 Wieringa's gustiness analysis

### 4.4.1 The gustiness model

The median gust ( $\langle u_x \rangle$ ) recorded by an anemometer–recorder combination in a certain time period ( $T$ ) has a probability of exceedance of  $1/2N$ , where  $N$  is the number of independent gust observations in period  $T$ . In other words, when again  $N$  gust observations are taken, 50% will have a larger  $u_x$ . For a normal distribution,  $\langle u_x \rangle$  can be expressed as a function of  $N$ . Wieringa (1973) summarizes integral calculations by Parratt (1961):

$$\langle u_x \rangle = 1.42 + 0.301 \ln(N - 4), \quad \text{for } N > 7. \quad (4.10)$$

The number of independent gust observations  $N$  in period  $T$  will be a function of  $T$  and the duration of the gust. As atmospheric turbulence is described with length scales rather than time scale we can also state

$$N \sim \frac{\text{length scale}}{\text{gust length}}. \quad (4.11)$$

Wieringa expressed the gust length as  $\bar{U}t_{\text{gust}}$ . Here  $t_{\text{gust}}$  is the gust duration. Note that the gust length  $\bar{U}t_{\text{gust}}$  is different from  $U_{\text{max}}t_{\text{gust}}$ .

From detrended 1 Hz turbulence measurements over wide open water during strong winds, Wieringa determined values of  $z_0$  and  $G$  resulting in  $N = 87$  and a length scale of 990 m for averaging periods of 10 minutes. He assumed that for extension of  $T$  the turbulence-related parameters  $z$  and  $z_0$  are less relevant, and climatological statistics are adequate for finding the gust factor increase with increasing averaging period. Taking  $\langle u_x \rangle = 1.73$  for  $N = 6$ , and using 10-min sampled experimental wind data with  $(\sigma_u/U) \approx 0.06$  related to 1-h averaging periods, Wieringa scaled the total expression for  $G_{10\text{-min}}$  with a factor  $f_T$ , which is unity for  $T = 10$  min and 1.10 for  $T = 1$  h. Wieringa's final gust model, fitting well to all reliable published  $G$ -data then available, is:

$$\langle G \rangle = f_T \left[ 1 + \frac{1.42 + 0.301 \ln(990 \text{ m}/\bar{U}t_{\text{gust}} - 4)}{\ln z/z_0} \right]. \quad (4.12)$$

Wieringa (1973) was based on high-speed research data, and to account for the slower response of operational anemometry an attenuation factor  $A$  was introduced in later papers

(Wieringa 1976, 1977, 1986). Wieringa also adjusted the length scale from 990 m to 1000 m. For anemometer response length  $\lambda$  and analogue recorder response time  $t_{\text{rec}}$  the attenuation factor is

$$A = [1 + (2\pi\lambda/Ut_{\text{gust}})^2]^{-1/2} [1 + (2\pi t_{\text{rec}}/t_{\text{gust}})^2]^{-1/2}. \quad (4.13)$$

The attenuation should only be applied to fluctuations of wind, so

$$G_{\text{meas.}} - 1 = A(G_{\text{wind}} - 1). \quad (4.14)$$

In context of Wieringa's model the factor  $A$  is not the fraction transmitted variance of  $\sigma_u$ , but the transmission of the measuring chain for gusts with duration  $t_{\text{gust}}$  or length  $\bar{U}t_{\text{gust}}$ .

In period  $T$  gusts of all magnitudes will be present. When gustiness observations are used to calculate  $z_0$ , it is necessary to know the gust length to be used in Eq. 4.12. The damping of gusts due to anemometer and recorder inertia is a function of gust duration: short gusts (large  $G$ ) will be attenuated more strongly than long gusts (small  $G$ ). As a result  $G$  will not increase when  $\bar{U}t_{\text{gust}}$  goes to zero, but, according to Wieringa (1976), there will be a maximum in the recorded  $G$  below which the attenuation by anemometer and recorder becomes dominant. The  $\bar{U}t_{\text{gust}}$  to be used in Eq. 4.12 is the gust length at which the maximum occurs of the product of  $u_x$  and  $A$ :

$$u_x A = \left[ 1.42 + 0.301 \ln \left( \frac{990 \text{ m}}{\bar{U}t_{\text{gust}}} \right) \right] \times [1 + (2\pi\lambda/Ut_{\text{gust}})^2]^{-1/2} [1 + (2\pi t_{\text{rec}}/t_{\text{gust}})^2]^{-1/2}. \quad (4.15)$$

By putting the derivative of this expression to  $t_{\text{gust}}$  at zero, an expression for the gust length can be found. Oemraw (1984) gives calculator programs for deriving  $t_{\text{gust}}(U)$  from  $\lambda$  and  $t_{\text{rec}}$ , Wieringa (1976; 1980a) gives nomograms for finding  $t_{\text{gust}}$  from such calculations. Typically in Wieringa's model the gust duration will be one or two orders of magnitude larger than the response time of the recorder, depending on  $U$ .

#### 4.4.2 Comments on Wieringa's model

The following must be noted concerning Wieringa's gust model. When the probability density distribution of wind speed is Gaussian,

$$P(U) = \frac{1}{\sigma_u \sqrt{2\pi}} \exp \left[ - \left( \frac{U - \bar{U}}{\sigma_u \sqrt{2}} \right)^2 \right], \quad (4.16)$$

the chance of exceeding  $U_{\text{max}}$  equals (Abramowitz and Stegun, 1965)

$$P(U > U_{\text{max}}) = \frac{1}{2} \left[ \frac{2}{\sqrt{\pi}} \int_{\frac{u_x}{\sqrt{2}}}^{\infty} e^{-t^2} dt \right] = \frac{1}{2} \left( \text{erfc} \frac{\langle u_x \rangle}{\sqrt{2}} \right), \quad (4.17)$$

where erfc is the complementary error function. We are looking for the number of samples  $N$  so that  $P(U > \langle U \rangle) = 1/2N$ . So

$$N(\langle U \rangle) = [2P(U > \langle U \rangle)]^{-1} = \left[ \text{erfc} \frac{\langle u_x \rangle}{\sqrt{2}} \right]^{-1}. \quad (4.18)$$

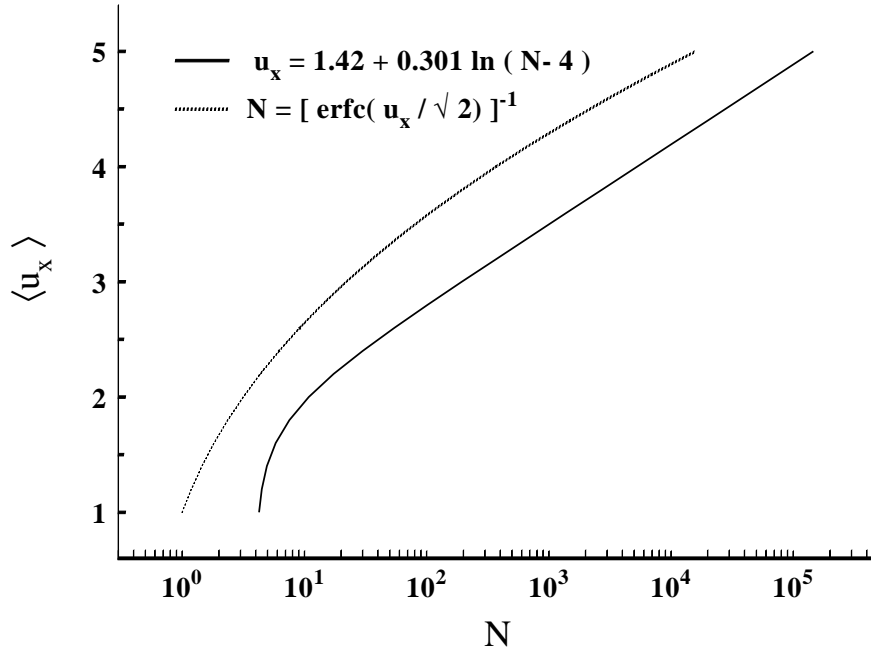


Figure 4.2:  $u_x$  with chance of exceedance  $1/2N$  as function of  $N$ .

This expression must be compared with Wieringa’s (1973) expression (Eq. 4.10). In Figure 4.2 both functions are plotted. For a given  $N$  Eq. 4.10 yields lower estimates of  $\langle u_x \rangle$  than Eq. 4.18. Proceeding in Wieringa’s derivation of Eq. 4.12 this difference becomes unimportant, however, because Wieringa “tunes” the factor  $990/\overline{U}t_{\text{gust}}$  to yield the correct  $z_0$  for his data set.

To derive a gust length Wieringa applies the attenuation function  $A$  to his gust model. This is done using a single time or length scale. Wieringa describes the gust length as the length scale at which the measured gusts are strongest. In fact,  $A$  is a spectral transfer functions and gusts are the result of the superposition of fluctuations with a variety of length scales. Moreover, gusts occur in the time domain whereas  $A$  is defined in the spectral domain. As we will see later, the gust length is a cut-off scale. Gusts smaller than this scale will have less influence on  $G$  because of the attenuation by the measuring chain.

## 4.5 Beljaars’s gustiness analysis

### 4.5.1 The gustiness model

Beljaars’s (1987a) starting point is the assumption that  $U(t)$  and  $\partial U/\partial t$  are joint Gaussian. In that case the probability of  $u_x$  being less than some arbitrary level  $U_s$  in period  $T$  is

$$P(u_x < U_s, T) = \exp[-E(U_s, T)], \quad (4.19)$$

$$E(U_s, T) = \nu T e^{-U_s^2/2}. \quad (4.20)$$

Here  $E$  is the expected number of up crossings of level  $U_s$ ,  $\nu$  is a frequency, the zero-crossing rate of  $U - \bar{U}$ , corresponding to the width of the power spectrum of horizontal wind speed variance,

$$\nu^2 = \frac{\int_0^\infty n^2 S_u(n) dn}{\int_0^\infty S_u(n) dn}. \quad (4.21)$$

$S_u$  is the spectral density at frequency  $n$ . For large  $\nu T$  the *average*  $\bar{u}_x$  equals

$$\bar{u}_x = (2 \ln \nu T)^{1/2} + \gamma (2 \ln \nu T)^{-1/2}, \quad (4.22)$$

where  $\gamma = 0.5772$  (Euler's constant). The first term on the right hand side of Eq. 4.22 is the mode of  $u_x$ .

Spectra, necessary for the evaluation of  $\nu$ , can be taken from literature. Beljaars used spectra from Kaimal (1977, data from the Minnesota site). These spectra explicitly include the influence of the boundary layer height  $z_i$  on the low frequency part of the spectrum. The high frequency portion scales on surface layer parameters only, and there is a transition zone:

$$\begin{aligned} \frac{n S_u(n)}{u_*^2} = & \begin{cases} \left(1 + 0.75 \left|\frac{z}{L}\right|^{2/3}\right) 0.3 f^{-2/3} & f \geq \frac{1}{2}, \\ \left(1 + 0.75 \left|\frac{z}{L}\right|^{2/3}\right) 0.48 (2f)^{-p} & \frac{1}{2} \geq f \geq \frac{3z}{2z_i}, \\ \left(12 + 0.5 \left|\frac{z_i}{L}\right|\right)^{2/3} \frac{f_i}{1 + 3.1 f_i^{5/3}} & f \leq \frac{3z}{2z_i}. \end{cases} \end{aligned} \quad (4.23)$$

Here the dimensionless frequencies  $f$  and  $f_i$  are given by  $nz/\bar{U}$  and  $nz_i/\bar{U}$ , respectively.  $L$  is the Monin-Obukhov length:

$$L = -\frac{u_*^3 \theta}{\kappa g w' \theta'}, \quad (4.24)$$

where  $g$  is the acceleration of gravity ( $9.8 \text{ m s}^{-2}$ ),  $\theta$  is the potential temperature, and  $\overline{w'\theta'}$  is the kinematic heat flux. For the transition zone  $p$  is given by

$$p = \ln \left( 0.44 \frac{(12 + 0.5 |z_i/L|)^{2/3}}{1 + 0.75 |z/L|^{2/3}} \right) / \ln \left( \frac{z_i}{3z} \right).$$

The transfer function of the anemometer ( $\tau = \lambda/\bar{U}$ ) or recorder ( $\tau = t_{\text{rec}}$ ) for  $\sigma_u^2$  as function of frequency is a regular first order transfer function, and can be written as

$$T_1(n) = [1 + (2\pi n \tau)^2]^{-1}. \quad (4.25)$$

The transfer function of an analogue running-average filter over  $t_0$  seconds is

$$T_{\text{ra}}(n) = \left( \frac{\sin \pi n t_0}{\pi n t_0} \right)^2, \quad (4.26)$$

and for a discrete running-average

$$= \left( \frac{\sin \pi n \Delta N}{N \sin \pi n \Delta} \right)^2. \quad (4.27)$$

Here averaging is done over  $N$  samples taken at  $\Delta$  seconds intervals ( $\Delta N$  is the averaging period).

When the wind speed signal is discretely sampled, the maximum will generally be missed, so  $\overline{u_x}$  will be smaller than with continuous recording. Beljaars derived a modified expression for Eq. 4.20 by considering the expected number of up crossings of a linearly interpolated signal between successive samples:

$$E(U_s, T) = \frac{T}{\Delta} P(u_x(t) < U_s, u_x(t + \Delta) > U_s), \quad (4.28)$$

from which he derived

$$E(U_s, T) = \frac{T}{\Delta} \frac{1}{\pi} \int_0^a \frac{\exp[-\frac{1}{2}U_s^2(1+y^2)]}{1+y^2} dy, \quad (4.29)$$

where

$$a = \left( \frac{1-\rho}{1+\rho} \right)^{\frac{1}{2}}, \text{ and } \rho = \frac{R(\Delta)}{R(0)}. \quad (4.30)$$

Here  $R$  is the autocovariance of the wind speed signal and can be computed from the turbulence spectrum. A new expression for  $\overline{u_x}$  can now be derived:

$$\overline{u_x} = \left( 2 \ln \frac{Ta}{\Delta\pi} \right)^{1/2} \left( 1 - \frac{1}{6}a^2 \right) + \gamma \left( 2 \ln \frac{Ta}{\Delta\pi} \right)^{-1/2}. \quad (4.31)$$

For small  $\Delta$

$$\lim_{\Delta \rightarrow 0} \frac{a}{\Delta\pi} = \nu, \quad \lim_{\Delta \rightarrow 0} a = 0, \quad (4.32)$$

and Eq. 4.31 reduces to Eq. 4.22.

## 4.5.2 Comments on Beljaars's model

There are two major differences between Wieringa's and Beljaars's model: the first concerns the influence of the measuring period  $T$ , and the second concerns the attenuation factor  $A$ .

The influence of  $T$  on  $u_x$  enters Beljaars's model via Eqs. 4.22 and 4.31. It also influences the apparent value of  $c$ ,  $\sigma_u$  is high-pass filtered with time constant  $T$  as an additional attenuation to  $A$ . In Wieringa's model the influence of  $T$  on the measured gustiness enters the equations by the factor  $f_T$  in Eq. 4.12. As we will see in the next section this difference hampers the direct comparison of the  $u_x$ -values from both models.

To stress the conceptual difference between Beljaars's and Wieringa's model concerning the transfer function  $A$ , in Figure 4.3 a flow chart is plotted. Wieringa's method starts with a statistical criterion and uses gustiness data to find  $u_x(\overline{U}t_{\text{gust}})$ , then he applies the recorder and anemometer transfer functions to find  $\overline{U}t_{\text{gust}}$  and hence the expected  $\langle u_x \rangle$ .

Beljaars's method starts with spectra. All transfer functions have to be applied to the turbulence spectrum. These modified spectra enter the gust model which yields the expected average  $\overline{u_x}$  (Greenway, 1979, cf. figure 2). The anemometer and recorder transfer will influence  $\nu$  via Eq. 4.21, and  $\overline{u_x}$  via Eq. 4.22. This also applies to the running-average filter.

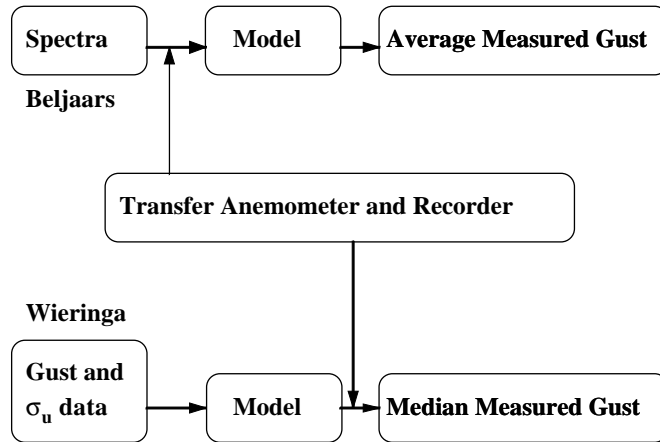


Figure 4.3: Flow chart showing the different concepts of Wieringa and Beljaars.

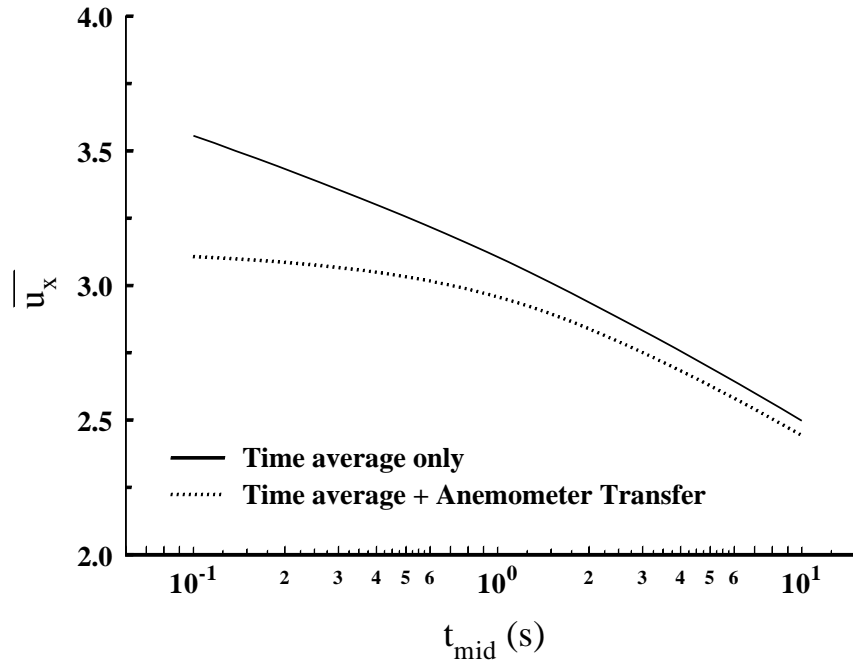


Figure 4.4: Averaged normalized gust magnitude  $\bar{u}_x$  as function of averaging time of running-average filter with and without application of the anemometer transfer function.

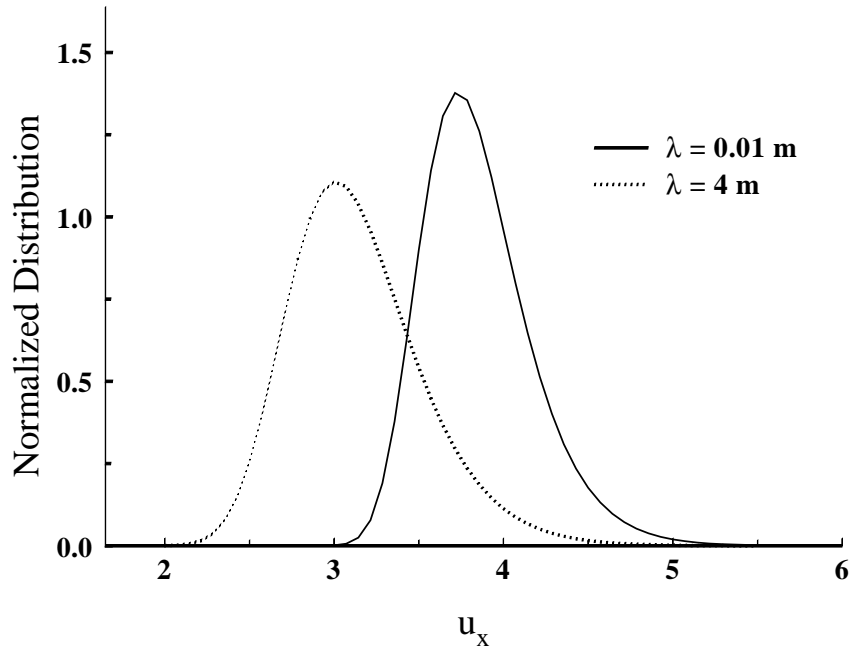


Figure 4.5: Normalized distribution of  $u_x$  for two measuring chains, the first with an anemometer response length of 0.01 m, the second the a response length of 4 m. For both a recorder response time of 0.001 s was used.

The effect of the anemometer inertia on  $u_x$  according to Beljaars's model is illustrated in Figure 4.4. Here  $\overline{u_x}$  is plotted as function of the averaging time of the running-average filter with and without application of the anemometer transfer function ( $U = 8 \text{ m s}^{-1}$ ,  $\lambda = 4 \text{ m}$ ). Both the running-average over time and the anemometer will attenuate high frequencies in the turbulence signal, and this will reduce the expected  $\overline{u_x}$ . Shorter averaging times will yield a larger  $\overline{u_x}$ , also when this averaging time is smaller than the anemometer response time ( $4 \text{ m}/8 \text{ m s}^{-1} = 0.5 \text{ s}$ ). This figure shows that fluctuations of all scales, even the smallest, will contribute to  $\overline{u_x}$ . So the peak gust in a record cannot be associated with a single gust length. However, the main contribution to the variance in the recorded signal will come from fluctuations with length scales comparable with the length scale of the measuring chain. So the gust duration of a measuring chain is the cut-off time below which the gusts are strongly attenuated. Beljaars (1987a; 1988) defines the gust duration as follows:

Gusts observed after a running-average filter have a duration that is equal to the averaging time of the filter. An arbitrary measuring chain with several elements (not necessarily running-average filters) produces gusts with duration  $t_0$ , if a hypothetical running-average filter with averaging time  $t_0$  would have resulted in the same gust magnitude.

The effect of anemometer inertia on the observed gusts distribution is illustrated in Figure 4.5. Here the normalized distribution of  $u_x$  is plotted (Eq. 4.19) for two measuring chains. Filtered gusts have smaller  $u_x$ . The shift in the average of  $u_x$  corresponds to the difference between the curves in Figure 4.4.

## 4.6 Application of gustiness models

In this section the gustiness models will be used for roughness length estimation, this  $z_0$  is used to compute the exposure correction. Beljaars's model was not designed for  $z_0$ -estimation. The application is straightforward and similar to that of Wieringa's model, however. Maximum gust records and information on the measuring chain is the required input information, just as in Wieringa's model.

In the context of Beljaars's model, the factor  $A$  reduces the apparent value of  $\sigma_u/\bar{U}$ , the second term in Eq. 4.9. Then from rearranging Eq. 4.9 we can derive

$$\ln \frac{z}{z_0} = \frac{Ac\kappa u_x}{G-1}, \quad (4.33)$$

which yields the roughness length. The attenuation  $A$  can be computed from

$$A^2 = \frac{\int_0^\infty T_{hp}(n)T_1(n)T_{ra}(n)S_u(n)dn}{\int_0^\infty S_u(n)dn}, \quad (4.34)$$

where  $T_{hp}$  is the high-pass filter associated with the measuring period  $T$ :

$$T_{hp}(n) = 1 - [1 + (2\pi nT)^2]^{-1} \quad (4.35)$$

In the context of Wieringa's model combination of Eq. 4.12 and Eq. 4.14 leads to

$$\ln \frac{z}{z_0} = \frac{f_T Ac\kappa u_x}{G-1-A(f_T-1)}. \quad (4.36)$$

Now  $A$  is given by Eq 4.13. The additional term in the denominator is the result of the time function  $f_T$  operating on the total right hand side of Eq. 4.12, in stead of working on the turbulent fluctuations alone like the attenuation  $A$  does. The peculiar result is an interaction between  $A$  and  $f_T$ : the value of  $f_T$  determines to what extent  $A$  influences the measured gustiness. In case of  $T = 3600$  s,  $f_T = 1.1$ . With  $A \approx 0.9$  and  $G-1 \approx 0.5$ , it is clear that the term  $A(f_T-1)$  has a major influence on the roughness length estimate.

For both models knowledge of the average wind speed is necessary. So when  $G$  is determined, a selection on a certain wind speed range should be applied. The wind speeds selected should not be too low, to ensure nearly neutral conditions. For the Netherlands, with only weak or moderate insolation, a minimum wind speed of  $5 \text{ m s}^{-1}$  is usually enough. De Bruin et al. (1993) computed  $z_0$  from measurements of  $\sigma_u$  and  $U$  using Eq. 4.8 for a site in southern France. Their figure 10 shows that even in cases of strong insolation a wind speed of  $7 \text{ m s}^{-1}$  is enough to let  $z_0$  converge to a single value. Note that for Wieringa's model the median, and for Beljaars's model the average of  $G$  and  $u_x$  should be taken. The difference is usually insignificant for the exposure correction estimates, however. An advantage of using the median is it's stability in non-stationary situations.

The evaluation of the models is done in four ways. First, for three measuring chains the relation between  $G$ ,  $z_0$ , and  $S$  is investigated. The measuring chains are examples from routine observations that have been used at different KNMI stations in the past. Second, the effect of the measuring period  $T$  is investigated by analyzing a data set from Schiphol (Amsterdam airport). Third, a record from Zestienhoven (Rotterdam airport) is used to evaluate the models's capacity to deal with changes in the measuring chain. Fourth, the roughness lengths found with Beljaars's model are used to estimate the wind speed at 40 and 80 m height, the region of the assumed blending height, from the wind speed at 10 m height at the Cabauw tower (Van Ulden and Wieringa, 1996). The estimates are then compared with the observed wind speed at these height.

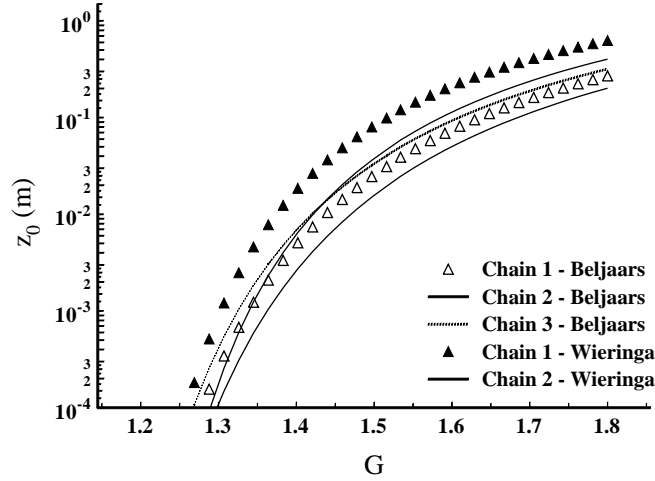


Figure 4.6: Roughness length as function of  $G$  calculated using Beljaars's and Wieringa's model for the three measuring chains of section 4.6.1 with  $T = 3600$  s.

Table 4.1: Input parameters for three measuring chains.

Chain	$\lambda$ (m)	Recording	Recorder parameters
1.	2.9	Continuous	$t_{\text{rec}} = 0.8$ s
2.	2.9	Continuous	$t_{\text{rec}} = 0.2$ s
3.	2.9	Discrete	$\Delta = 0.25$ s, $N = 12$

Table 4.2: Input parameters for spectra and exposure correction computation.

$z_m$	$z_b$	$z_i$	$L$	$T$	$U$
10 m	60 m	1000 m	$-10^5$ m	3600 s	8.2 m s <sup>-1</sup>

Table 4.3: Measuring chain parameters and gustiness analysis of station Zestienhoven before and after the recorder exchange in 1988.

	Before 1988		After 1988	
	Beljaars	Wieringa	Beljaars	Wieringa
$t_{\text{rec}}$ (s)	0.8	0.8	0.2	0.2
$A$	0.90	0.88	0.93	0.92
$G$	1.43	1.40	1.55	1.52
$u_x$	3.48	2.00	3.64	2.25
$z_0$ (m)	0.016	0.022	0.045	0.053
$S$	0.98	0.99	1.02	1.03

### 4.6.1 Evaluation of three measuring chains

In this section the two gustiness models are evaluated for three measuring chains. In all cases a cup anemometer (KNMI 018,  $\lambda = 2.9$  m) is used, first in combination with a Nieaf recorder, second with a Camille Bauer recorder, and third with the AWS-configuration. The parameters of these measuring chains can be found in Table 4.1. Since the latter measuring chain samples at discrete time intervals, it will only be evaluated with Beljaars's model. In Table 4.2 the necessary parameters of the atmospheric boundary layer are given. When calculating  $z_0$  with Beljaars's model we use  $c = \sigma_u/u_* = 2.2$ , and with Wieringa's model  $c = 2.5$ , since these are the values used by the authors themselves.

Wieringa's roughness lengths are larger than those resulting from Beljaars's model (see Figure 4.6). The resulting exposure correction factors are plotted in Figure 4.7(a). Over smooth terrain, when the exposure correction is less than 1, Wieringa's correction is about 1% larger than (chain 1), or is equal to Beljaars's correction (chain 2). Over rough terrain Wieringa's correction is larger by about 12% (chain 1) or 7% (chain 2).

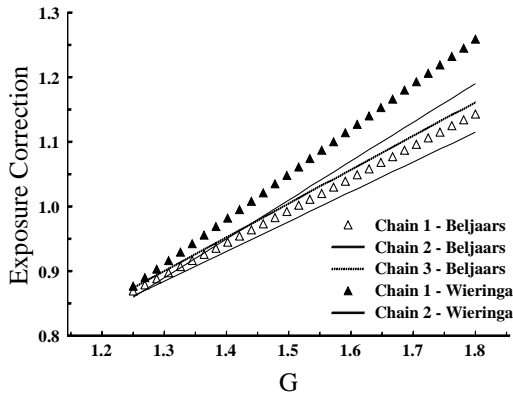
To illustrate the effect of the term  $A(f_T - 1)$  in the denominator of Eq. 4.36, Figure 4.7(a) is re-computed and plotted in Figure 4.7(b) for the same measuring chains with the only difference that  $T = 600$  s instead of  $T = 3600$  s. So  $f_T = 1$  and the  $A(f_T - 1)$  in the denominator of Eq. 4.36 vanishes. A different gustiness interval has been chosen so that the same range of exposure corrections factors (and roughness lengths) is obtained. Again Wieringa's exposure correction is larger, 3% or 2% for smooth surfaces to 12% or 9% for rough surfaces for chain 1 and 2, respective.

So with  $z_0 = 0.1$  m Wieringa's correction is about 6% larger. However, since  $\langle G \rangle$  is a few percent smaller than  $\overline{G}$ , this difference is reduced to 4–5%.

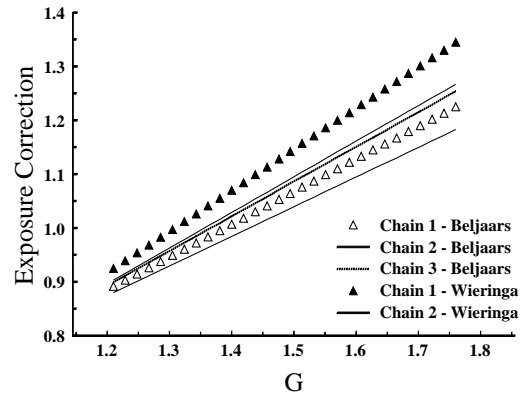
### 4.6.2 Schiphol data set

In the previous section it was shown that the difference between Beljaars's and Wieringa's exposure corrections is a function of the measuring time  $T$ . In this section the influence of  $T$  will be investigated further. This will be done using a data set collected at Schiphol airport. The data were collected on four masts of 10 m height by analogue recorders (Heath,  $t_{\text{rec}} = 0.07$  s) and cup-anemometers (KNMI 018). In the period from 1978 to 1983 1-min averages and gusts were collected. From these 1-min records, averages and gusts were composed for 10-, 30-, and 60-min periods. For these values of  $T$  both gustiness models were used to compute the exposure corrections.  $G$  will increase with increasing  $T$ . If the gustiness models express  $u_x$  as function of  $T$  correctly,  $S$  will be the same for different values of  $T$ .

Results for one mast (# 27) are plotted in Figure 4.8(a) and 4.8(b). Beljaars's exposure corrections are larger for larger  $T$ . So  $G$  increases stronger with  $T$  than would be expected from Beljaars's model. The difference between  $T = 600$  s and  $T = 3600$  s is usually smaller than 5%. Wieringa's model gives higher exposure corrections for  $T = 1800$  s than for  $T = 3600$  s and  $T = 600$  s. On average the difference between the curves is smaller than for Beljaars's model. The difference is a function of  $G$ , however. For large  $T$ ,  $S$  is more sensitive to  $G$  than for small  $T$ . This is the result of the term  $A(f_T - 1)$  in the denominator of Eq. 4.36. The larger  $T$  and  $f_T$ , the smaller the denominator becomes, and so Eq. 4.36 becomes more sensitive to changes in  $G$ .

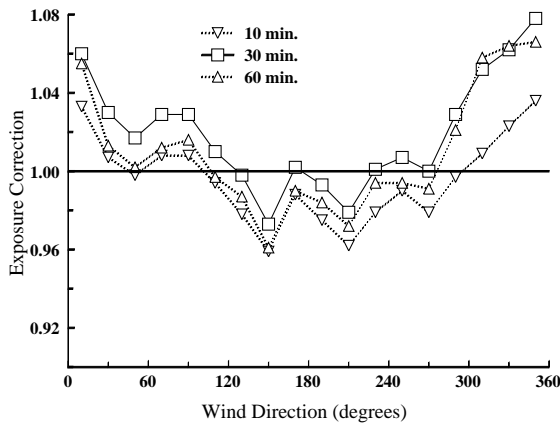


(a)  $T = 3600$  s.

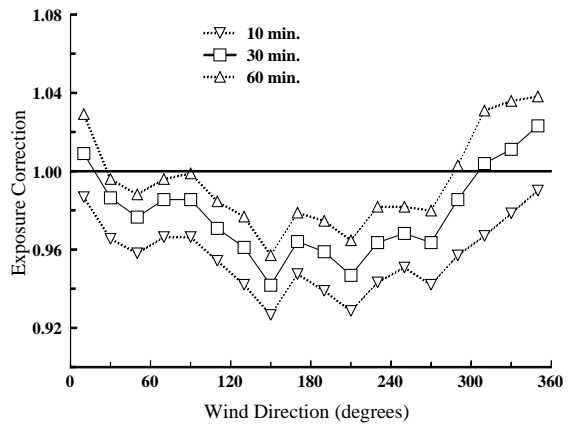


(b)  $T = 600$  s.

Figure 4.7: Exposure correction factor  $S$  as function of  $G$  calculated using Beljaars's and Wieringa's model for the three measuring chains of section 4.6.1 with different values for  $T = 3600$  s and  $T = 600$  s.



(a) Wieringa.



(b) Beljaars.

Figure 4.8: Exposure correction factor  $S$  for different values of  $T$  (600 s, 1800 s, 3600 s) calculated with Wieringa's and Beljaars's model for mast 27 of the Schiphol data set.

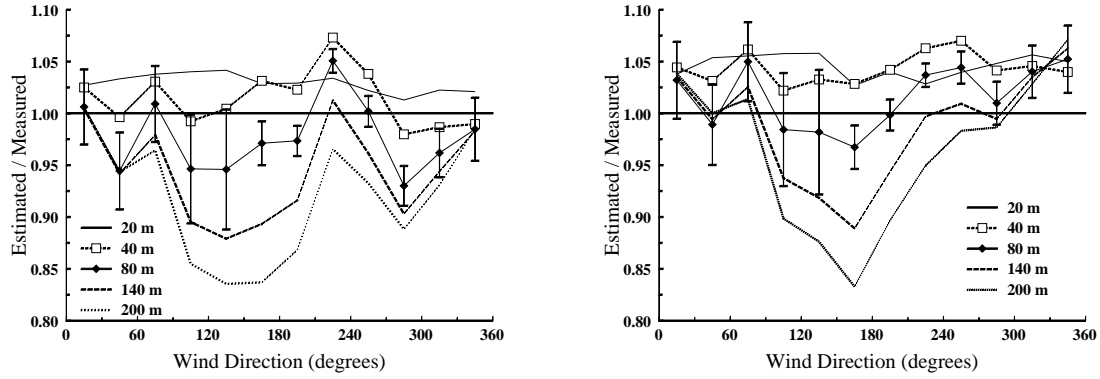
### 4.6.3 Recorder exchange at Zestienhoven

At Zestienhoven airport during 1988 a slow recorder (Nieaf,  $t_{\text{rec}} = 0.8$  s) was replaced by the faster Camille Bauer ( $t_{\text{rec}} = 0.2$  s). This resulted in an increase in  $G$ : for wind speeds larger than  $7 \text{ m s}^{-1}$  and from the directions between  $270^\circ$  and  $300^\circ$   $G$  increased from  $1.43 \pm 0.02$  before 1988, to  $1.55 \pm 0.02$  after 1988. The median was about 3% smaller than the average of  $G$  probably due to nonstationarity which increases the average more than the median of  $G$ . Assuming that there were no significant changes in the station's surrounding, the roughness lengths found from the gustiness analysis ought to be the same before and after the recorder exchange.

The average wind speed, measured at 10 m height, in this data selection is  $9.3 \text{ m s}^{-1}$ . The response length of the cup-anemometer is 2.9 m. From this information,  $u_x$  can be computed for the measuring chains before and after the recorder exchange. The results are summarized in Table 4.3. It is clear that besides the small difference in roughness length between the two models, for both models a jump in  $z_0$ , and hence in  $S$ , remains. An increase of 4% in  $S$  results from straightforward application of the models. The selected sector is covered mainly by short grass close to the tower. In the distance ( $\approx 0.8$  km), however, there are some bushes and low trees. From a roughness literature review (Wieringa, 1993) we expect to find a roughness length of 0.02–0.06 m. The computed roughness lengths are in the expected range.

Although a 4% uncertainty in exposure correction will be acceptable for most applications, we can still wonder why the models do not neutralize the recorder exchange effect completely. The following causes are suggested. First of all, the models can be wrong. Second, the effect of the recorder exchange on  $S$  may be contaminated with changing surface roughness in the environment of Zestienhoven. Third, the measuring chain information, and therefore  $u_x$ , is incorrect.

Wieringa (1980a) already validated and applied his model using different data sets successfully. Beljaars (1987a) also validated the sensitivity of his model to changes of measuring chains. So the first cause is not very plausible. Environmental changes can not be ruled out completely, but it is unlikely that a sudden change in roughness has occurred in one year ( $G$  increased for all wind directions). The recorder response times are only poorly documented, so these must be suspected at first. Wieringa and Van der Veer (1976) note that there is a large uncertainty in the response time of the Nieaf recorder and it may also change in time, depending on its maintenance. Applying Beljaars's model, the Nieaf recorder should have a response time about 3.6 s to level out the roughness jump. For Wieringa's model its response time should be about 1.4 s. The difference between these response times indicates that the sensitivity of the models for the measuring chain is different. More accurate information on the measuring chain is required to judge which model performs best, however. Unfortunately none of the old recorders was kept at KNMI, so checks on the response time are no longer possible. Wieringa and Van der Veer (1976) report attenuation of the gust factor during the transmission from anemometer to recorder of 18% for some stations in the Netherlands. In case that with the replacement of the recorder at Zestienhoven also the signal transmission has been improved, this may explain the jump in measured  $G$ .



(a)  $z_0$  from gustiness analysis of the sonic at 5.4 m.

(b)  $z_0$  from gustiness analysis of the propeller vane at 10 m.

Figure 4.9: Ratios of estimated to measured wind speed for different heights as function of wind direction. The wind speed profile is estimated from the wind speed measured by the propeller vane at 10 m height. The roughness length is found from gustiness analysis of a sonic at 5.4 m height (upper panel) and from the propeller vane at 10 m height (lower panel).

#### 4.6.4 Estimation of wind speed at elevated levels

Gustiness analysis is applied to find a roughness length that enables us to extrapolate the wind speed from the surface to the blending height. The model's performance can directly be tested when wind speed observations at different levels are available. Therefore, we turn to the Cabauw tower.

From the Cabauw tower two wind speed records are used. The first is measured at 10 m height by a propeller vane with  $\lambda = 2.2$  m (Monna and Driedonks, 1979), and a recorder with  $t_{\text{rec}} = 1$  s, discretely sampled every 3 s. Data were stored every 30 min. A six-year period is analyzed. Wind speeds in the range  $7\text{--}10$  m s $^{-1}$  at 10 m were selected for the gustiness analysis and for the extrapolation of the wind speed. The second record is measured at 5.4 m height, by a sonic anemometer with path length 0.1 m, sampled at 10 Hz. Data were stored every 10 min. Here, a 7-month period is analyzed. Wind speeds in the range  $8\text{--}12$  m s $^{-1}$  at 5.4 m were selected for gustiness analysis using Beljaars's model. The resulting roughness lengths were used to extrapolate the 10-m wind from the former data set. No analogue wind speed records are available to the author at present, so the same comparison can not be done using Wieringa's model. However, Holtslag (1984) estimated wind speed profiles up to 200 m height at Cabauw using surface observations only. He obtained good results using roughness lengths derived with Wieringa's gust model and surface observations to estimate atmospheric stability.

In Figure 4.9 the ratio of estimated to measured wind speed at different heights are plotted as function of wind direction. The gustiness analysis is applied to the wind speed records of sonic anemometer in Figure 4.9(a) and to the propeller vane in Figure 4.9(b). For the 80-m level errors bars are plotted which denote the uncertainty in the  $U_{\text{est.}}/U_{\text{meas.}}$ -ratio. For clarity the error bars for the other heights are omitted but they are of the same magnitude. With the blending height assumed at a height of about 60 m, the relevant heights are the 40-m and 80-m level. For both heights the estimated wind speed is within 5% of the measured wind speed, which is satisfactory. The south-east sectors, where at

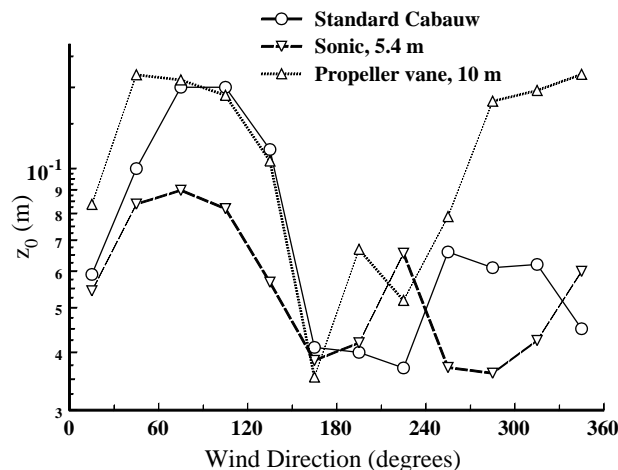


Figure 4.10: Roughness lengths as a function of wind direction at the Cabauw site. The standard Cabauw values are derived from the analysis of the standard deviation of the wind speed, the other values are derived from gustiness analysis of the sonic anemometer at 5.4 m, and the propeller vane at 10 m height.

higher levels the largest deviations are found, is the most complex region at Cabauw.

In Figure 4.9 there is a clear trend with height, the wind speed at 20 and 40 m are overestimated while at the higher levels there is a growing underestimation. Estimates based on the analysis of the 5.4-m high sensor are generally lower those that based on the 10-m high sensor. This is the result of the different footprints for the two heights (Schmid and Oke, 1990). Close to the tower the surface is very smooth compared with the surface further away. The lowest sensor will be influenced most by the surface close to the tower and the estimated roughness length will be lower. Underestimation of regional  $z_0$  will result in underestimation of  $U$  at higher levels. Since the wind speed at 10 m height is relatively high because of the small local surface roughness, the wind speed at 20 and 40 m height will be overestimated but at higher levels the wind speed will be underestimated. Similar effects can also be found in the estimates of Holtslag (1984). He took into account stability effects which resulted in better wind speed estimates at higher levels. In the exposure correction procedure as applied in this paper stability effects are not taken into account since information on stability is often not available. So there is no sense in a detailed comparison of our results with those of Holtslag (1984).

In Figure 4.10 the roughness lengths are plotted as a function of wind direction. The standard Cabauw values are derived from the analysis of the standard deviation of the wind speed (Beljaars, 1988), the other values are derived from gustiness analysis of the sonic anemometer at 5.4 m, and the propeller vane at 10 m height. In the east sector tree lines and a built-up area commence suddenly at about 0.3 km from the tower (see figure 1 of Van Ulden and Wieringa, 1996). This is reflected by the high roughness lengths, although the sonic at 5.4 m seems to be influenced by the smooth local surface. The south-west sector is the most uniform and smooth sector on which all estimates agree. Going from west to north a shelterbelt-like a line of low farms and trees is approaching the tower with a minimum distance of  $\approx 0.5$  km in the north-west direction. Further away the surface is very smooth again. In this sector the roughness estimates do not agree at

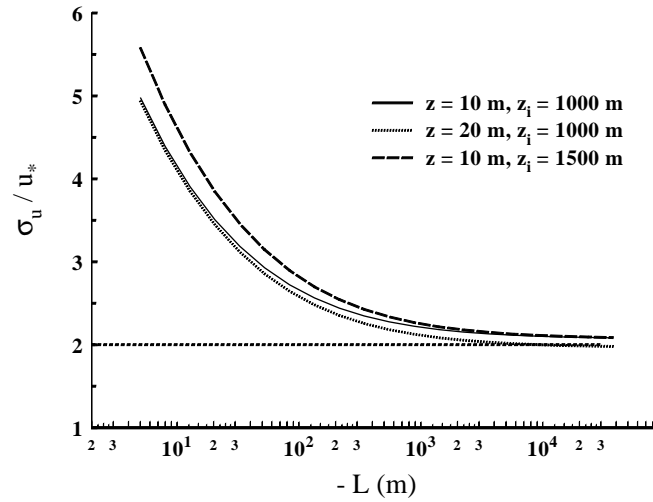


Figure 4.11: Standard deviation of horizontal wind speed as function of Obukhov length for different boundary layer depths and different heights as modeled by Højstrup (1982).

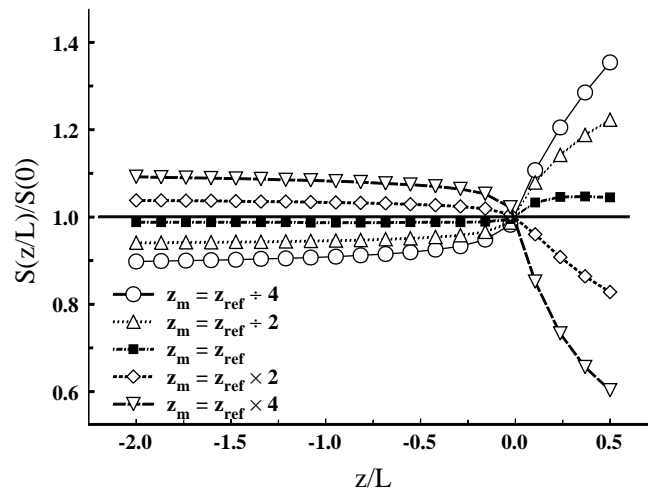


Figure 4.12: Effect of stability on the exposure corrections from  $z_0 = 0.1$  m to  $z_0 = 0.03$  m. The ratio of non-neutral to neutral exposure correction is plotted as function of stability for different ratios of measuring height to reference height.

all. The sonic at 5.4 m gives the lowest roughness lengths. It is important to notice that these measurements are done 0.1–0.2 km south of the main tower. At 5.4 m height the boundary layer will be close to full equilibrium with the smooth surface in the vicinity of the tower (Garratt, 1990). The approaching line of roughness elements is reflected by the increasing roughness lengths from the gustiness analysis of the propeller vane at 10 m height. In the standard Cabauw  $z_0$ -values, *i.e.* analysis of  $\sigma_u/u_*$  at 10 m height, there is hardly any increase. This is probably due to different footprints for the extremes and the standard deviation of the wind speed signal. The standard deviation has large contributions of fluctuations with very low frequencies or large length scales. Gusts are dominated by fluctuations with higher frequency or shorter time scales. Because of the slower adaptation time of the low-frequency fluctuations,  $\sigma_u$  is determined by the smooth surface far upstream in the north (Højstrup, 1981). So analysis of  $\sigma_u/u_*$  results in lower  $z_0$ -values than the gustiness analysis. Ultimately this means that the turbulent wind speed distribution can not be Gaussian in terrain which is strongly heterogeneous at horizontal scales of the order of 1 km.

From the estimated wind speeds in Figure 4.9 in the north-west direction it can be seen that  $z_0$  is scale dependent. For the purpose of exposure correction this implies that one should use roughness values derived from gustiness data observed at the same height as the corrected average wind, since then at least the footprint is similar. The difference between the two values observed at 10 m, the  $(\sigma_u/u_*)$ -derived “standard” and the propeller vane observations, requires close examination. More details of Figure 4.9 can be explained by close examination of the internal boundary layer structure at Cabauw, but we will not go further into this in this paper.

## 4.7 Influence of atmospheric stability and blending height

In the previous section we found a difference in exposure correction between Beljaars’s and Wieringa’s model of 0–10% for gustiness analysis with  $T = 3600$  s, and a difference of 2–11% for  $T = 600$  s. We found a 5% spread in  $S$  as a function of  $T$ . For the case-study Zestienhoven we found a jump in exposure correction of 4% as the result of a recorder exchange, and from the Cabauw data we found that the wind speed at 40–80 m can be estimated from the gustiness and wind speed close to the surface within 5%. To put these uncertainties in exposure correction in perspective, we also consider the uncertainties resulting from atmospheric stability and the blending height estimate.

### 4.7.1 Influence of stability on $\sigma_u/u_*$

For the neutral surface layer, the standard deviation of horizontal wind speed fluctuations ( $\sigma_u$ ) is related to the friction velocity ( $u_*$ ). Different ratios for  $\sigma_u/u_*$  are reported: Beljaars used 2.2 (Panofsky et al., 1977; Beljaars and Holtslag, 1991); Wieringa used 2.5 which he derived from his data over Lake Flevo ( $\sigma_u/u_* = 2.47 \pm 0.52$ ). This corresponds also to values given by Lumley and Panofsky (1964). It is doubtful whether  $\sigma_u$  follows M–O theory since it is not solely determined by surface fluxes but also by eddies with the size of the atmospheric boundary layer. So  $\sigma_u/u_*$  will be a function of both  $z/L$  and  $z_i/L$  (Panofsky and Dutton, 1984; De Bruin et al., 1993). Højstrup (1982) integrated expressions for atmospheric turbulence spectra to find a relation for  $\sigma_u/u_*$  as function of stability and

boundary layer height (see Figure 4.11):

$$\left(\frac{\sigma_u}{u_*}\right)^2 = 0.6 \left(\frac{z_i}{-L}\right)^{\frac{2}{3}} + 4.8 \frac{(1 - z/z_i)^2}{1 + 15z/z_i}. \quad (4.37)$$

The boundary layer height  $z_i$  has only small influence on  $\sigma_u/u_*$ . From Figure 4.11 it can be seen that  $\sigma_u/u_*$  at 10 m height increases from its neutral value of 2.2 to about 4 for  $L = -100$  m. Stability parameters are usually not available and one often assumes a constant (neutral) value for  $\sigma_u/u_*$ . To determine the impact of possible errors in the estimate of  $\sigma_u/u_*$  on  $S$  the partial derivative of  $S$  to  $\sigma_u/u_*$  is taken. The sensitivity of the  $z_0$ - and  $S$ -estimate for the choice of  $\sigma_u/u_*$  can be expressed as follows

$$\frac{\sigma_u}{u_*} = c \left(\frac{z}{L}, \frac{z_i}{L}\right),$$

$$\frac{dz_0}{z_0} = \frac{dc}{c} \frac{\partial z_0}{\partial c} = -\frac{dc}{c} \left(\ln \frac{z}{z_0}\right), \quad (4.38)$$

$$\frac{dS}{S} = \frac{dz_0}{S} \frac{\partial S}{\partial z_0} = \frac{dz_0}{z_0} \left(\frac{\ln z_b/z_m}{\ln z_b/z_0 \cdot \ln z_m/z_0}\right). \quad (4.39)$$

Here  $dz_0$  and  $dc$  represent the uncertainties in  $z_0$  and  $c$ , respectively. With  $z_b = 60$  m,  $z_m = 10$  m, and  $z_0 = 0.1$  m, the term in parenthesis in Eq. 4.38 equals 4.6, and that in Eq. 4.39 equals 0.06. With  $dc = 1$  and  $c = 3$ ,  $|dz_0/z_0| \simeq 1.5$ , and  $dS/S$  equals almost 0.1. For  $c = 2.5$ , and a  $dc$  of 0.3 ( $-L > 800$  m) the uncertainty in  $U_p$  is only 2%. So the effect of non-neutral stability on the value of  $c$  is of minor importance.

## 4.7.2 Influence of stability on the wind speed profile

The influence of atmospheric stability on the ratio  $\sigma_u/u_*$  is already discussed and turned out to be of minor importance. Stability effects, however, will also influence the wind speed profile. In non-neutral, steady-state, and homogeneous conditions the wind speed gradient is a function of atmospheric stability only (Blackader and Tennekes, 1968; Businger and Yaglom, 1971; Obukhov, 1971):

$$\frac{\kappa z}{u_*} \frac{\partial U}{\partial z} = \Phi_M \left(\frac{z}{L}\right). \quad (4.40)$$

Here  $\Phi_M$  is the non-dimensional wind speed gradient (Dyer, 1974; Yaglom, 1977). Integrating this equation like in Paulson (1970) enables us to derive a non-neutral version of Eq. 4.5

$$S \left(\frac{z}{L}\right) = \left(\frac{\ln z_b/z_0 - \Psi_M(z_b/L) + \Psi_M(z_0/L)}{\ln z_m/z_0 - \Psi_M(z_m/L) + \Psi_M(z_0/L)}\right) \times \left(\frac{\ln z_{\text{ref}}/z_{0\text{ref}} - \Psi_M(z_{\text{ref}}/L) + \Psi_M(z_{0\text{ref}}/L)}{\ln z_b/z_{0\text{ref}} - \Psi_M(z_b/L) + \Psi_M(z_{0\text{ref}}/L)}\right). \quad (4.41)$$

In Figure 4.12 the ratio of non-neutral to neutral exposure correction,  $S(z/L)/S(0)$ , is plotted for  $z_0 = 0.1$  m. If  $z_{\text{ref}}$  is close to  $z_m$  the influence of stability is small. This is mainly due to the compensating effect of transforming the wind speed upwards to the blending height and downwards assuming the same (wrong) Obukhov length (Wieringa, 1986). In

unstable conditions the effect of stability on  $S$  will generally be less than 10%. In stable conditions  $S(z/L)/S(0)$  soon becomes large. With  $U > 5 \text{ m s}^{-1}$  at 10 m height,  $|z/L|$  will generally be well below 0.1, and the error in  $S$  well below 10%. For larger  $z_0$  the effect of stability is somewhat larger than for smaller roughness lengths.

### 4.7.3 Blending height

The blending height is a function of the horizontal scale of the major surface heterogeneity and of atmospheric stability (Mason, 1988; Claussen, 1990; Mahrt, 1996; Philip, 1997; Ma and Daggupati, 1998). For the Netherlands Wieringa (1986) used a uniform value of 60 m, corresponding to a heterogeneity length scale of a few hundred meters.

To estimate the sensitivity of  $S$  to the choice of  $z_b$ , the partial derivative of  $S$  to  $z_b$  was taken. The sensitivity of  $S$  can be expressed as follows:

$$\frac{dS}{S} = \left( \frac{\ln z_0/z_{0\text{ref}}}{\ln z_b/z_{0\text{ref}} \cdot \ln z_b/z_0} \right) \frac{dz_b}{z_b}. \quad (4.42)$$

When the local roughness is relatively small,  $z_0 = 0.1 \text{ m}$ ,  $z_{0\text{ref}} = 0.03 \text{ m}$ , and  $z_b = 60 \text{ m}$ , the expression in parenthesis equals 0.06. In this case also  $S$  itself will be close to unity, and the uncertainty in  $S$  is about 20 times smaller than that of  $z_b$ . However, if  $z_0 = 1 \text{ m}$ , the expression in parenthesis equals 0.25. So when the local surface roughness increases, the actual value of  $z_b$  becomes more important. Using a too low  $z_b$  over rough, heterogeneous areas, which seems the most likely thing to happen, will also make  $S$  too low.

## 4.8 Conclusions

Two gustiness models, from Wieringa (1976) and Beljaars (1987a), have been evaluated and tested on their capability of relating gustiness to surface roughness. Both gustiness models assume a Gaussian distribution of the turbulent wind speed fluctuations. The computation of the exposure correction is done assuming Monin-Obukhov similarity theory is valid. Although both assumptions are common in boundary layer research, certainly in cases of heterogeneous terrain when we need exposure corrections, their validity is questionable. A theoretical objection was found against Wieringa's gust model: Wieringa applies spectral transfer functions on gusts that occur in the time domain. This results in the erroneous notion of a "gust length with maximum gust factor" for a certain measuring chain. For a certain measuring chain there will be a length- or time-scale below which eddies are strongly attenuated. However, the peak gust during the observing period is always the result of the superposition of several eddies which are in phase and it cannot be associated with a single length- or time-scale.

For observation periods of one hour, Beljaars's model gives exposure corrections that are 0–10% smaller than those from Wieringa's model, depending on surface roughness. For shorter observation periods the difference is larger. For 10-min periods for example, Beljaars's exposure corrections are 3 to 10% smaller. In view of other uncertainties, the influence of atmospheric stability on the ratio  $\sigma_u/u_*$  and the wind speed profile, and the assumed blending height, the difference between the two gustiness models is small for observing periods of one hour.

Analyzing a data set with different values for the observing period  $T$  yields a 5% spread in exposure correction  $S$  for Beljaars's model.  $S$ , as calculated by the model, increases as

$T$  increases from 600 to 3600 s. Applying Wieringa's model there seems to be a maximum in  $S$  as function of  $T$ . The spread in  $S$  is on average smaller, but the sensitivity to the gust factor  $G$  increases with  $T$ .

Both models were tested at an airport station where a change in the measuring chain has occurred, the old wind speed recorder was replaced by a faster recorder. Both models are not quite capable of leveling the change in observed gustiness. In this example a jump in roughness length remains corresponding to a exposure correction change of 4%.

Roughness lengths from Beljaars's model have been used to extrapolate the wind speed profile from 10 m height to higher levels. These estimated profiles were compared with observations from the Cabauw tower. Gustiness analysis was applied to two different wind speed records to yield the roughness length. Beljaars's model performed satisfactorily: differences less than 5% were found when estimating the wind speed at 40 and 80 m height from the wind speed at 10 m height. Since no analogue wind speed records are available to the author at present, no similar analysis can be done for Wieringa's model, but Holtslag (1984) obtained good results using roughness lengths from Wieringa's gust model in combination with surface observations of atmospheric stability.

With both Wieringa's (1976) and Beljaars's (1987a) gustiness model the exposure correction can be computed with an accuracy of 5%. If this uncertainty would be due only to the uncertainty in the  $z_0$  estimate, the uncertainty in  $z_0$  can be found from solving Eq. 4.5 for  $z_0$ . It follows that the accuracy of the roughness length depends strongly on the magnitude of  $z_0$  itself. For  $z_0 = 0.03$  m it will be accurate to a factor 3–4, for  $z_0 = 0.2$  m to a factor 2, and with  $z_0 = 1$  m its accuracy will be about 15%.

## Acknowledgments

This paper is a partial and preliminary result of the contribution of the Royal Netherlands Meteorological Institute (KNMI) to the HYDRA-project, supported by the National Institute for Coastal and Marine Management (RIKZ) and the Institute for Inland Water Management and Waste Water Treatment (RIZA).

The author wishes to thank Fred Bosveld and Rinus Rauw from the Atmospheric Research Section of KNMI who helped computing the gust factors from the Cabauw data sets, Henk Benschop for making available the Schiphol data set, and several members from the Observations and Modeling Section of KNMI who also gave useful feedback. Dr. Anton Beljaars and Prof. Jon Wieringa gave helpful comments about their gust models. Prof. Wieringa also gave good advice at various stages writing this paper.



# Chapter 5

## Local Wind Speed Estimation by Physical Downscaling of Weather model forecasts.

Submitted to *Journal of Wind Engineering and Industrial Aerodynamics*, 2005.

Co-authors: A. J. M. Jacobs, A. B. C. Tijm and J. R. A. Onvlee

### Abstract

Wind speed forecasts by numerical weather prediction (NWP) models in heterogeneous terrain lack local representativity as they are derived using grid-box averaged roughness lengths. In this paper a downscaling method is presented to increase the local accuracy of NWP-wind speed forecasts.

The method includes a simple two-layer model of the atmospheric boundary layer, used in combination with a high-resolution roughness map. The two-layer is used to post-process direct NWP-model output. The model comprises a surface layer and an Ekman-layer. In the surface layer vertical wind speed transformations are done using the logarithmic wind speed profile. In the Ekman-layer geostrophic resistance laws are applied.

The roughness map is derived from a land-use map and a simple footprint model. The roughness lengths are wind direction dependent and the footprint area of the Ekman-layer extends farther upstream than that of the surface layer. The roughness lengths compare well to those derived from gustiness analysis for station locations. The adjustment of the surface wind after a roughness transition as modeled by the two-layer model is similar to that of internal boundary layer models.

The NWP-model wind and the downscaled wind are evaluated in coastal zone areas, in estuaries, and at an airport in the Netherlands. Verification against in-situ observations shows that the downscaling method reduces the NWP surface wind speed error significantly, largely in terms of bias. The quality of the downscaled wind, however, depends highly on the quality of the high-resolution roughness map: inaccuracies of the land-use map may lead to local errors in the downscaled wind.

### 5.1 Introduction

Detailed near-surface wind speed forecasts are of vital importance to many public sectors and industries such as aviation, wind energy, navigation and water management. Managing

operations in these fields requires wind information with a high level of spatial detail ( $< 1$  km). Most numerical weather prediction models provide information on spatial scales varying from 10 to 40 km. On scales smaller than the NWP-model grid, spatial wind speed variations are caused mainly by differences in roughness and stability, with roughness effects dominating at higher wind speeds. Surface roughness often varies on horizontal scales much smaller than the NWP-model grid and consequently the NWP-model wind forecasts lack representativity. Nowadays high-resolution land-use data, based on satellite observations, are available on scales as little as tens of meters. This enables the addition of greater detail to NWP-model winds.

This paper presents a high-resolution wind transformation model (henceforth called the 2L-model), that produces locally representative near-surface wind forecasts with a horizontal grid spacing of 500 m. Such high resolution is beyond the limit of current operational mesoscale models. The basis of the 2L-model is the assumption that sub-grid-scale wind speed variations are caused mainly by surface roughness changes. These variations can be modeled by boundary layer theory on the condition that the relevant roughness parameters are known.

The 2L-model was first developed as an interpolation method for surface wind measurements (Wieringa, 1986; Verkaik and Smits, 2001). In the present study NWP-model forecasts provide the input wind speed, which are downscaled by the 2L-model. The 2L-model adjusts the wind speed of the NWP-model output, so the downscaled results have the same averaging timescales as the NWP-model.

The 2L-model is applied to derive detailed forecasts of wind fields in the Netherlands for the coastal waters in the province of Zeeland, and for the take-off and touch-down area at Amsterdam Airport Schiphol. The model is computationally very efficient which enables several Dutch authorities in the field of water management to run the 2L-model at their own computer systems and generate high-resolution wind data on customized grids as input to their warning systems and models for sea state, waves and currents. The NWP-model output they receive from the Royal Netherlands Meteorological Institute (KNMI). In this paper verification results of the downscaled wind are presented for those regions. We focus on the merits of the 2L-model, the verification of the NWP-model is beyond the scope of this paper.

Downscaling models for wind have been the subject of earlier studies. Recently De Rooy and Kok (2004, henceforth DR&K) presented a method in which they also used a high-resolution roughness map in combination with a physical downscaling model, to correct for the sub-grid-scale variation of the NWP-model output. In addition, they used a statistical correction to compensate for the grid-scale NWP-model error. For the part of the sub-grid-scale variation their method and the 2L-model are similar except that their model uses a local, but directionally constant, roughness parameter in the downscaling, while the 2L-model uses roughness parameters that depend on wind direction. The 2L-model is therefore better suited for areas with large roughness transitions. DR&K determine the NWP-model error in every grid box from wind speed observations. After the introduction of a new version of the NWP-model, DR&K need to determine the NWP-model errors again. The 2L-model, however, can be applied directly.

## 5.2 Two-layer model of the ABL

The 2L-model is a simple 1-D boundary-layer model of the atmospheric boundary layer (ABL) in two layers. The lower layer is the surface-layer (SL) where Monin-Obukhov theory is used (Obukhov, 1971; Businger and Yaglom, 1971; Tennekes, 1973). In this layer there is a strong vertical gradient in wind speed. There is no change in wind direction. The neutral version of the logarithmic wind speed profile is used to express the dependence of wind speed  $U$  [m s<sup>-1</sup>] on height  $z$  [m]:

$$U(z) = \frac{u_{*l}}{\kappa} \ln \frac{z}{z_{0l}}. \quad (5.1)$$

Here the Von Kármán constant  $\kappa = 0.4$  (Frenzen and Vogel, 1995a; Frenzen and Vogel, 1995b), and  $u_{*l}$  [m s<sup>-1</sup>] is the local friction velocity. The friction velocity is a measure for momentum transfer at the surface by friction:  $\tau = \rho u_*^2 = -\rho \overline{u'w'}$ . Here  $\tau$  is the surface tension,  $\rho$  is the density of air, and  $\overline{u'w'}$  is the covariance of the turbulent fluctuations of the longitudinal and vertical components of the wind speed. The roughness length used in this layer is the local roughness length  $z_{0l}$  [m].

In the second layer, the wind speed increases further and in addition the wind direction veers (turns clockwise) in the northern hemisphere. Following Brown (1982) and Garratt (1992) we will call this layer the Ekman-layer (EL). The wind veering is described by the introduction of a second wind speed component, perpendicular to the surface wind speed. The geostrophic resistance laws are applied to relate the wind speed at the top of the ABL to the friction velocity (Garratt, 1992, cf. chapter 3):

$$\begin{aligned} U_{\text{macro}} &= \frac{u_{*r}}{\kappa} \left[ \ln \frac{h}{z_{0r}} - A \right], \\ V_{\text{macro}} &= -\frac{u_{*r}}{\kappa} \text{sgn}(f) B. \end{aligned} \quad (5.2)$$

Here  $U_{\text{macro}}$  and  $V_{\text{macro}}$  are the components of the wind speed at the top of the EL, the macrowind, and  $u_{*r}$  is the regional friction velocity.  $U_{\text{macro}}$  is parallel to the surface wind,  $V_{\text{macro}}$  is perpendicular to  $U_{\text{macro}}$ . With  $U_{\text{macro}}$  in eastward direction,  $V_{\text{macro}}$  points northward. The Coriolis parameter  $f$  [s<sup>-1</sup>] equals  $2\Omega \sin \phi = 1.1 \cdot 10^{-4}$  Hz at latitude 52° North, where  $\Omega$  is the angular velocity of the Earth's rotation and  $\phi$  is the latitude. The roughness length used in this layer is the regional roughness length  $z_{0r}$ ,  $h$  is the ABL-height. For  $A$  and  $B$  the values for neutral stability of the parameterization by Arya (1977) are adopted:  $A = 1.9$  and  $B = 4.5$ . For neutral boundary-layers an alternative formulation for Eq. 5.2 is available in which the ABL-height is no longer required as external parameter. We prefer to use Eq. 5.2, which is the neutral limit of the non-neutral form of the geostrophic resistance laws, including the ABL-height. Comparison of downscaled wind speeds with measurements showed that this approach performs better than using the neutral formulation without the ABL-height.

The objective of the 2L-model is to model the roughness induced wind speed differences at the surface. The relative magnitude of the wind speed variations decreases with height. While there may be large wind speed variations at the surface, at higher levels the wind speed will be much more horizontally homogeneous. The smaller the horizontal scale of the surface roughness heterogeneity, the lower the blending height, i.e. the height at which the wind speed variations blend into the mean flow. At the blending height the average wind speed can be assumed horizontally constant. This is the basis of many interpolation and

downscaling techniques (Wieringa, 1986; Bergström et al., 1988; De Rooy, 1995; Hutjes, 1996). In the 2L-model the blending is achieved in two steps. We assume that the small-scale wind speed variations have blended at the top of the SL ( $\approx 60$  m height), and the large-scale variations at the top of the ABL ( $\approx 0.5$ – $1$  km height). The wind at the top of the ABL can be mathematically interpolated. So, a small-scale, local roughness parameter is used in the SL and a regional roughness parameter is used in the EL.

The downscaling of NWP-winds using the 2L-model goes as follows (see Fig. 5.1). The friction velocity  $u_*$  is computed from the 10-m wind and the NWP-model roughness using Eq. 5.1. Next the wind speed at the top of the EL is computed from Eq. 5.2. The wind speed at the top of the EL is interpolated bi-linearly to the target location. At the target location the wind speed at the top of the SL is then computed from Eq. 5.2 and the regional roughness of the target location, and then the surface wind speed at the target location is computed using Eq. 5.1 and the local roughness.

The 2L-model is used assuming neutral atmospheric stability. This may seem to be a severe limitation of the applicability of the 2L-model but it is not: as will be shown the error in the wind speed estimate that enters in the upward transformation from the negligence of stability effects is counterbalanced in the downward transformation (De Rooy and Kok, 2002). For this reason the 2L-model could also be used for the interpolation of climatological wind fields when data on local stability is often not available.

In the present application the input wind speed is provided by the NWP-model. Besides the surface wind speed, the NWP-model provides wind speed at elevated levels as well as information on ABL-height and stability (Vogelezang and Holtslag, 1996). So if the 2L-model is used in combination with a NWP-model, it is possible to bypass the upward transformation at the input grid and start with the mathematical interpolation of the NWP-model wind at ABL-height level. The counterbalancing stability effect is then negated and the geostrophic resistance laws and the logarithmic wind speed profile must be used including stability corrections. In this paper we will show that this approach was not successful. The main reason for this failure is the problems we had with the determination of an accurate stability parameter from the NWP-model in stable conditions. The geostrophic resistance laws and the logarithmic wind speed profile require the Obukhov length stability parameter ( $L$ ). In the NWP-model  $L$  is not used. It has to be deduced from the wind speed and temperature gradients between model layers. However, we have not succeeded in finding a method that yields an appropriate value for  $L$  for all weather types. Moreover, the NWP-model we used was known for having a problem modeling stable boundary layers, too strong vertical mixing, which has been a common problem to many NWP-models. Therefore, in the present application of the 2L-model we will use the NWP-model surface wind as input and will apply the neutral version of the geostrophic resistance laws and the logarithmic wind speed profile.

In barotropic situations the macrowind approximates the geostrophic wind, i.e. the wind is parallel to the isobars. In baroclinic conditions the macrowind may deviate from the geostrophic wind and the NWP-model wind at ABL-height may be quite different as well. As discussed, this is not relevant to the wind speed transformation. However, the direction of the macrowind is used to determine the footprint for the regional roughness. If the turning of the wind direction with height deviates significantly from that in neutral situations, for example in cases of strong cold advection, the direction of the footprint may be in error.

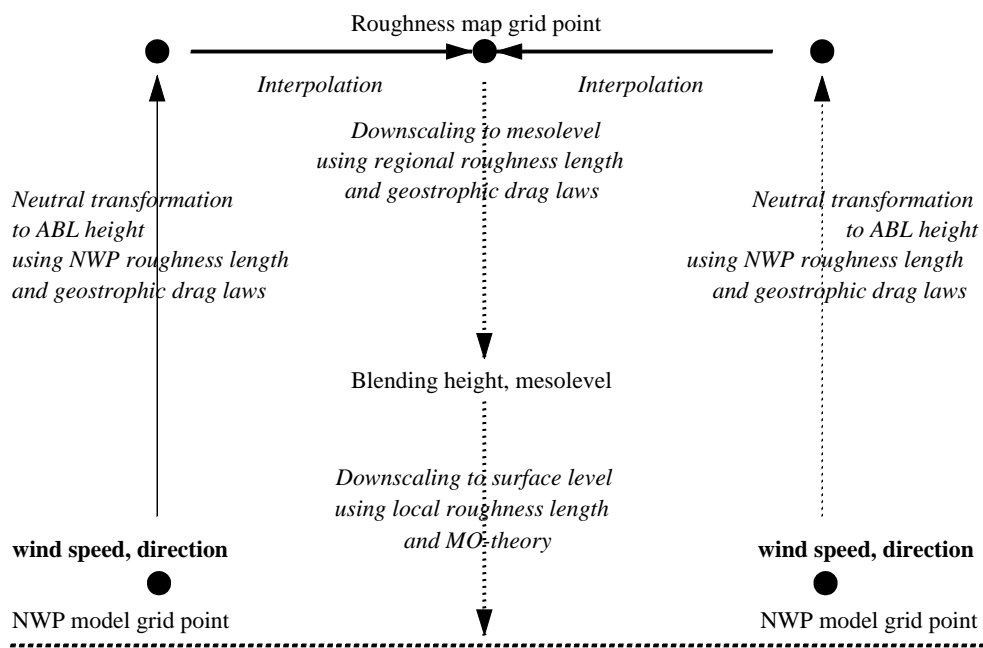


Figure 5.1: Schematic diagram of the downscaling method.

## 5.3 The roughness map

The 2L-model requires roughness lengths for the SL and EL. These are derived using a simple footprint model for a locally regular grid covering the Netherlands with a resolution of 500 m. Because of the detail of the land-use map and the considerable size of the footprint, the evaluation of the roughness map is computationally very demanding. So the roughness map is not determined in run-time, but for every 500-m point in the domain the wind direction dependent roughness length is determined prior to running the downscaling method. The roughness caused by water, if present in the footprint, is treated separately since it has to be computed in run-time when the wind speed is available.

### 5.3.1 Spatial data on land-use

The roughness map is derived from the high-resolution land-use map LGN3+ (De Wit et al., 1999). This map is a raster file covering the Netherlands with a resolution of 25 m. Every pixel in the map represents a typical land-use class. The accuracy, defined as the chance that the actual land-use is correctly classified, in LGN3+ is over 90% for built-up areas and most nature areas. The reliability, defined as the chance that the correct land-use type is found at a pixel classified by that land-use, is over 90% as well for most land-use types in LGN3+.

To each of the land-use classes in LGN3+ we assigned a roughness length adopted from literature Wieringa (1993). In Table 5.1 the land-use classes and the assigned roughness lengths are listed. Two classes were added to LGN3+: airport runways and parking lots.

Table 5.1: Land-use classes in LGN3+ and the assigned roughness lengths.

Class Name	$z_0$ (m)	Class Name	$z_0$ (m)
no data	0.03	grass	0.03
maize	0.17	potatoes	0.07
beets	0.1	cereals	0.16
other agricultural crops	0.04	greenhouses	0.1
orchards	0.39	bulb cultivation	0.1
deciduous forest	0.75	coniferous forest	0.75
fresh water	0.001	salt water	0.001
continuous urban area	1.6	built-up in rural area	0.5
deciduous forest in urban area	1.1	coniferous forest in urban area	1.1
built-up area with dense forest	2.	grass in built-up area	0.03
bare soil in built-up area	0.001	main roads and railways	0.1
buildings in rural area	0.5	runways	0.0003
parking lots	0.1	salt marshes	0.0002
beaches and dunes	0.0003	sparsely vegetated dunes	0.06
vegetated dunes	0.02	heath lands in dune areas	0.03
shifting sands	0.0003	heath lands	0.03
heath lands with minor grass	0.04	heath lands with major grass	0.06
raised bogs	0.06	forest in raised bogs	0.75
miscellaneous swamp vegetation	0.03	reed swamp	0.1
forest in swamp areas	0.75	swampy pastures in peat areas	0.07
herbaceous vegetation	0.03	bare soil in natural areas	0.001

This was done because in LGN3+ concrete runways and airport platforms were included in the category “built-up area”. Consequently, the roughness was strongly overestimated in these areas. This proved to be especially troublesome in the validation of the downscaling method using measurements done at airports. The problem could be solved partially by correcting the land-use map. The runways were identified by hand and added to the new class with low roughness. The same applies to large parking lots in the Amsterdam Airport Schiphol area. However, the corrections applied to the land-use map of Schiphol are very crude and far from complete as yet.

No data on land-use in the neighboring countries Germany and Belgium are available to us at present. Therefore we do not use test stations close to the national border in this study. Neither did we include seasonal effects of canopy growth or deciduous trees dropping their leaves in winter on the roughness length.

### 5.3.2 Surface elevation

In the major part of the Netherlands orography plays a minor role. However, in some areas orography does add to the total roughness and therefore it is taken into consideration. Surface elevation is assessed from the GTOPO30<sup>1</sup> database. In this database the surface

<sup>1</sup><http://edcdaac.usgs.gov/gtopo30/gtopo30.html>

elevation is given at a resolution of  $(1/120)^\circ$  ( $\approx 1$  km). This grid has been interpolated using spline approximation techniques and exported into a new grid on a 500-m resolution in local  $(X, Y)$ -coordinates. Height differences are assessed by comparing the height at point  $(X, Y)$  with the neighboring points on the 500-m grid.

The roughness length due to orography  $z_{0H}$  is computed from

$$z_{0H} = 0.2 \cdot \Delta H^2 / L, \quad (5.3)$$

where  $\Delta H$  is the maximum height difference over distance  $L$  (Agterberg and Wieringa, 1989), here  $L = 500$  m.

The resolution of GTOPO30 is not high enough to resolve small hills, dikes, etc. In the coming years a high-resolution elevation map of the Netherlands will become available. Then this part of the roughness map will need to be revised. It should also be noted that although orography adds to the roughness on large scales, on small scales orography may induce acceleration of wind and complex circulation patterns around hills (Jackson and Hunt, 1975; Jacobs, 1984). In the 2L-model these effects are not incorporated. So in cases where orographic forcing on the flow is not resolved by the NWP-model, the 2L-model will not solve this problem.

### 5.3.3 Area-averaged surface roughness

A suitable manner to aggregate surface roughness is to average the drag coefficients at the blending height (Wieringa, 1986; Mason, 1988; Claussen, 1990). This method gives stronger weight to the larger roughnesses in the averaging domain. The blending height is a function of the horizontal scale of the roughness fluctuations. Small-scale roughness fluctuations lead to a stronger enhancement of the effective roughness than large-scale fluctuations, although the roughness lengths and their areal fractions are equal (Schmid and Bünzli, 1995). We use a fixed blending height of 60 m at which the drag coefficients are averaged, following Wieringa (1986). This corresponds to the maximum SL-height. In areas with small-scale ( $\lesssim 1$  km) roughness fluctuations this method slightly underestimates the effective roughness in comparison to other estimates (Baldauf and Fiedler, 2003). For the regional roughness, averaging can be done at a higher level. However, using a higher level does not lead to significantly different roughness values for the regional roughness. So we average the drag coefficients at 60-m height for the regional roughness as well.

The neutral drag coefficient is defined as  $C_d \equiv (u_* / U)^2$  and assuming a neutral logarithmic wind speed profile (Eq. (5.1)) it can be expressed as

$$C_d = \left[ \frac{\kappa}{\ln(z/z_0)} \right]^2. \quad (5.4)$$

The roughness due to orography can also be expressed as a drag coefficient using this equation. The orographic drag can be added to the ‘skin drag’. Next, Eq. (5.4) can be inverted to compute the roughness length from the total drag.

### 5.3.4 Drag relation for water

The roughness of water is a strong function of wind speed. It also depends on wave age and water depth. Consequently, an average roughness length cannot be given independently of

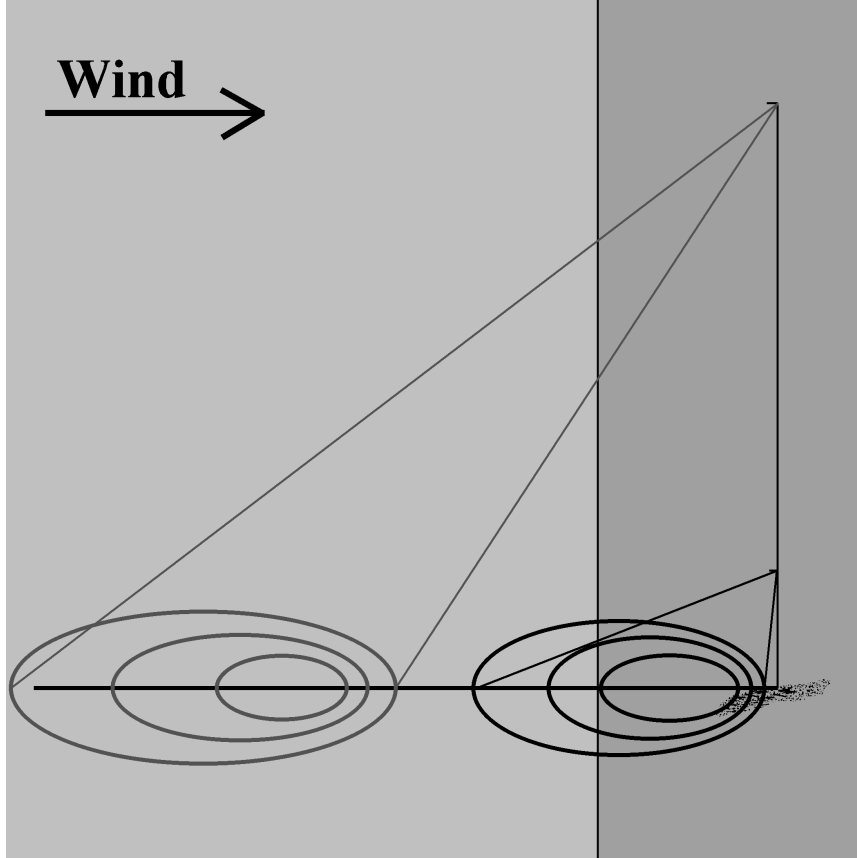


Figure 5.2: Illustration of the footprint for two different measuring heights near a coastline. All numbers and scale ratios in this example are fictitious.

the wind speed. The roughness of the water in the footprint can therefore be determined only during runtime.

The total drag at the evaluation point for wind directions in sector  $j$  is computed from

$$C_d = C_{d,j} + f_{w,j} \cdot C_{water}(U), \quad (5.5)$$

where the drag of water can be expressed using Eq. (5.4) and the Charnock relation

$$z_0 = \alpha \cdot u_*^2 / g, \quad (5.6)$$

where  $g$  is the acceleration of gravity [ $9.82 \text{ m s}^{-2}$ ] and for  $\alpha$  the value 0.017 is used, which applies to long fetches over deep seas (Charnock, 1955; Garratt, 1977). For shallow waters, values as large as 0.032 have been reported for  $\alpha$  (Onvlee, 1993; Benschop, 1996). In the NWP-model the value of 0.017 is used and we hold on to that value to prevent a bias in the downscaled wind speed over sea. Basically,  $\alpha$  is determined by the wave conditions which in turn are a function of wind speed, water depth and wave age. The lower limit of  $z_0$  is given by  $0.1\nu/u_*$  where  $\nu$  is the kinematic viscosity of air ( $1.5 \cdot 10^{-5} \text{ m}^2 \text{ s}^{-1}$ ) (Makin, 2003).

Although wave growth in models is sensitive to the drag relation, for wind speed the exact form of the drag relation is less crucial. This is because the wind speed always depends on  $z_0$  in a logarithmic way:  $U \propto \ln(z/z_0)$ . For large values of  $z/z_0$ ,  $U$  becomes a weak function of  $z_0$ .

## 5.4 Footprint model

During the advection of air parcels in the ABL by the flow, their physical properties are influenced by the surface properties. Consequently, meteorological parameters observed at a certain location will reflect the surface properties upstream of this location, the source area. The source area can be estimated from footprint models (Schmid, 1994; Horst and Weil, 1992; Horst, 1999). The footprint area for the average wind speed at a 10-m height over open terrain extends several hundred meters upwind. On shorter distances significant changes in the wind speed can be expected in the vicinity of obstacles. The flow around these obstacles, however, can not be described by the logarithmic wind speed profile.

In Fig. 5.2 an illustration of the footprint for two different measuring heights near a coastline is given. At some distance inland we imagine a measuring tower with sensors at two heights. The wind is onshore. The footprint of the lower sensor is small and is close to the tower. This is indicated by the ellipsoids at the surface, partially over land and partially over water. The inner ellipsoid could represent the area which determines 50% of the measured entity by this sensor, the outer ellipsoid represents the 90% area. All numbers and scale ratios in this example are fictitious.

### 5.4.1 Footprint approximation

Here we will make a simple approximation of the footprint using the following procedure. The area surrounding the evaluation point is split into 72 direction sectors each  $5^\circ$  wide. For each pixel  $i$  in sector  $j$  the drag coefficient at the blending height is determined from the equation

$$C_{d,i} = \left[ \frac{\kappa}{\ln(z_{bh}/z_0)} \right]^2. \quad (5.7)$$

The roughness length is determined from Table 5.1. The drag coefficient of water is wind speed dependent and is not added to the total drag at this stage.

A weighted average of  $C_{d,i}$  is computed using the weighting function

$$W(x_i, D) = \exp(-x_i/D), \quad (5.8)$$

where  $x_i$  is the distance from the source area to evaluation point, and  $D$  is a length scale determining the size of the footprint. We use 600 m for the local footprint, and 3 km for the regional footprint (see section 5.4.2). The average drag coefficient of sector  $j$  is given by

$$C'_{d,land,j} = \frac{\int_S \delta(\text{land}) W(x_s, D) C_{d,s} ds}{\int_S W(x_s, D) ds}, \quad (5.9)$$

$$C'_{d,water,j} = \frac{\int_S \delta(\text{water}) W(x_s, D) C_{water}(U) ds}{\int_S W(x_s, D) ds} = f'_{w,j} \cdot C_{water}(U). \quad (5.10)$$

Here  $\delta(\text{land})$  equals 1 if the considered pixel is covered by land and  $\delta = 0$  otherwise. Similarly  $\delta(\text{water}) = 1$  for water and 0 otherwise.  $C_{water}(U)$  will be determined in runtime when  $U$  is available.  $f'_{w,j}$  represents the weighted fraction of water in the footprint.

For practical reasons only the source area up to a distance of  $3 \times D$  is considered. This corresponds to 80% of the total integral  $\int_0^\infty \phi x \exp(-x/D) dx$  ( $\phi x \cdot dx$  is the surface area at distance  $x$ ,  $\phi$  is the width of the sector in radians). Note that the relative surface contribution to the weighted sum reaches a maximum at distance  $D$ .

Now the direction dependent  $C'_{d,j}$  and  $f'_{w,j}$  are smoothed using a weighted moving average:

$$C_{d,j} = \sum_{k=-2}^{k=2} w_k \cdot C'_{d,j+k} \quad \text{and} \quad (5.11)$$

$$f_{w,j} = \sum_{k=-2}^{k=2} w_k \cdot f'_{w,j+k}, \quad (5.12)$$

where  $w_{-2,-1,\dots,+2} = \{0.08, 0.13, 0.18, 0.22, 0.18, 0.13, 0.08\}$ . This bell shape has been chosen in accordance with sophisticated footprint models (Schmid, 1994).

## 5.4.2 Footprint length scales

Footprint length scales have to be selected for the regional and local roughness,  $D_r$  and  $D_l$  respectively. The footprint dimensions depend on roughness, measuring height, and stability (Horst and Weil, 1994; Schmid, 1994). The roughness map can not be assessed in run-time, so we use fixed values for  $D_r$  and  $D_l$ . Estimates for the footprint length scale can be made from the literature. It is also possible to validate the roughness lengths from the footprint model with estimates from other sources and adjust the footprint length scales to reach a satisfactory resemblance (section 5.4.3). The footprint length scales determine the rate at which the surface wind speed will adjust to a new surface roughness after a roughness transition. So internal boundary-layer models may serve as a reference as well (section 5.4.4).

The wind speed profile up to height  $z$  will only in equilibrium with the local surface roughness if that roughness extends  $100 \times z$  upstream (Bradley, 1968; Rao et al., 1974; Duijm, 1983). Fetches of more than 10 km are required before the SL is in complete equilibrium according to Taylor (1987). An estimate for the regional footprint length scale can be made from Schmid (1994, cf. figure 5h). It shows that with  $O(z/z_0) = 10^2 \rightarrow O(D_l/z_0) = 10^3 \dots 10^4$  in near-neutral conditions. This implies that  $D_l$  will be several hundreds of meters. Most of the footprint estimates and fetch requirements apply to the SL only. Hardly any references are available for the regional footprint length scale or roughness length. Jensen (1978) argued that for the whole ABL to be in equilibrium, homogeneous fetches of several tens of kilometers are required. So  $D_r$  will be at least several kilometers, but a solid estimate is hard to establish.

## 5.4.3 Comparison with gustiness measurements

The roughness map can be verified by comparing the roughness length to that of other sources. The canonic way to determine the roughness length at a certain location is by determining the wind speed profile. Accurate instrumentation and careful interpretation is required to do so (Wieringa, 1980b; Wyngaard et al., 1982; Horst, 1999). Assessment of the roughness length from profiles is therefore limited to specific research sites and it is unfeasible to analyze large areas this way. There are alternative methods, however, based on turbulence statistics from measurements at a single level (Sozzi et al., 1998). Gustiness analysis is one of these methods.

We will compare the local roughness length derived from the land-use map ( $z_{0l}$ ) to gustiness derived roughness lengths ( $z_{0gust}$ ) for the Dutch measuring station locations.

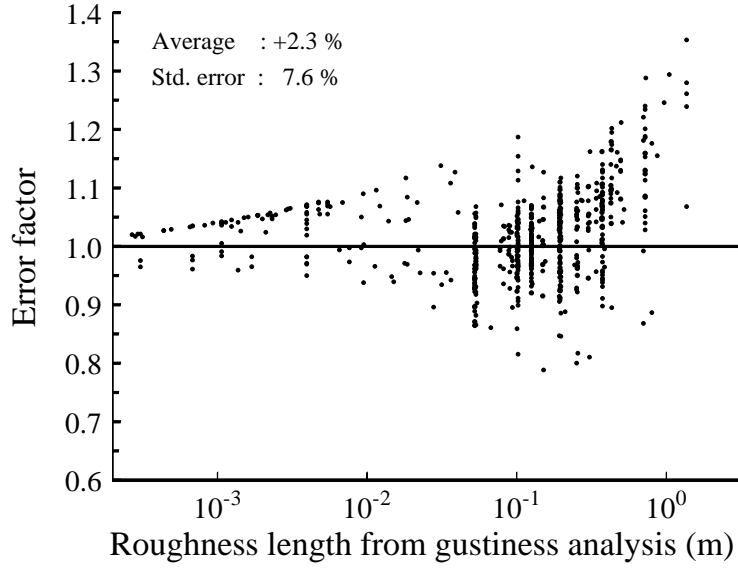


Figure 5.3: Comparison of the roughness lengths derived from gustiness to those from the footprint model and the roughness map. The error factor is obtained by the product of the transformation factor for wind speed from the surface level to the top of the surface layer using the gustiness derived roughness and the reverse transformation using the footprint roughness. An error factor larger than 1 implies that the gustiness roughness is larger than the footprint roughness.

These have been measured and analyzed at most Dutch wind stations since 1971 (Wieringa, 1976; Beljaars, 1987b; Verkaik, 2000). The gustiness derived roughness is a function of wind direction and, if the station's environment changes, also a function of time. The difference in roughness length will be expressed as follows. The ratio ( $f_1$ ) of the 60-m wind to the 10-m wind is computed from of Eq. (5.1) using  $z_{0\text{gust}}$ :

$$f_1 = \ln(60/z_{0\text{gust}}) / \ln(10/z_{0\text{gust}}), \quad (5.13)$$

and the ratio  $f_2$  is that of the 10-m wind to the 60-m wind using  $z_{01}$  from the roughness map:

$$f_2 = \ln(10/z_{01}) / \ln(60/z_{01}). \quad (5.14)$$

The error factor is

$$\text{Error factor} = f_1 \cdot f_2. \quad (5.15)$$

With a perfect match ( $z_{01} = z_{0\text{gust}}$ ) the error factor equals 1.

The average error factor and its standard deviation have been determined for a range of values for  $D_1$ . Best results were found for  $D_1 = 0.6$  km. Then the average error factor is 1.023 with a standard deviation of 0.076.

In Fig. 5.3 the error factor is plotted for 34 stations for  $D_1 = 0.6$  km. For each station  $z_{0\text{gust}}$  has been determined for recent years. It has been computed for 18 wind direction

sectors of  $20^\circ$  wide. From this figure it can be seen that for sectors with a low  $z_{0\text{gust}}$  the error is usually less than 10%. The cluster of points with high  $z_{0\text{gust}}$  comprises most of the onshore stations. In this cluster there is a slight trend of increasing error with increasing  $z_{0\text{gust}}$ . This implies that for large  $z_{0\text{gust}}$ ,  $z_{01}$  tends to fall behind. Close examination of some obvious errors reveals that often the land-use map is in error in these cases. This is partially due to its finite resolution. With a pixel size of  $(25 \text{ m})^2$  isolated obstacles may not be resolved. These obstacles can have a large impact on the observed gustiness and wind speed.

In the sectors with low  $z_{0\text{gust}}$  there is often water present in the footprint. The error factor in these sectors is more often larger than 1. This could be the result of our choice for  $\alpha = 0.017$  in Eq. (5.6). This value must be considered as a minimum, and may need enhancement.

#### 5.4.4 Comparison with internal boundary-layer models

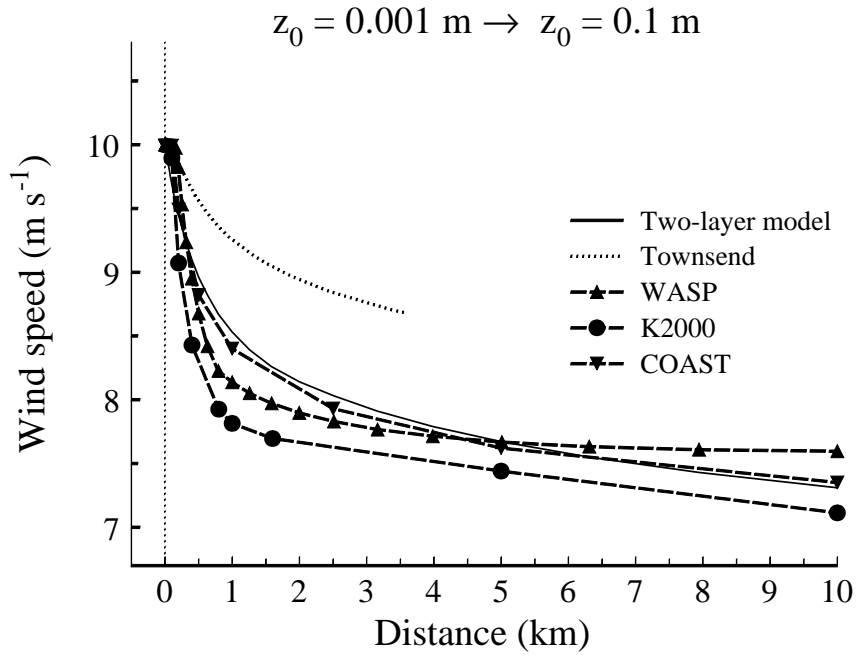
The rate at which the surface wind speed adjusts to a new surface roughness in the 2L-model is described by  $D_1$  and  $D_r$ . Increasing  $D$  will increase the length of the fetch required to achieve a new equilibrium. This response rate can also be described by internal boundary-layer models (IBL-models). Here we will compare the development of the wind speed after a roughness change in the 2L-model to that of IBL-models. Most IBL-models have been developed for the SL only. However, there are IBL-models developed for the whole ABL as well. From these models a regional footprint length scale may be found.

We consider the sea–land transition (and vice versa) where the land roughness length is 0.1 m. Beside the 2L-model we will use the IBL-models by Kudryavtsev et al. (2000, henceforth K2000), Troen and Petersen (1989, henceforth WASP), Van Wijk et al. (1990, henceforth COAST), and a surface layer IBL-model by Townsend (1965). For the 2L-model and Townsend’s model the roughness length of the sea is assumed to have a value of 0.001 m, the other models compute the drag of the sea from the wind speed. K2000 and COAST are used in near-neutral mode, the other models are neutral by themselves. A value of  $10 \text{ m s}^{-1}$  has been adopted for the wind at 10 m height over sea. The results are plotted in Fig. 5.4. The 2L-model is used with  $D_1 = 0.6 \text{ km}$  and  $D_r = 3 \text{ km}$ . Fig. 5.4(a) shows the sea–land transition, Fig. 5.4(b) the land–sea transition where the wind speed over land is fixed at  $7 \text{ m s}^{-1}$ . COAST is developed for onshore flow only.

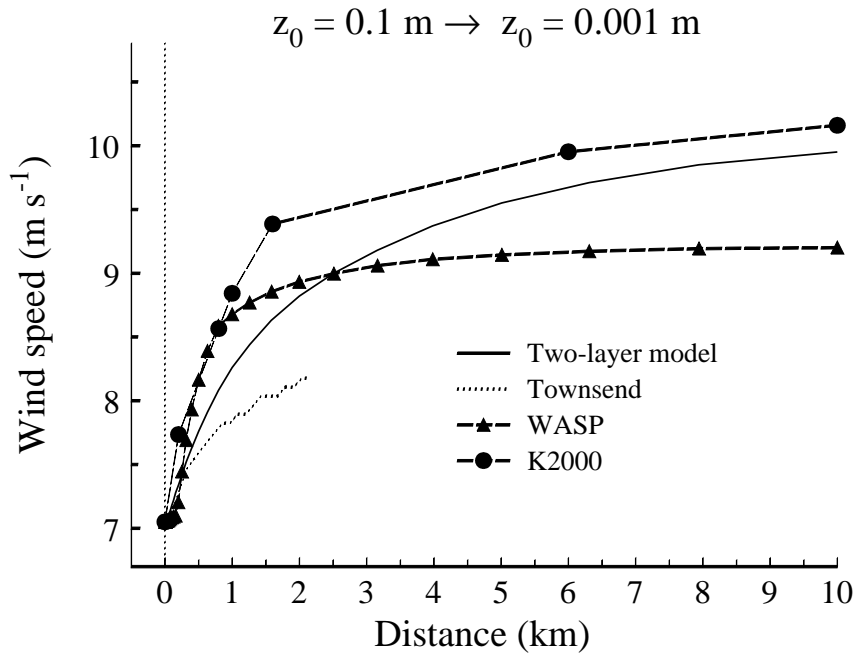
Apart from Townsend’s model, all models show a similar adjustment of the 10-m wind to the new surface roughness for short fetches. The 10-m adjustment in the 2L-model compares well to the IBL-models. However, for short fetches the 2L-model adapts slower than most IBL-models. This suggest a smaller value to be used for  $D_1$ . For this study the map with  $D_1 = 0.6 \text{ km}$  was the only one available, however.

Although the development of the 10-m wind after a change in roughness in the 2L-model is similar to that of IBL-models, there are important conceptual differences between IBL-models and the 2L-model. Simple IBL-models give a formula for the IBL-height growth rate and an assumption on the wind speed profile in the disturbed layer. In terms of the 2L-model the footprint of the profile above the IBL-height lies entirely upstream of the roughness transition and the footprint of the profile below the IBL-height lies entirely downstream of the roughness transition. The interface of the two layers climbs with fetch. In the 2L-model the interface is fixed at the blending height while the roughness lengths are gradually adjusting.

Every change in surface roughness will cause internal boundary-layers to emerge, so



(a) Smooth-to-rough transition.



(b) Rough-to-smooth transition.

Figure 5.4: The development of the wind speed in the 2L-model compared with several IBL-models: the surface layer IBL-model by Townsend (1965); the Wind atlas analysis and application programme Troen et al. (1989, WASP); the analytical IBL-model of the full ABL by Kudryavtsev et al. (2000, K2000); the surface layer IBL-model by Van Wijk et al. (1990, COAST).

their number may be large. IBL-models have difficulties handling many transitions and their validation in this context is also poor. Furthermore, IBL-models require a well defined sequence of roughness changes along a line upwind of the site of interest. This usually implies major simplifications to the roughness map.

#### 5.4.5 Sample of the roughness map – Zeeland estuaries

In Fig. 5.5(a) the surface roughness map of the NWP-model is presented for the Zeeland area. The resolution of the roughness map is  $0.1^\circ$ . Note that the NWP-model roughness lengths are small in most parts of the Zeeland province, even over land. In Fig. 5.5(b) the local roughness for the same area is plotted. The roughness of water is computed using homogeneous wind field ( $5 \text{ m s}^{-1}$  south-southwest). In contrast to the NWP-model roughness map there are sharp gradients in the local roughness map along the coastlines and urban areas.

The regional NWP-model roughness length at location Hansweert is compared to the direction dependent local and regional roughness lengths derived from the land-use map in Fig. 5.6. For comparison, roughness lengths derived by gustiness analysis are presented as well. For winds over land (offshore) the local roughness lengths in the SL are in good agreement with the gustiness analysis. Note that for offshore winds (directions northwest to northeast) the NWP-model roughness is much too low. For onshore winds (directions southwest to southeast), where the roughness is dominated by the presence of at least 80% water, the NWP-model roughness is too high. Note also that the difference between  $z_{0\text{gust}}$  and  $z_{0\text{l}}$  for onshore winds indicates that for this location the footprint length scales are chosen too small.

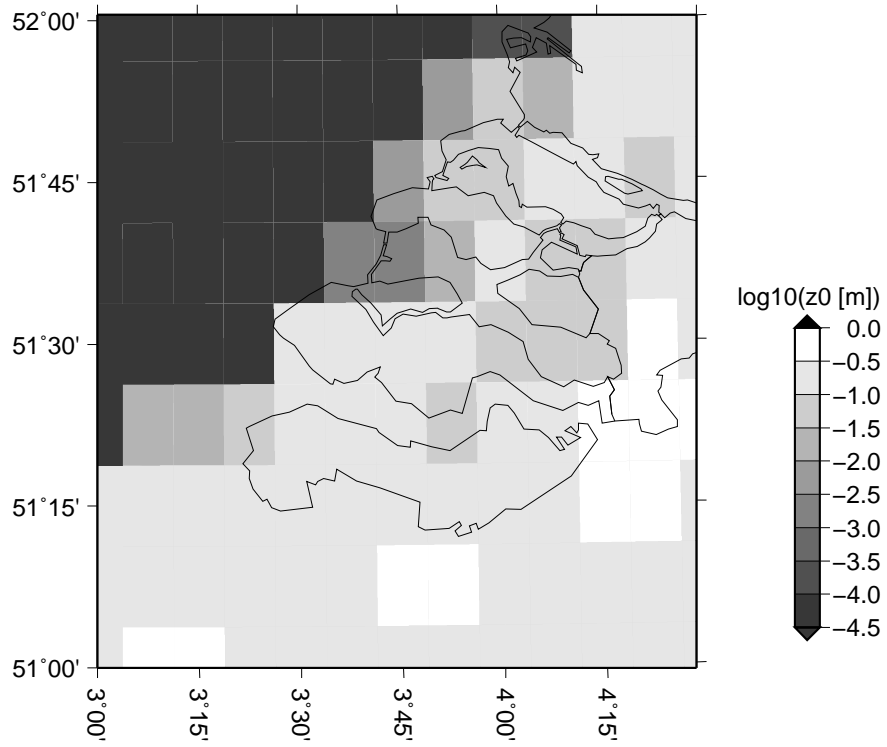
### 5.5 NWP-model data

The NWP-model that is used in the verification study to provide the necessary input data is the operational mesoscale Hirlam model. Hirlam is a weather forecasting and data-assimilation system with all the necessary physics such as cloud physics, convection, a turbulence parameterization, a soil parameterization and radiation. It is developed by the international Hirlam project (Undén et al., 2002). This is a joint effort of Denmark, Iceland, Ireland, Finland, the Netherlands, Norway, Spain and Sweden.

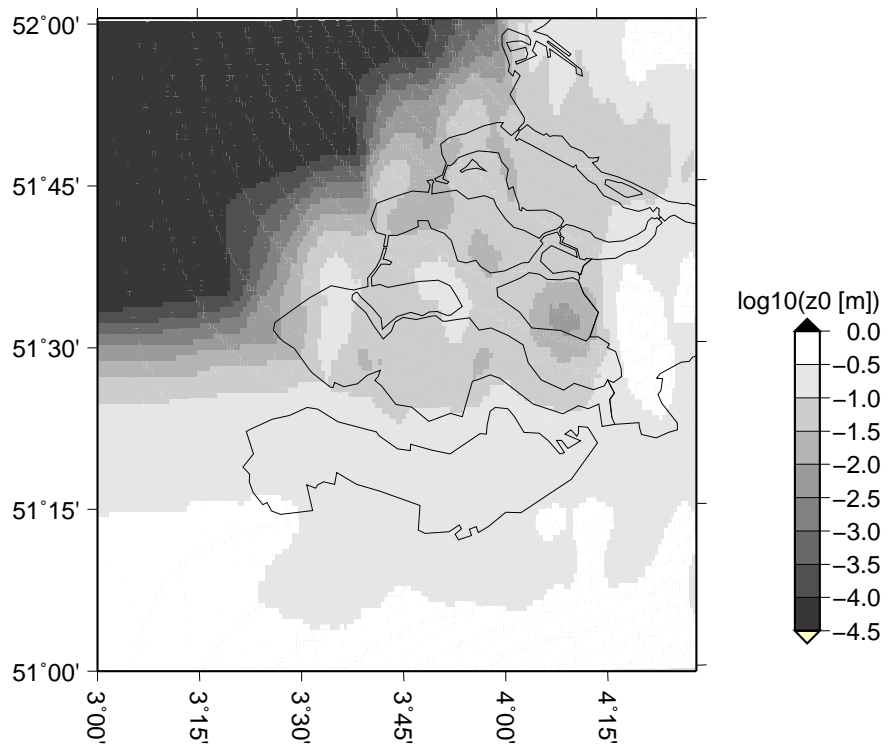
Hirlam is a limited area model like ETA, WRF or Aladin, that runs in a nested mode. The outer grid, covering the North Atlantic and Europe, has a horizontal resolution of  $0.2^\circ$  ( $\sim 22 \text{ km}$ ) and 31 layers in the vertical. The model is driven at the boundaries by the ECMWF model. It produces forecasts to +48 hour, four times a day. The inner grid, covering Northwest Europe, has a horizontal resolution of  $0.1^\circ$  ( $\sim 11 \text{ km}$ ) and 40 layers in the vertical. It produces forecasts to +24 hour, eight times a day.

The difference between the downscaled wind and the NWP-model wind depends mainly on the difference in roughness and the wind speed, the influence of the ABL-height is of minor importance and it does not depend on forecasts time. So, it is sufficient to verify only the +03 hour Hirlam forecasts, provided every 3 hours during the verification period. Due to spin-up problems in the Hirlam model, which results in an underestimation of initialized wind speeds, these +03 hour model forecasts are used rather than the initialized analysis.

The NWP-model provides the 10-m wind and the ABL height at the NWP-grid points. The 10-m wind and ABL height are interpolated to the high resolution grid of the land-



(a) NWP-model roughness map.



(b) Local roughness map.

Figure 5.5: Roughness maps of the Zeeland estuaries. The resolution of the NWP-model roughness map is  $0.1^\circ$ . The resolution of the local roughness map is 0.5 km. The local roughness map is derived for a homogeneous wind field ( $5 \text{ m s}^{-1}$  southwest).

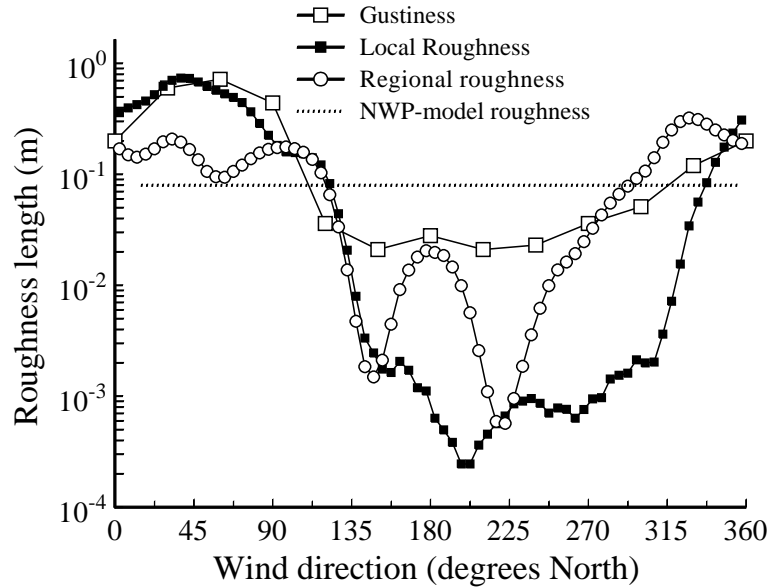


Figure 5.6: Roughness lengths at test location Hansweert. The gustiness derived roughness is compared to the local roughness, the regional roughness, and the (directionally constant) NWP-model grid scale roughness.

use map. This 10-m wind is used for comparison with the downscaled wind. The ABL height is calculated at the input grid points from the surface parameters and the model level parameters using the method of Vogelezang and Holtslag (1996). As the depth of the boundary layer in the Netherlands usually is less than 3 km, the use of 10 layers of Hirlam data is sufficient.

## 5.6 Verification

The verification results of the 2L-model are presented for three test sites: coastal, land, and offshore (see Fig. 5.7). The first test location, “Hansweert”, is located at a coastline in the Zeeland estuary. Hansweert is on the edge of a tidal waterway that is the main shipping route from the North Sea to the river Scheldt that provides access into the main land. This location was selected for its highly complex roughness map with large directional differences in roughness. The second location is the synoptic wind speed measurement site at Amsterdam Airport Schiphol (see Fig. 5.8 for details). This is a typical inland location with built-up areas. However, also at this site there are large directional differences in wind speed. The third location is the offshore site “Vlakte van de Raan”. This site is entirely surrounded by water. The smallest distance from the Vlakte van de Raan to the coast of Zeeland is about 20 km. Results have been collected from several more test locations. However, the results for other locations are similar to those presented in this paper. The coastal and land locations are selected for the large differences in roughness as function of wind direction. At the offshore site there are no differences between the NWP-model roughness map and the local roughness map at this site, so the comparison of the NWP-model wind and the downscaled wind can be used to assess to effect of atmospheric stability on the downscaling.

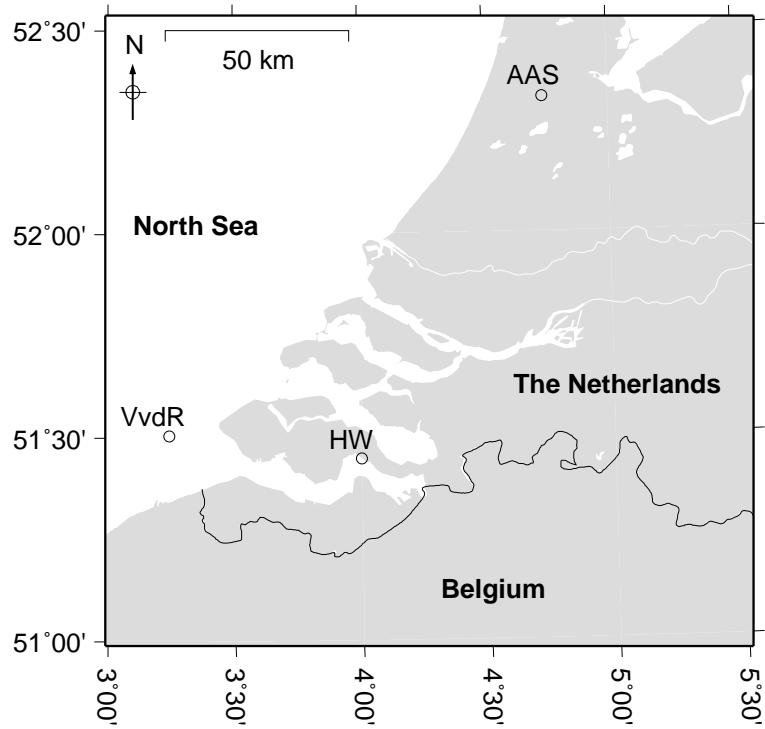


Figure 5.7: Map of the south-west part of The Netherlands. The test locations are encircled. The offshore site ‘VvdR’ indicates the site ‘Vlakte van de Raan’, inland ‘AAS’ indicates ‘Amsterdam Airport Schiphol’, and in the Zeeland estuaries ‘HW’ indicates ‘Hansweert’.

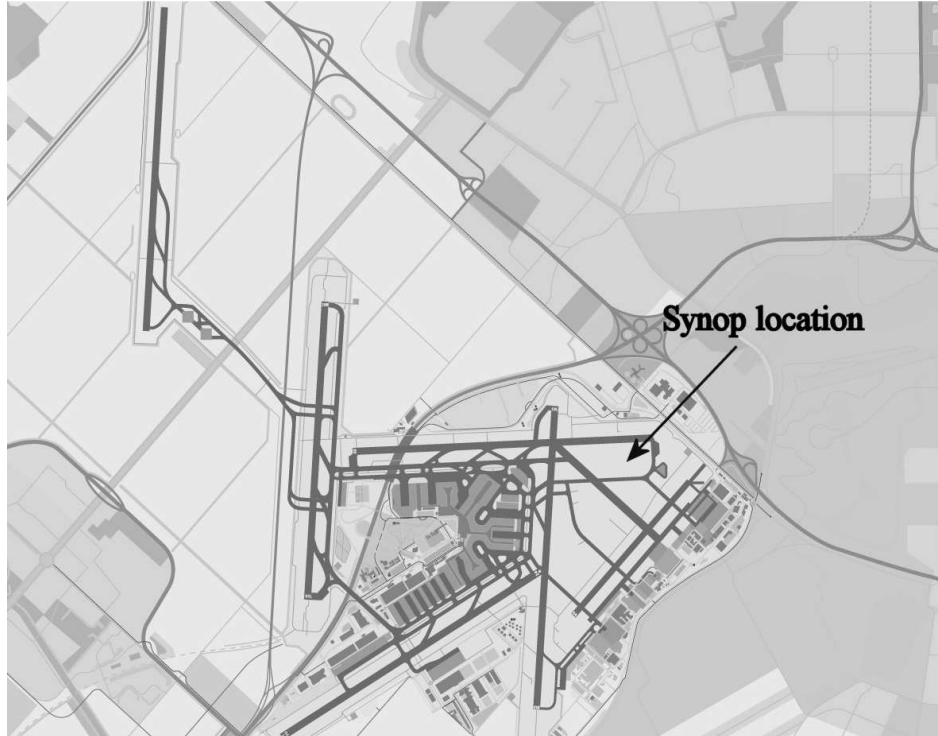


Figure 5.8: Map of the take-off and touchdown area at Schiphol airport. The size of map is about  $10 \times 8 \text{ km}^2$ . The arrow marks the synoptic wind measurement location used for validation.

For illustration purpose the impact of the local roughness on the wind in the ABL is demonstrated by comparing the results of 2L-model with the NWP-model winds. In Fig. 5.9(a) NWP-model wind at 10 m is plotted. The wind field, at a horizontal resolution of  $0.1^\circ$ , is interpolated bi-linearly to the 1 km resolution grid. In Fig. 5.9(b) the corresponding wind field produced by the 2L-model at a resolution of 1 km and at 10 m height is plotted. Note the abrupt changes in wind speed when the downscaled wind flow reaches the coast, whereas NWP-model winds change gradually near the coast. The downscaled winds over small water bodies can be more than 40% stronger than the NWP-model winds.

### 5.6.1 Observations

At the three test locations hourly observations were collected of the averaged wind speed and wind direction over the preceding ten-minute time interval. The measurement heights, relative to the station height, are 10 m at Schiphol airport and approximately 16.5 m at the measurement stations in Zeeland. The Zeeland measurements are corrected to the WMO standard height of 10 m. The reduction factor for the mean wind speed is based on a neutral logarithmic wind profile relation. The deviations of the corrected measurements from the wind speed at observation height are around 6% on average. The uncorrected measurements at 16.5-m height were not available to us in this period. In order to validate the downscaling model per wind sector, the observed wind direction was used to sample the data in  $30^\circ$ -intervals. Wind speeds less than  $3 \text{ m s}^{-1}$  were rejected in the verification analysis because for low wind speeds the wind direction is often variable.

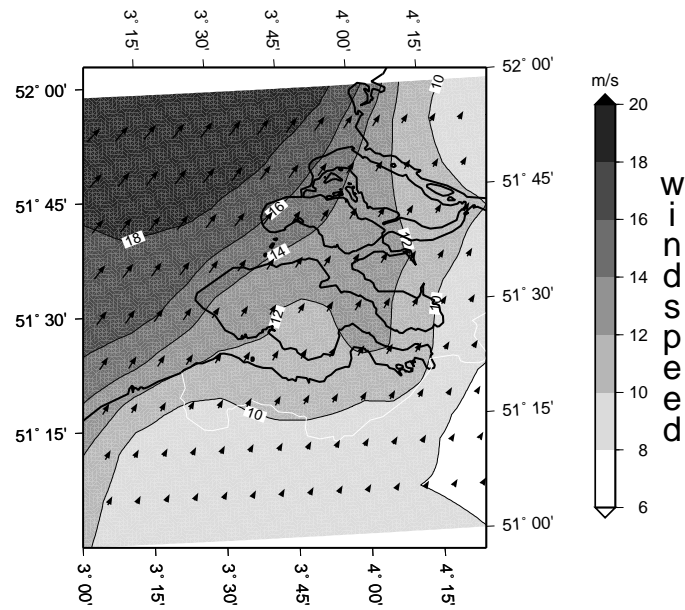
A first verification data set has been collected in the period November 2001–February 2002. During this period, the daily averaged atmospheric stability changed from unstable-neutral in the beginning to strongly stable at the end. In the first months of the verification period (November–December 2001) the sea was significantly warmer than the land surface and the atmosphere. For the province of Zeeland this period was predominantly unstable over land and over water. In the second half of January 2002, the sea was much colder than the land surface and the atmosphere. A warm airflow in that period resulted in a strongly stable, stratified atmosphere. This data set has been collected to test the running scores of both the neutral and non-neutral implementation of the downscaling method. A second data set has been collected in the period October 2003–August 2004 for the same stations. This data set has been used to validate the downscaling method as function of wind direction.

### 5.6.2 Verification results

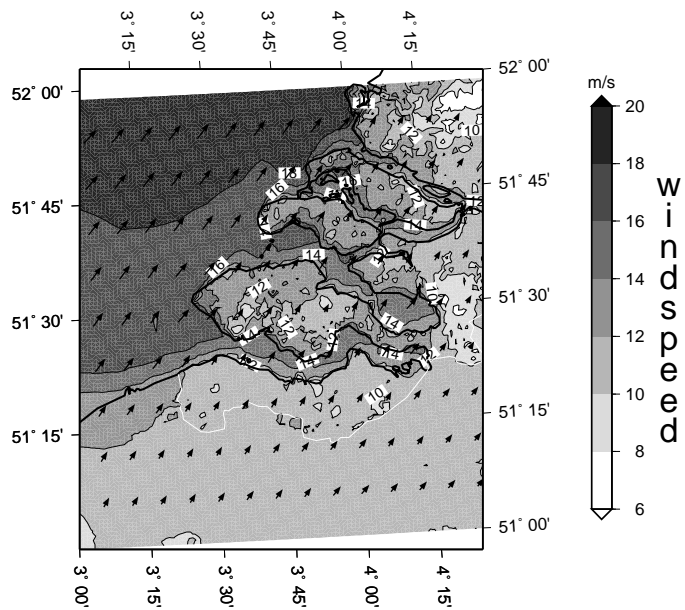
In the following results will be presented in terms of the mean error and the standard deviation of the error in the 10-m wind speed. The wind speed error is defined as

$$Error = Model - Observation,$$

where *Model* is the result of the Hirlam model or the downscaling method. The Hirlam model wind is interpolated bi-linearly to the observation location. The downscaled wind is the wind speed at the 500-m grid point nearest to the observation location. *Observation* stands for the measured mean wind speed over the preceding ten-minute time interval. The error statistics of the modeled wind direction are omitted in the presentation as those errors are generally small. Wind direction errors in the NWP-model and in the local wind flow computed with the downscaling method are  $10^\circ$  on average.

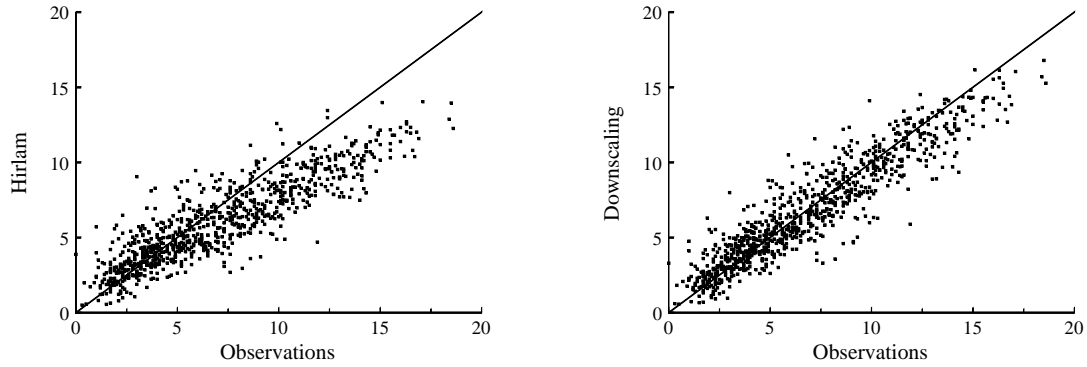


(a) NWP-model surface wind.



(b) Downscaled surface wind. The southern part of the map covers Belgium. We do not have land-use data for Belgium. A dummy value for the roughness is used here. Consequently the downscaled wind speed over Belgium is uniform.

Figure 5.9: Wind field at 10-m height for Zeeland valid for February 2002, 22nd 00h UTC. The color scale indicates the wind speed, the arrows indicate the wind direction. The prevailing wind direction is southwest.



(a) HIRLAM model wind speed versus in situ observations. (b) Downscaled wind speed versus in situ observations.

Figure 5.10: Scatter plot +3-hour forecast of the HIRLAM model wind and the downscaled wind versus the observed wind speed at Hansweert.

## Hansweert

Scatter plots of the modeled wind speed, computed by Hirlam and the 2L-model, versus the observed wind speed at location Hansweert are presented in Fig. 5.10. Fig. 5.10(a) shows that Hirlam underestimates the wind speed and the underestimation increases for stronger winds. Fig. 5.10(b) shows that the 2L-model leads to a major improvement of the surface wind. The downscaled wind estimates the measured wind speed better on average, the scatter is slightly reduced.

Fig. 5.11(a) and 5.11(b) show the 10-m wind speed error ( $30^\circ$ -wide bins) of Hirlam and the 2L-model for the location Hansweert for the summer and winter period, respectively. At Hansweert Hirlam underestimates the surface wind speed when the wind direction is between  $120^\circ$  and  $320^\circ$ , and overestimates the wind speed for other wind directions. Fig. 5.6 shows that the underestimation (overestimation) corresponds to the directions where the Hirlam roughness is larger (smaller) than the local and regional roughness. The predominance of southern winds in the Netherlands results in the overall underestimation of the wind speed by Hirlam in Fig. 5.10(a).

In Fig. 5.12(a) the running scores for Hansweert are presented for the period November 2001–February 2002 (7-day averaging window). A large negative bias is found for Hirlam, increasing to  $-3 \text{ m s}^{-1}$  during the stable period. The 2L-model method improves the surface wind for both periods with stable and unstable stratification: the bias is reduced significantly to an absolute value that is less than  $0.5 \text{ m s}^{-1}$  for the greater part of the verification period and for each wind direction.

## Amsterdam Airport Schiphol

In Figs. 5.11(c) and 5.11(d) the verification results are presented for location Amsterdam Airport Schiphol. The Hirlam bias is large for both the unstable and stable period (Fig. 5.12(b)) which shows that in general the Hirlam roughness that is used for Schiphol is too large. Variations in bias as a function of the wind direction are large. The maximum underestimation of the Hirlam surface wind occurs for southwesterly winds with a bias in the order of  $-3 \text{ m s}^{-1}$  (30–40%). In this direction the footprint is over the runway and the

roughness is very small. (cf. Fig. 5.8). For other wind directions, in which the wind mainly blows over built-up areas, the resulting Hirlam winds still underestimate the measured wind speed by  $1 \text{ m s}^{-1}$  on average.

As was already noted, the quality of the land-use map in the Schiphol area is poor: the concrete platforms of the airport are classified as built-up areas. As a result the regional roughness length for the 2L-model is generally too high as well and the 2L-model would underestimate the local wind speed, just like Hirlam. The 2L-model results in Figs. 5.11(c), 5.11(d) and 5.12(b) are achieved by using the local roughness for both the SL and the EL. Doing so the downscaling method improves the surface winds significantly. For the greater part of the verification period, and for most wind directions, the absolute value of the bias is less than  $0.5 \text{ m s}^{-1}$  in the summer period, and less than  $1 \text{ m s}^{-1}$  in the winter period.

### Vlakte van de Raan

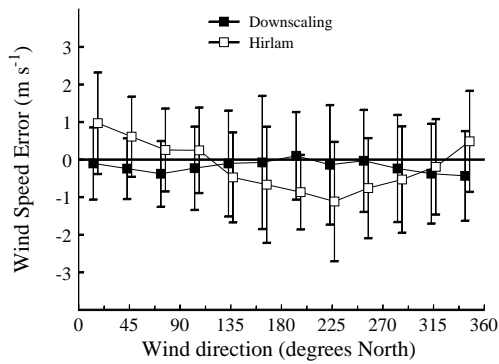
The verification scores for location ‘Vlakte van de Raan’ are presented in Figs. 5.11(e), 5.11(f), 5.12(d), and 5.12(c). In both Hirlam and the 2L-model the sea roughness is computed by application of the Charnock relation (Charnock, 1955; Garratt, 1977; Makin et al., 1995). The 2L-model replaces the Hirlam grid-box averaged surface roughness, which for the Vlakte van de Raan consists of sea roughness only, by the local roughness. As a result we may expect that at the Vlakte van de Raan the local wind computed by the 2L-model hardly differs from the grid-box averaged surface wind computed by Hirlam. This confirmed by Figs. 5.11(e) and 5.11(f). During summer as well as winter the mean error in the Hirlam surface wind, and consequently also in the downscaled surface wind, is less than  $1 \text{ m s}^{-1}$  for most wind directions.

Fig. 5.12(c) shows that the running scores of Hirlam and the 2L-model are identical as well. This figure proves that stability has little effect on the performance of the 2L-model. Both in stable and unstable conditions the negligence of stability effects in the upward transformation is counterbalanced in the downward transformation. This is a trivial result since in the same roughness length is used in the upward and downward transformation.

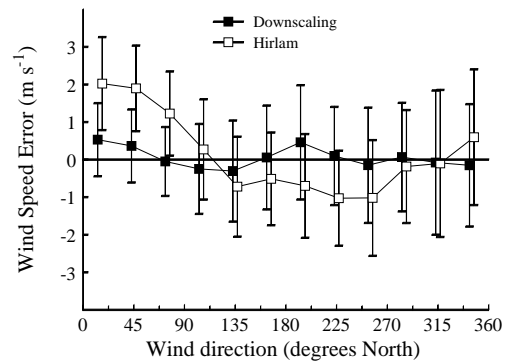
In Fig. 5.12(d) the running scores are plotted for the Hirlam forecast, and as derived after application of the non-neutral downscaling method. Here the Hirlam wind speed at the top of the ABL is used as input to the 2L-model and the stability, as derived from Hirlam, is taken into account in the transformation Eqs. 5.2 and 5.1. It is clear that the non-neutral downscaling method produces lower quality surface winds than Hirlam. Especially during the stable period, which starts in the second half of January 2002, the bias in the downscaled surface wind speed increases to almost  $4 \text{ m s}^{-1}$ . This large bias is caused by the stability corrections, since the Hirlam- and the 2L-model-roughness for this open-sea location is identical. During periods of neutral and unstable stratification (November–December 2001) the performance of the stability correction is better, but still slightly worse than the Hirlam performance.

## 5.7 Conclusions

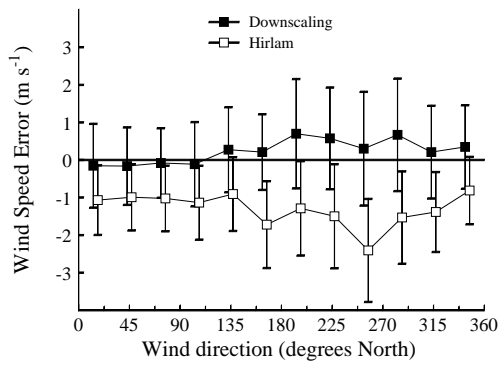
- The use of uniform, grid-box averaged, roughness information in NWP-models, to describe the local wind flow, leads to large errors in the representation of the wind in certain areas of the Netherlands.
- The 2L-model significantly reduces the mean error in the surface winds that are



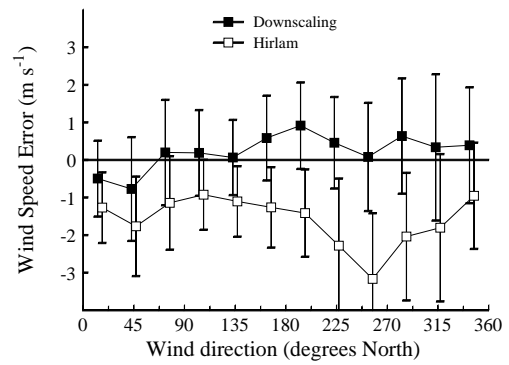
(a) Summer period at Hansweert.



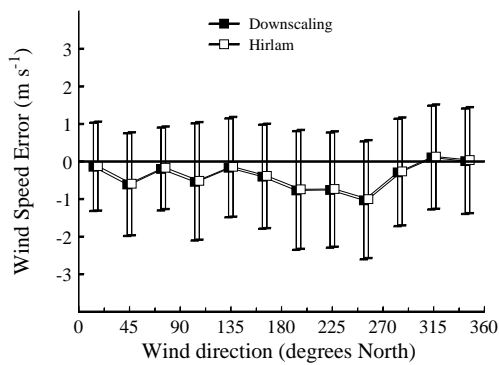
(b) Winter period at Hansweert.



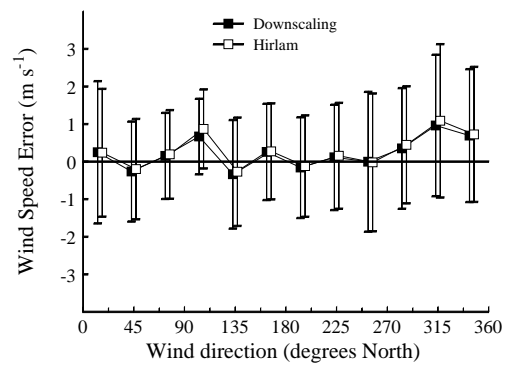
(c) Summer period at Schiphol.



(d) Winter period at Schiphol.

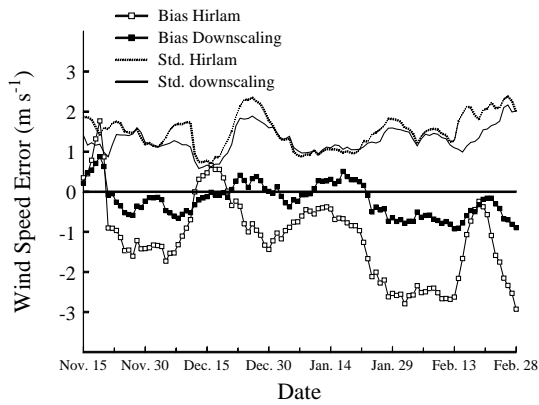


(e) Summer period at Vlake van de Raan.

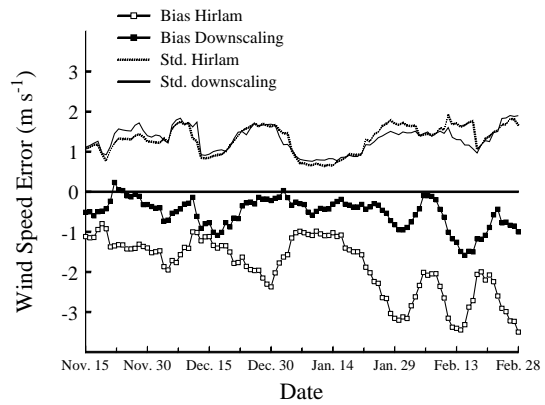


(f) Winter period at Vlake van de Raan.

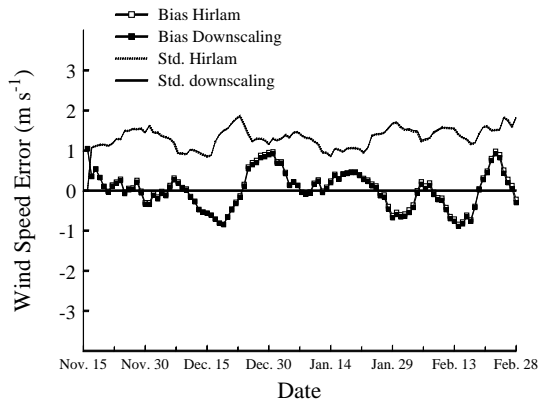
Figure 5.11: Mean and standard deviation of the wind speed error of the +3-hour forecast of the NWP-model and the downscaling method in the winter period October 2003–March 2004 and the summer period April 2004–August 2004.



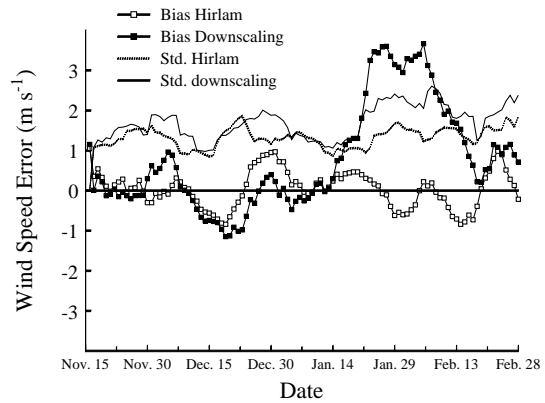
(a) Hansweert.



(b) Amsterdam Airport Schiphol.



(c) Vlake van de Raan.



(d) Non-neutral downscaling method at Vlake van de Raan.

Figure 5.12: Running mean and standard deviation (7-day averaging period) of the wind speed error of the +3-hour forecast of the HIRLAM model and the downscaling method in the period November 2001–February 2002.

produced by Hirlam. The mean error in the modeled local wind speed is in absolute value less than  $0.5 \text{ m s}^{-1}$ , about 5–10% of the measured wind speeds, for most wind directions. For open-sea locations the 2L-model gives similar performance as Hirlam. The standard deviation of the error is only slightly reduced.

- The 2L-model gives an improved performance during neutral, unstable and stable atmospheric conditions. Errors due to not accounting for atmospheric stability in the 2L-model are counterbalanced by using an upward and subsequent downward transformation.
- A non-neutral implementation of the 2L-model suffers from stability correction problems that arise during stable stratification.
- Local and regional, wind direction dependent, roughness lengths can be derived from a land-use dataset by averaging surface roughness over the upstream area.
- The local roughness lengths compare well to those derived from gustiness analysis. This comparison reveals that the footprint length scale for the local roughness is about 0.6 km, which also sets the lower limit for the spatial resolution at which the downscaling method can be applied.
- The 2L-model is well capable of modeling the development of the wind speed after roughness transitions and gives similar results as internal boundary-layer models. The comparison confirms that the footprint length scale for the local roughness must be close to 0.6 km, and that the footprint length scale for the regional roughness is about 3 km.
- Inaccuracies in the land-use map may lead to biased downscaling results.

## Acknowledgments

The presented downscaling method has been developed on the authority of the *Rijksdienst IJsselmeergebied*. Part of the research presented in this paper has been carried out within the framework of the projects Hydra and Nautilus, both supported by the Dutch National Water Board *Rijkswaterstaat*. The Hydra-project is supported by the *National Institute for Coastal and Marine Management* (RIKZ) and the *Institute for Inland Water Management and Waste Water Treatment* (RIZA). Nautilus is supported by RIKZ.

The authors are grateful for the support and interest they received from the user group representatives of the Netherlands Ministry of Transport, Public works and Water management. Iwan Holleman and Vladimir Makin from the Royal Netherlands Meteorological Institute, and Bert Holtslag from Wageningen University and Research Centre, are acknowledged for commenting on the first draft of this paper. Jan-Rolf Hendriks from the Tidal Water Division in Zeeland is thanked for providing the wind observation data from the ZeGe measurement network.

# Chapter 6

## Summary and Outlook

### 6.1 Summary

This thesis deals with the relation between wind, momentum flux, roughness and land-use. The relation between wind, momentum flux and roughness for homogeneous surfaces and constant flux layers has been well established in the Monin-Obukhov (MO) similarity theory in the early '70s (Businger and Yaglom, 1971; Obukhov, 1971). Over non-homogeneous terrain this relation is still a subject of study today (Philip, 1997; De Jong et al., 1999; Mahrt et al., 2001; Baldauf and Fiedler, 2003; Kljun et al., 2004; Dellwik and Jensen, 2005). Key questions of this thesis are: “how is the roughness related to land-use?”, “how are wind and friction related to the upstream land-use and roughness?”, and “is MO-theory still useful over non-homogeneous terrain?”.

A measurement campaign was conducted at Cabauw in 1996 to measure momentum fluxes at elevated levels. At Cabauw the Royal Netherlands Meteorological Institute (KNMI) operates a 213-m high meteorological tower (Monna and Van der Vliet, 1987; Van Ulden and Wieringa, 1996). Routine measurements are taken of the wind, temperature, and moisture profiles, as well as all kinds of surface fluxes. The K-Gill Propeller Vane (k-vane) was used as flux measuring device. Chapter 2 presents the results of an extensive evaluation of the k-vane that was conducted before the instruments were installed at Cabauw. The results of this campaign have been analyzed and are presented in chapter 3.

The dynamic properties of the k-vane have been assessed from perturbation theory, wind tunnel and field comparison experiments (**chapter 2**). From the field experiment it was concluded that k-vane measurements of average wind speed and direction are accurate except for very low wind speeds. Overspeeding or artificial vertical wind speed will generally be very small. Overspeeding could be significant in conditions of very high instability. However, these occasions usually are accompanied by very low wind speeds. Then other measuring errors will mask any overspeeding. From the perturbation theory it follows that the k-vane is a first-order sensor. This is confirmed by the field comparison experiment. The only relevant instrument parameter for measured variances and fluxes is the propeller response length at 45° angle of attack ( $D_{45^\circ}$ , 2.9 m for the 35301 model). This parameter can best be determined from a field comparison experiment, not from wind tunnel tests. Wind tunnel tests show much scatter, and the resulting parameters do not correspond very well to those from the field comparison experiment. When used above 20 m height, however, the differences found in  $D_{45^\circ}$  become insignificant. Transfer functions of the (co-)variances can be described by the regular first-order or second order equation. Standard

spectra as well as spectra measured by the k-vane itself can be used to calculate correction coefficients. In very stable conditions the corrections may become large, increasing scatter in the corrected results. On average both methods yield fluxes and variances that are correct within 10%. During the measurement campaign the k-vanes proved extremely vulnerable to atmospheric electricity and contamination of the bearings supporting the propellers. This resulted in a very low data coverage.

The dataset was analyzed by using various methods to estimate the roughness length from the wind speed and flux measurements (**chapter 3**). The observed differences are explained by considering the source area of the meteorological parameters. Also the flux-profile relationships are tested in conditions of strong flux divergence due to entrainment using both surface layer and local scaling.

The surface roughness at Cabauw is not uniform. A clear rough-to-smooth transition is found in the wind speed profiles at Cabauw. The internal boundary layer reaches the lowest k-vane (20-m height) only in south-west direction where the obstacle-free fetch is about 2 km. The internal boundary layer is also reflected in the roughness lengths derived from the wind speed profiles. The lower part of the profile ( $< 40$  m) is not in equilibrium with the surface roughness and no reliable roughness analysis can be derived from it. The upper part of the profile can be linked to a large-scale roughness length.

Roughness lengths derived from the standard deviation of horizontal wind speed fluctuation and gustiness have large footprints and therefore represent a large-scale roughness. The drag coefficient is more locally determined but still represents a large-scale roughness length when it is measured above the local internal boundary layer.

Except for unstable cases the momentum flux in our data selection shows significant divergence. The heat flux divergence is even more pronounced. Our data set comprises many cases where the measurements are done above the surface layer. In addition, in unstable conditions the entrainment rate can be expected to be large. This is due to our data selection procedure which is in favor of conditions with developing boundary-layers in the morning hours with significant shear (Pino et al., 2003). It is reconfirmed that in stable boundary layers the regular flux-profile relationships are valid provided that local scaling is used. Also in unstable conditions it appears that scaling of the profiles with local fluxes works well, even in directions where the upstream terrain causes strong disturbances of the boundary layer.

In **chapter 4** two gustiness models are evaluated. These gustiness models are used to correct historical wind speed records for the influences of local and temporal roughness variations (exposure correction). The model by Wieringa (1976) has been in use for many years at KNMI. This model was suitable for analogue recorders and was tuned for observation periods of 10-min or 1 hour only. To comply with modern digital recording techniques the model by Beljaars (1987a) is suggested to replace Wieringa's model. Beljaars's model can be used for various kinds of measuring chains, filters, and observations periods.

The exposure correction factors are usually in the range 0.9–1.2. With both Wieringa's and Beljaars's gustiness model the exposure correction can be computed with an accuracy of about 5%. For observation periods of one hour, Beljaars's model gives exposure corrections that are 0–10% smaller than those from Wieringa's model, depending on surface roughness. For shorter observation periods the difference is larger. For 10-min periods for example, Beljaars's exposure corrections are 3 to 10% smaller. In view of other uncertainties, the influence of atmospheric stability on the ratio  $\sigma_u/u_*$  and the wind speed profile

and the assumed blending height, the difference between the two gustiness models is small for observing periods of one hour.

The models are also compared using field data. At an airport station an old, slow wind speed recorder was replaced by a faster recorder. This resulted in an abrupt increase in the measured gustiness. This should not lead to a change in estimated roughness or exposure correction if the gustiness models are correct. However, in both models a jump in roughness length remains corresponding to a exposure correction change of 4%.

Roughness lengths from Beljaars's model have been used to extrapolate the wind speed profile from 10 m height to higher levels at Cabauw. These estimated profiles were compared with observations from the tower. Gustiness analysis was applied to two different wind speed records to yield the roughness length. Beljaars's model performed satisfactorily: differences less than 5% were found when estimating the wind speed at 40 and 80 m height from the wind speed at 10 m height.

In **chapter 5** a physical downscaling method is presented to increase the local accuracy of weather model forecasts. The use of uniform, grid-box averaged, roughness information in numerical weather prediction (NWP) models, to describe the local wind flow, leads to large errors in the representation of the wind in certain areas of the Netherlands. This is particularly noticeable in the coastal zone and near built-up areas. In a stably stratified atmosphere onshore surface winds from the NWP-model HIRLAM are sometimes underestimated by as much as  $3 \text{ m s}^{-1}$  in the Zeeland estuaries, which is as much as 25–30% of the measured wind speeds.

The downscaling method includes a simple two-layer model (2L-model) of the atmospheric boundary layer, used in combination with a high-resolution roughness map. The 2L-model is used to post-process direct NWP-model output. The 2L-model comprises a surface layer and an Ekman-layer. In the surface layer vertical wind speed transformations are done using the logarithmic wind speed profile. In the Ekman-layer geostrophic resistance laws are applied. The roughness map is derived from a land-use map and a simple footprint model. The roughness lengths are wind direction dependent and the footprint area of the Ekman-layer extends farther than that of the surface layer.

The NWP-model wind and the downscaled wind are evaluated in coastal zone areas, in estuaries, and at an airport in the Netherlands. The 2L-model significantly reduces the mean error in the surface winds that are produced by HIRLAM. The mean error in the modeled local wind speed is in absolute value less than  $0.5 \text{ m s}^{-1}$ , about 5–10% of the measured wind speeds, for most wind directions. The standard deviation of the error is only slightly reduced. For open-sea locations the 2L-model gives similar performance as HIRLAM. This shows that over water the same roughness is used as in HIRLAM. The 2L-model gives an improved performance during neutral, unstable and stable atmospheric conditions. Errors due to not accounting for atmospheric stability in the 2L-model are counterbalanced by using an upward and subsequent downward transformation.

The local roughness lengths compare well to those derived from gustiness analysis. This comparison reveals that the footprint length scale for the local roughness is about 0.6 km. Consequently, this length scale is the lower limit for the spatial resolution at which the downscaling method can be applied. Application at a finer resolution will not add any detail to the wind field.

The quality of the downscaling results depend strongly on the quality of the land-use map and the roughness map. The regional roughness of Amsterdam Airport Schiphol proved to be unusable due to inadequacies of the land-use map. In general the airports

in the Netherlands are known for being poorly classified. Moreover, airport areas are subjected to frequent changes which cause changes in the local roughness lengths.

## 6.2 Outlook

### 6.2.1 Application limits of the roughness length concept

In this thesis various methods are evaluated to relate the wind speed profile to the local roughness and vice versa. Information on the local roughness, extracted from gustiness analysis, is used to improve the interpretation of wind speed measurements. Information on land-use can be used to estimate the roughness and to improve estimates of the local wind speed. The connection between roughness and local wind speed is embedded in the Monin-Obukhov similarity and the concept of the roughness length. The application of this concept has limits both in vertical and horizontal scale. In many areas the friction of the surface is for a substantial portion caused by form drag on vegetation and buildings (Beljaars, 1982). At the height where the flow is influenced by individual obstacles the roughness sub-layer is formed. The application of MO-theory is restricted to heights above the roughness sub-layer. This implies that there is a lower limit on the footprint areas as well. This sets restrictions to the heights and the scale of the footprint areas where the downscaling method can be applied. Wind measurements taken in the roughness sub-layer or in the wake of obstacles will give very high gust factors. However, these can not be related to the upstream roughness length in this case. So, it also sets restrictions to the interpretation of measured wind speed.

The footprint length scale for the local roughness (0.6 km) has been determined by comparison with gustiness measurements mostly done at 10-m height. These scales are appropriate for the areas where most measuring stations of KNMI are located. For other areas, however, they may not be applicable. As long as the resolution of operational NWP-models is much larger than these scales the downscaling method presented here will be useful. However, when the resolution of NWP-models becomes comparable or smaller than these scales an entirely different approach to roughness will be necessary. Then it becomes important that momentum is extracted from the flow not only the surface, but also at the height of the obstacles. Then also the flow in the lee of obstacles need to be modeled. Models capable of describing this process are called drag partitioning models (Raupach, 1994). Although early attempts looked promising (Verkaik, 1999), the land-use data set used here (LGN3+) is not suitable for drag partitioning calculations. Other remote sensing data sources have already been explored for their ability to do drag calculations and this may lead to operational applications in due time (De Jong et al., 1999; De Vries, 1999).

### 6.2.2 Wind climate assessment

In the wind climate research at KNMI the measured wind speed has often been interpreted in terms of potential wind (Wieringa, 1986). The potential wind speed is computed from the measured wind speed and a exposure correction factor. The correction for site exposure is based on a strongly simplified physical model of the ABL. The gustiness model to determine the roughness length may have changed, the physical concept to compute the exposure corrections itself has not. This is important to climate research as it requires long homogeneous times series.

The most sophisticated way to interpret meteorological measurements is by means of a re-analysis joining all observations in a coherent physical model. For the re-analysis of long time-series one has to settle for coarse resolution models mainly because of limited computational resources. For the interpretation or estimation of the surface wind speed it will still be essential to apply some boundary layer model to include the local effects of roughness. An additional problem is that re-analysis data do not always provide the long-term homogeneous data sets climate researchers are looking for (Smits et al., 2005).

Climate models may solve the problem of temporal inhomogeneity, although they have the same problem with local representativity. Moreover, risk assessments of national governments require ground-truth verification using measured wind speed. So future wind climate research will persistently need high-quality surface wind speed observations. This includes uniform instrumentation, correction for exposure and data processing. To be able to distinguish trends from shifts in wind climate this needs to be done on an international scale. At the moment there is little correspondence in measuring processes between different countries. Besides this the availability of data is a problem. Freely available datasets like Hydra<sup>1</sup> are rare. These aspects make international wind climate assessments such as the European wind atlas (Troen and Petersen, 1989) an arduous task. This atlas, compiled for wind energy potential mapping, is based on (only) 15 years of data and focuses on averages only. Such an update is required for instance in the determination of European standards for wind load on buildings.

---

<sup>1</sup>[www.knmi.nl/samenw/hydra](http://www.knmi.nl/samenw/hydra)



# Appendix A

## Propeller Dynamics

The k-vane is provided with four-bladed Gill propellers (Gill, 1975). The propellers are helicoidally shaped, that is the angle between the blade chords and the propeller plane is

$$\alpha_b = \arctan(\gamma_R R/r), \quad (\text{A.1})$$

where  $\gamma_R$  is the pitch factor,  $R$  is the radius of the propeller, and  $r$  is the distance to the propeller axis (Busch et al., 1980). In absence of drag and friction, the ratio of the wind speed to the orbital speed of the propeller tips  $U/\omega R$  equals  $\gamma_R$ . In this case the angle of attack of the relative wind on the propeller blade will be zero. Then the pitch, the length of the column of air that has passed the propeller after one revolution, equals  $2\pi\gamma_R R$ . In practice  $\omega R$  will be less than  $U/\gamma_R$  by a factor  $k$ . Inclusion of a correction ( $\Delta u_f$ ) for wind speed independent friction results in the calibration equation for the propeller

$$U = \gamma_R k R \omega + \Delta u_f. \quad (\text{A.2})$$

Note that in this equation, equal to Eq. 43 from Busch et al. (1980),  $k$  will be *larger* than 1 in order to reduce  $\omega$  at given wind speed  $U$ . Usually  $k$  is very close to unity (within 1%) and  $\Delta u_f$  is very small (less than  $0.1 \text{ m s}^{-1}$ ). The correction  $\Delta u_f$  should not be confused with the starting or threshold wind speed  $U_{\text{thr}}$ . The former is an offset to be determined from regression of the calibration curve; the latter is the minimum wind speed required to start the propeller from rest. Usually  $U_{\text{thr}}$  is larger than  $\Delta u_f$ .

When inclined to the wind direction, the propeller response is less than the wind speed component parallel to the propeller axis since propellers exhibit imperfect cosine response (Drinkrow, 1972; Hicks, 1972; Horst, 1973). The actual angular response can be written as

$$C(\Psi) \cos \Psi = (\gamma_R k R \omega + \Delta u_f) / U. \quad (\text{A.3})$$

To correct propeller response for imperfect cosine response,  $C(\Psi)$  has to be measured in a wind tunnel. For the propellers used in this experiment (no. 08254,  $20 \times 30 \text{ cm}$ ),  $C(\Psi)$  is in close agreement with:

$$C(\Psi) = 1 - 0.3 \sin^2(\Psi) + 0.02 \sin(6\Psi), \quad (\text{A.4})$$

taken from Bottema (1995). When a propeller mounted on a vane is placed in a turbulent wind field, it will generally not be aligned perfectly into the instantaneous wind direction. Since usually  $C(\Psi) \leq 1$  for propellers, its response will be reduced due to lateral and vertical wind fluctuations, even though the total wind vector is larger. The corresponding errors were called the  $v$ - and  $w$ -error by MacCready (1966).

The propeller response to a step change in wind speed from  $U_0$  to  $U_\infty$  can be described by a first-order differential equation (MacCready and Jex, 1964)

$$\partial U_{prop}/\partial t = (U_\infty - U_{prop}(t)) / \tau, \quad \tau = D/U_\infty. \quad (\text{A.5})$$

The corresponding transfer function for wind speed variance is given by

$$T_u = [1 + \tau^2 \omega^2]^{-1}. \quad (\text{A.6})$$

Here  $D$  is called the distance constant because it is assumed to be independent of wind speed. Since  $\tau$  is smaller for larger wind speeds, the propeller responds faster to increasing wind speed and slower to decreasing wind speed. Placing the propeller in a turbulent wind field this will cause the propeller to overspeed. The magnitude of the overspeeding will increase with  $D$ . This feature is similar to cup anemometer overspeeding and has been discussed in detail by Busch and Kristensen (1976). MacCready (1966) called this the  $u$ -error of a propeller-anemometer. Here  $D = U_\infty \tau$  increases slightly as the angle  $\Psi$  between wind direction and propeller axis increases. Note that this is only true when  $U$  is equal to the total wind, not to the component parallel to the propeller axis [compare Busch et al. (1980) and Bottema (1995)].

For the propeller blades to act as airfoils, the angle of attack of the relative wind should not exceed  $15^\circ$ . This restriction is expressed by the following relation:

$$\omega_{(\min)}^{\max} / \omega_0 = R\gamma_R / r \tan(\alpha_b \mp 15^\circ), \quad (\text{A.7})$$

where  $\omega_0$  is the equilibrium angular velocity of the propeller. For the propellers used with the k-vane ( $R\gamma_R = 0.3/2\pi$  m),  $\omega_{\min}/\omega_0 = 0.6$ , and  $\omega_{\max}/\omega_0 = 1.7$ . This means that when step-up responses are used to determine  $D$ , only the part after 60% adaption, the tail, should be used. Note from Eq. A.7 that if  $\omega \neq \omega_0$ , the angle of attack is a function of  $r$ .

# Appendix B

## Vane Dynamics

The vane is often assumed to be a damped harmonic oscillator (Busch et al., 1980; Wieringa, 1967). This assumption is only valid if wind torque  $M$  on the vane increases linearly with attack angle  $\beta$ :  $M = N\beta$ . In absence of friction, the vane equation can be written as

$$-J\frac{\partial^2\beta}{\partial t^2} = N\beta + \left(\frac{r_v N}{U}\right)\frac{\partial\beta}{\partial t}. \quad (\text{B.1})$$

Here  $J$  is the moment of inertia of the vane and  $r_v$  the distance from the aerodynamic center of the vane blade to the pivot of the vane. The term in parenthesis in Eq. B.1 is the aerodynamic damping. Any friction that is proportional to  $U^{-1}\partial\beta/\partial t$  can simply be added to the aerodynamic damping (Wieringa, 1967). The solution to Eq. B.1 for a subcritically damped vane ( $\zeta < 1$ ) is

$$\beta = \beta_0 \exp(-\gamma t - i\omega t), \quad (\text{B.2})$$

where  $\gamma = \zeta\omega_0$ ,  $\omega_0 = (N/J)^{1/2}$ ,  $\zeta = r_v\omega_0/2U$ ,  $\omega^2 = \omega_0^2(1 - \zeta^2)$ , and  $\beta_0 = \beta(t_0)$ . The equilibrium value of  $\beta$  is 0,  $\lambda_n = 2\pi U/\omega_0$  is the natural wavelength, and  $\zeta$  is the damping ratio. Friction that is not proportional to  $U^{-1}\partial\beta/\partial t$  will cause  $\zeta$  to be a function of  $U$  (Busch et al., 1980). If  $M$  is not linearly proportional to  $\beta$  the zeroth and first derivative of  $\beta$  mix up and a nonlinear differential equation results. The transfer function for wind direction variance is given by

$$T_v = \left[ (1 - \omega^2/\omega_0^2)^2 + (2\zeta\omega/\omega_0)^2 \right]^{-1}. \quad (\text{B.3})$$

So the measured wind direction variance and the covariances between real and measured wind direction are given by

$$\sigma_\beta^2 = \overline{(\beta')^2} = (\sigma_v/U)^2 \int_0^\infty T_v S_v(\omega) d\omega, \quad (\text{B.4})$$

$$\overline{\beta'\phi'} = (\sigma_v/U)^2 \int_0^\infty (1 - \omega^2/\omega_0^2) T_v S_v(\omega) d\omega. \quad (\text{B.5})$$

A subcritically damped vane overshoots. The ratio of two successive overshoots equals

$$h = \beta_i/\beta_{i-1} = \exp\left[-\pi\zeta/(1 - \zeta^2)^{1/2}\right]. \quad (\text{B.6})$$

Experimentally  $\omega$  and  $\gamma$  or  $\zeta$  can be found by fitting Eq. B.2 to the measured response or by measuring successive overshoots and the time between them.

Vane parameters  $\lambda_n$  and  $\zeta$  can also be calculated from the dimensions and weight of the vane (Wieringa, 1967):

$$\lambda_n = 2\pi (JU^2/N)^{1/2}, \quad \zeta = \pi r_v/\lambda_n. \quad (\text{B.7})$$

Here  $N$  can be estimated from the area of the vane blade  $S$ , the torque parameter  $a_v$ , and  $r_v$

$$N/U^2 = r_v F_v / \beta U^2 = \rho a_v S / 2,$$

where  $F_v$  is the force on the vane blade. The torque parameter is given by

$$a_v = c_v / \beta = c_{v_0} A / \beta (AE + 2), \quad A = b^2 / S,$$

where  $b$  is the span of the vane blade,  $A$  is the aspect ratio and  $c_{v_0}$  is the lift force coefficient for infinite aspect ratio. Here  $E$  is the edge correction and equals the ratio of the semiperimeter to the vane span. When infinite aspect ratio is assumed,  $a_v = 2\pi$ .

# Appendix C

## K-vane measurements at Cabauw

### C.1 Experimental Setup

The Cabauw tower is 213 m high and has booms at intervals of 20 m. The direction of the booms are  $10^\circ$ ,  $130^\circ$  and  $250^\circ$ . At the end of the booms two lateral extensions on either side of the boom carry three plugs, on which instruments can be mounted. At 20, 100 and 180 m height k-vanes have been installed at the far right plug of the north and the far left plug of the south-west pointing booms. The k-vanes have been mounted on the standard KNMI plug. The plug has 9 pines that are all necessary for the k-vane: two for power supply ( $\pm 15$  V) and the seven others for ground, bottom, top, differential ( $= \textit{bottom} - \textit{top}$ ), azimuth, temperature and level signal.

In the k-vane's extension tube the electronics of the thermocouple and the level sensor are stored. A voltage signal for the thermocouple is produced by an cold weld compensation chip. The propeller's photo chopper circuits generate voltage pulses (20 per revolution). All these signals are lead from the k-vane's axle to its base by slip rings contacts. Vane movements are recorded at the k-vane's base by a potentiometer. All signals are converted into current signals in the range of  $\pm 5$  mA (level sensor and differential) and  $-5-20$  mA (other signals). These signals enter the tower where they are amplified and converted into balanced voltages in the range of  $\pm 10$  V. This way the signals are transmitted to the main building at the base of the tower. Here the signals are transformed to regular voltage signals and lead to the AD-converter in the basement of the building.

Since the (small) vertical wind speed is calculated from the difference of two rather large signals (top and bottom), it is sensitive to differences in the transmission of both signals. Therefore the difference of the top and bottom signal has been amplified already at the base of each k-vane and was then transmitted as an additional sixth signal. As long as this amplified difference is not out of range ( $< 2.25$  m s $^{-1}$ ), the calibration procedure calculates the bottom signal from  $S_{\text{bot}} = S_{\text{top}} + S_{\text{diff}}$ .

### C.2 Data Acquisition

Data from the  $6 \times 6 = 36$  signals are recorded by a multiplexer-AD-converter-PC combination. The multiplexer was developed at KNMI. The AD-converter used in this experiment is the Ohmtronics Microstar DAP 1216a. For the PC a regular Tulip 486, 66 MHz was used. The data acquisition software was developed by Dr. Fred Bosveld from KNMI. Sample frequency of the data acquisition program is 16 Hz. Calibration, includ-

ing the iterative scheme for cosine response correction, is done in real time (Ataktürk and Katsaros, 1989; Verkaik, 1998). Every wind speed sample is decomposed in eastward, northward and vertical components before averaging. Every 10 min all averages and (co-)variances are stored on one of the floppy discs. Every change made in the calibration or status of the k-vanes or interruptions of the program is reported automatically in a log-file. The data- and log-file together require less than 1.4 Mbyte per ten days.

Calibrated records of  $U$ ,  $V$ ,  $W$  and  $T$  are also stored in files on a virtual disc. Every 30 min spectra were calculated from these records. The (co-)spectra are stored in a matrix of 20 frequency bands, together with preprocessing results on the hard disc. The spectra and preprocessing results require less than 6 Mbyte per week. Preprocessing includes rotation of the data so that  $\bar{V} = 0$ . In case spectra are calculated over segments of  $2^{13}$  samples (8.5 min) the required computing time for all k-vanes is about 4 min. Since the Microstar DAP 1216a has its own CPU and memory, measurements can continue while the main program is calculating spectra. First every 30 min spectra were computed over segments of  $2^{13}$  samples, but later during the campaign the computation of spectra was done every 20 min in one segment of  $2^{14}$  samples (17 min.). This was done to allow the determination of low frequency spectra.

In case raw data are stored, the data-acquisition program outputs about 8 Mbyte per hour. Because of limited data storage capacity only a few raw data runs have been stored. These runs have a length of only 3–4 days.

## C.3 Flow Distortion

### C.3.1 Potential Flow Calculations

The presence of the tower disturbs the flow field in its vicinity. At the location of the k-vanes flow distortion is caused by the main tower itself (2-m diameter cylinder), by the booms (9.4 m long with open lattice structure), by the side-arms (1.4 m long with 0.06-m diameter tubing), and by the instruments and their housing. Below 40 m measurements may also be disturbed by the 3.75-m high, 17-m diameter building at the foot of the tower.

Wessels (1983) applied Wucknitz's (1980) potential flow model of a cylinder with a wake to the Cabauw tower. He found that the presence of the main tower will reduce the wind at the end of the booms with 3.7% when the boom points into the mean wind direction.

When the boom is at an angle of  $95^\circ$  with the mean wind direction the error in the total wind speed vanishes, and at  $120^\circ$  there is a 2.4% increase. The wind direction change is  $2^\circ$  at maximum ( $80^\circ$ ). Wessels did not compute the effect of flow distortion on second order moments. It is possible though to calculate correction coefficients using Wyngaard's (1981b) application of Wucknitz's model. From Wyngaard's analysis an acceleration at  $120^\circ$  of 1.9% is found. Assuming  $\sigma_u = \sigma_v$ , and  $\overline{v'w'} = 0$ , it follows that the distortion of  $\sigma_u$  is equal to that of  $U$  ( $u$  is the longitudinal variation), and the distortion of  $\sigma_v$  approximates that of  $-\sigma_u$  (see Figure C.1(a)). No distortion of  $\sigma_w$  by the main tower is expected and the distortion of  $u_*$  will be half that of  $\sigma_u$ .

The equivalent cylinder radius of the booms is 0.09 m. The resulting wind speed error at the k-vane mounting plug will be less than 1% and the wind direction error is less than  $0.5^\circ$  maximum. The effect of the side-arms is expected to be negligible, the distance of the k-vane's bottom propeller to the side-arm being more than 0.5 m and the side-arm radius 0.03 m.

Flow distortion by the k-vane itself can be caused by the propeller housing only. All other members of the k-vane construction are too far away from the propellers to induce significant flow distortion. Disturbances caused by the propeller housing, however, will be incorporated in the propeller's calibration constant and cosine response correction if these are assessed with the propeller mounted on the housing that is also used in the field experiments.

### C.3.2 Experimental Assessment

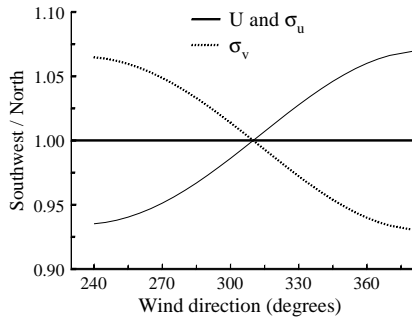
The combined effect of the flow distortion errors can be assessed by comparing the measurements of the two k-vanes at one level. Assuming equal response characteristics for the k-vanes the differences in output between the k-vanes can be contributed to flow distortion by the tower building, the main tower, booms, and side-arms. Differences in output are the largest when one of the k-vanes is in the wake of the tower. The most interesting wind directions for comparison are from  $250^\circ$  to  $10^\circ$ . Because the k-vanes are at the north and south-west booms, flow distortion effects are expected to change symmetrically from  $250^\circ$  to  $10^\circ$ .

The ratio ( $R$ ) of the parameters measure at the north boom (N) to that measured at the south-west (SW) boom have been determined by fitting the equation  $X_{SW} = R \times X_N$  using a  $\chi^2$ -procedure in  $15^\circ$  wide sectors. Here  $X$  stands for the friction velocity ( $u_*$ ) of the velocity variances ( $\sigma_u$ ). Results are plotted in Figs. C.1(b) to C.1(d). The velocity variances  $\sigma_u$  and  $\sigma_v$ , are the longitudinal and lateral wind speed variance, respectively, calculated in a coordinate system where  $\bar{V}$  equals zero.

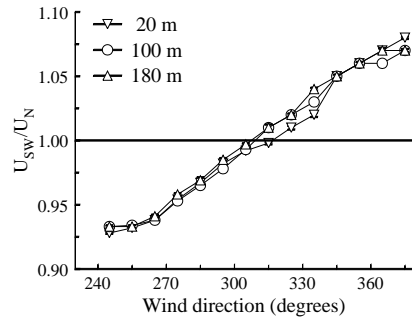
In Figure C.1(b) the results for the points ( $U_N, U_{SW}$ ) are plotted for  $250^\circ < DD < 10^\circ$ . All data included in the basic data selection have been used (see Section 3.4). At  $250^\circ$   $U_N$  is 5–7% higher than  $U_{SW}$ . This corresponds very well to the results of Wessels (1983). At  $310^\circ$  the situation is exactly symmetrical and the difference vanishes. At  $10^\circ$  the difference is reversed. At 20 m the flow distortion does not seem to be different than at the other levels. This indicates that the influence of the tower building on horizontal wind speed is small.

In Figure C.1(e) the average elevation angle difference is plotted (regression on ( $U, W_N - W_{SW}$ ) expressed in degrees). The dependence on wind direction does not reveal any systematic flow distortion by the tower. However, jumps in  $\bar{W}$  as function of time were discovered. In the direction  $310^\circ$ – $320^\circ$  at 100 m height the elevation angle difference is  $-0.62 \pm 0.04^\circ$  in the period till June 1996. After replace of the k-vanes this difference is  $0.30 \pm 0.03^\circ$ . Since the k-vanes were equipped with level sensors misalignment can not be the cause. Probably one of the propellers was not operating very well. During the measurement campaign several times the bearings of the lower propeller needed replacement because of heavy corrosion. This also explains the observed jump  $\bar{W}$  as mention above. When the lower propeller rotates shower negative vertical wind speed will be measured. After the replacement  $\bar{W}$  is closer to zero.

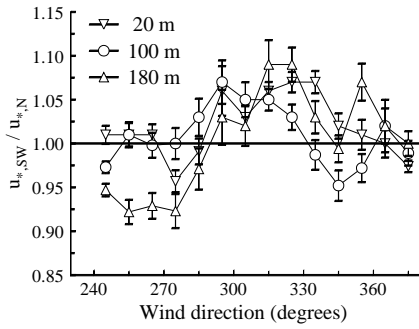
The distortion of  $\sigma_u$  (Figure C.1(f)) is similar to that of  $U$  as was expected, but there is considerably more scatter. The differences in measured  $u_*$  show irregularities (Fig. C.1(c)), although one expects  $u_*$  to be a contamination of the  $\sigma_u$  and  $\sigma_w$  distortion. Summarizing we can conclude that the measuring accuracy of the mean wind speed, the velocity variances is better than 5%, and 10% for friction velocity, which is satisfactory. One must bear in mind, however, that this is only the difference between two k-vanes. Measuring errors that are the same for all k-vanes will not be observed this way. Chapter 2 deals with the k-vane's



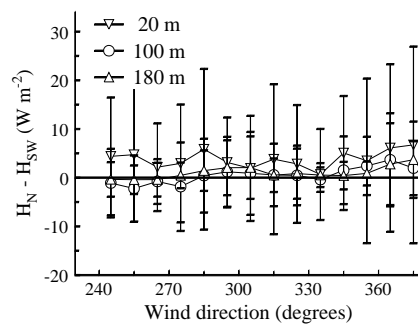
(a) Difference between the two k-vanes at one level due to flow distortion of  $U$ ,  $\sigma_u$ , and  $\sigma_v$  computed from Wyngaard's (1981) theory as function of wind direction.



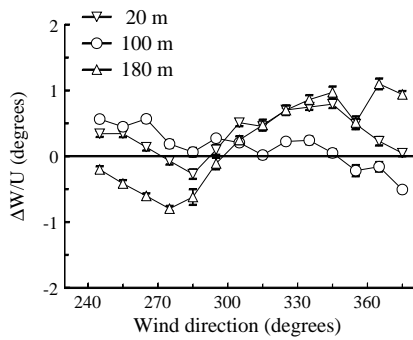
(b) Results of regression on  $(U_N, U_{SW})$  for  $250^\circ < DD < 10^\circ$ .



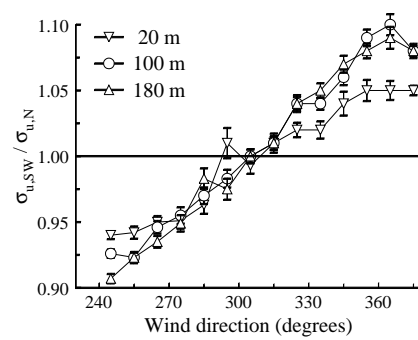
(c) Results of regression on  $(u_{*N}, u_{*SW})$  for  $250^\circ < DD < 10^\circ$ .



(d) Sensible heat flux difference ( $H_N - H_{SW}$ ) for  $250^\circ < DD < 10^\circ$ .



(e) Elevation angle difference  $(W_N - W_{SW})/U$  for  $250^\circ < DD < 10^\circ$ .



(f) As Figure C.1(b) but for  $\sigma_u$

Figure C.1: Experimental assessment of the distortion of the k-vane measurements by the tower.

dynamics in detail. From the close correspondence between the k-vanes we conclude that the results from Chapter 2 are applicable to all k-vanes used in this experiment.

In Figure C.1(d) the average difference in measured sensible heat flux is plotted ( $H_N - H_{SW}$ ). The data set comprises many runs with very low sensible heat fluxes. In these cases the relative difference can be quite large. From Figure C.1(d) it can be seen however, that the absolute difference in  $H$  between two k-vanes at one height is not large. One of the k-vanes at 20 m seems to be a bit biased, resulting in a positive difference of a few  $\text{W m}^{-2}$ . The scatter in the heat flux measurements seems to be quite large. However, the large standard deviation is mainly caused by differences at very high heat flux values. The relative error in these cases is still small.



# References

- Abramowitz, M. and Stegun, I. A., 1965: *Handbook of mathematical functions*. Dover publications, Inc.. New York. 1046 pp.
- Agterberg, R. and Wieringa, J., 1989: Mesoscale terrain roughness mapping of the Netherlands. *Technical Report TR-115*. Royal Netherlands Meteorological Institute. 35 pp.
- Arya, S. P. S., 1977: Suggested revisions to certain boundary layer parameterization schemes used in atmospheric circulation models. *Mon. Wea. Rev.* **105**, 215–227.
- Ataktürk, S. S. and Katsaros, K. B., 1987: Intrinsic frequency spectra of short gravity-capillary waves obtained from temporal measurements of wave height on a lake. *J. Geophys. Res.* **92**, 5131–5141.
- Ataktürk, S. S. and Katsaros, K. B., 1989: The K-Gill: A twin propeller-vane anemometer for measurements of atmospheric turbulence. *J. Atmos. Oceanic Technol.* **6**, 509–515.
- Baldauf, M. and Fiedler, F., 2003: A parameterisation of the effective roughness length over inhomogeneous, flat terrain. *Bound.-Layer Meteor.* **106**, 189–216.
- Barthelmie, R. J., Palutikof, J. P. and Davies, T. D., 1993: Estimation of sector roughness lengths and the effect on prediction of the vertical wind speed profile. *Bound.-Layer Meteor.* **66**, 19–47.
- Beljaars, A. C. M., 1982: The derivation of fluxes from profiles in perturbed areas. *Bound.-Layer Meteor.* **24**, 35–55.
- Beljaars, A. C. M., 1987a: The influence of sampling and filtering on measured wind gusts. *J. Atmos. Oceanic Technol.* **4**, 613–626.
- Beljaars, A. C. M., 1987b: On the memory of wind standard deviation for upstream roughness. *Bound.-Layer Meteor.* **38**, 95–101.
- Beljaars, A. C. M., 1988: The measurement of gustiness at routine wind stations - a review. *WMO-TECO-1988*. Leipzig. pp. 311–316. WMO/TD-No. 222, also Royal Netherlands Meteorological Institute, Sc. Rep., WR 87-11.
- Beljaars, A. C. M. and Bosveld, F. C., 1997: Cabauw data for the validation of land surface parameterization schemes. *J. Climate* **10**, 1172–1193.
- Beljaars, A. C. M. and Holtslag, A. A. M., 1991: Flux parameterization over land surfaces for atmospheric models. *J. Appl. Meteor.* **30**, 327–341.

- Beljaars, A. C. M., Schotanus, P. and Nieuwstadt, F. T. M., 1983: Surface layer similarity under nonuniform fetch conditions. *J. Clim. Appl. Meteor.* **22**, 1800–1810.
- Benschop, H., 1996: Windsnelheidsmetingen op zeestations en kust stations: herleiding waarden windsnelheid naar 10-meter niveau. *Technical Report TR-188*. Royal Netherlands Meteorological Institute. in Dutch, 16 pp.
- Bergström, H., Johansson, P.-E. and Smedman, A.-S., 1988: A study of wind speed modification and internal boundary-layer heights in a coastal region. *Bound.-Layer Meteor.* **42**, 313–335.
- Blackader, A. K. and Tennekes, H., 1968: Asymptotic similarity in neutral barotropic boundary layers. *J. Atmos. Sci.* **25**, 1015–1020.
- Bottema, M., 1995: Calibration study of the K-Gill propeller vane. *Technical Report TR-181*. Royal Netherlands Meteorological Institute. 46 pp.
- Bowen, B. M., 2000: Near-neutral surface layer turbulence at the Boulder atmospheric observatory tower: evidence of increasing vertical turbulence with height. *J. Appl. Meteor.* **39**, 716–724.
- Bradley, E. F., 1968: A micrometeorological study of velocity profiles and surface drag in the region modified by a change in surface roughness. *Quart. J. Roy. Meteor. Soc.* **94**, 361–379.
- Brown, R. A., 1982: On two-layer models and the similarity functions for the PBL. *Bound.-Layer Meteor.* **24**, 451–463.
- Busch, N. E., Christensen, O., Kristensen, L., Lading, L. and Larsen, S. E., 1980: Cups, vanes, propellers and laser anemometers. in F. Dobson, L. Hasse and R. Davids (eds), *Air-Sea interaction: Instruments and methods*. Plenum Press. New York. pp. 11–46.
- Busch, N. E. and Kristensen, L., 1976: Cup anemometer overspeeding. *J. Appl. Meteor.* **15**, 1328–1332.
- Businger, J. A. and Yaglom, A. M., 1971: Introduction to Obukhov’s paper ‘Turbulence in an atmosphere with a non-uniform temperature’. *Bound.-Layer Meteor.* **2**, 3–6.
- Charnock, H., 1955: Wind stress on a water surface. *Quart. J. Roy. Meteor. Soc.* **81**, 639.
- Claussen, M., 1990: Area-averaging of surface fluxes in a neutrally stratified, horizontally inhomogeneous atmospheric boundary layer. *Atmos. Environ.* **24A**, 1349–1360.
- De Bruin, H. A. R., Koshiek, W. and Van den Hurk, B. J. J. M., 1993: A verification of some methods to determine the fluxes of momentum, sensible heat, and water vapour using standard deviation and structure parameter of scalar meteorological quantities. *Bound.-Layer Meteor.* **63**, 231–257.
- De Jong, J. J. M., De Vries, A. C. and Klaassen, W., 1999: Influence of obstacles on the aerodynamic roughness of the Netherlands. *Bound.-Layer Meteor.* **91**, 51–64.
- De Rooy, W. C., 1995: Regionalisation of meteorological parameters. *Scientific Report WR95-06*. Royal Netherlands Meteorological Institute. 51 pp.

- De Rooy, W. C. and Kok, K., 2002: On the use of physical and statistical downscaling techniques for NWP model output. *Scientific Report* **WR2002-05**. Royal Netherlands Meteorological Institute. 82 pp.
- De Rooy, W. C. and Kok, K., 2004: A combined physical-statistical approach for the downscaling of model wind speed. *Wea. Forecasting* **19**, 485–495.
- De Vries, A. C., 1999: *Land surface roughness and remote sensing*. PhD thesis. Rijksuniversiteit Groningen, the Netherlands.
- De Wit, A. J. W., Van der Heijden, T. G. C. and Thunnissen, H. A. M., 1999. Vervaardiging en nauwkeurigheid van het LGN3 grondgebruiksbestand. DLO-Staring Centrum, Wageningen. in Dutch, 84 pp.
- Dellwik, E. and Jensen, N. O., 2005: Flux-profile relationships over a fetch limited beech forest. *Bound.-Layer Meteor.* **115**, 179–204.
- Desjardins, R. L., Reid, W. S., Buckley, D. J. and Fagan, W., 1986: Description and performance testing of a low friction, twin-propeller anemometer with a vane. *J. Phys. E: Sci. Instrum.* **19**, 632–637.
- Driedonks, A. G. M. and Tennekes, H., 1984: Entrainment effects in the well-mixed atmospheric boundary layer. *Bound.-Layer Meteor.* **30**, 75–105.
- Drinkrow, R., 1972: A solution to the paired Gill-anemometer response function. *J. Appl. Meteor.* **11**, 76–80.
- Duijm, N. J., 1983: Model voor de stroming in een neutrale oppervlakte laag na een verandering in oppervlakte ruwheid. *Scientific Report* **WR 83-3**. Royal Netherlands Meteorological Institute. in Dutch, 75 pp.
- Dyer, A. J., 1974: A review of flux-profile relationships. *Bound.-Layer Meteor.* **7**, 363–372.
- Fichtl, G. H. and Kumar, P., 1974: The response of a propeller anemometer to turbulent flow with the mean wind direction perpendicular to the axis of rotation. *Bound.-Layer Meteor.* **6**, 363–379.
- Frenzen, P. and Vogel, C. A., 1995a: A further note “On the magnitude and apparent range of variation of the von Karman constant in the atmospheric surface layer”. *Bound.-Layer Meteor.* **75**, 315–317.
- Frenzen, P. and Vogel, C. A., 1995b: On the magnitude and apparent range of variation of the von Karman constant in the atmospheric surface layer. *Bound.-Layer Meteor.* **72**, 371–392.
- Garratt, J. R., 1977: Review of drag coefficients over oceans and continents. *Mon. Wea. Rev.* **105**, 915–929.
- Garratt, J. R., 1990: The internal boundary layer — a review. *Bound.-Layer Meteor.* **50**, 171–203.
- Garratt, J. R., 1992: *The Atmospheric Boundary Layer*. Cambridge University Press. Cambridge. 316 pp.

- Garratt, J. R. and Hicks, B. B., 1990: Micrometeorological and PBL experiments in Australia. *Bound.-Layer Meteor.* **50**, 11–29.
- Gill, G. C., 1975: Development and use of the Gill UVW anemometer. *Bound.-Layer Meteor.* **8**, 475–495.
- Grant, A. L. M., 1991: Surface drag and turbulence over an inhomogeneous land surface. *Bound.-Layer Meteor.* **56**, 309–337.
- Grant, A. L. M. and Mason, P. J., 1990: Observations of the boundary-layer structure over complex terrain. *Quart. J. Roy. Meteor. Soc.* **116**, 159–186.
- Greenway, M. E., 1979: An analytical approach to wind velocity gust factors. *J. Ind. Aerodyn.* **5**, 61–91.
- Grelle, A. and Lindroth, A., 1994: Flow distortion by a Solent sonic anemometer: Wind tunnel calibration and its assessment for flux measurements over forest and field. *J. Atmos. Oceanic Technol.* **11**, 1529–1542.
- Hicks, B. B., 1972: Propeller anemometers as sensors of atmospheric turbulence. *Bound.-Layer Meteor.* **3**, 214–228.
- Højstrup, J., 1981: A simple model for the adjustment of velocity spectra in unstable conditions downstream of an abrupt change in roughness and heat flux. *Bound.-Layer Meteor.* **21**, 341–356.
- Højstrup, J., 1982: Velocity spectra in the unstable planetary boundary layer. *J. Atmos. Sci.* **39**, 2239–2248.
- Holtslag, A. A. M., 1984: Estimation of diabatic wind speed profiles from near-surface weather observations. *Bound.-Layer Meteor.* **29**, 225–250.
- Holtslag, A. A. M. and De Bruin, H. A. R., 1988: Applied modelling of the nighttime surface energy balance over land. *J. Appl. Meteor.* **27**, 689–704.
- Holtslag, A. A. M. and Nieuwstadt, F. T. M., 1986: Scaling the atmospheric boundary layer. *Bound.-Layer Meteor.* **36**, 201–209.
- Horst, T. W., 1973: Corrections for response errors in a three-component propeller anemometer. *J. Appl. Meteor.* **12**, 716–725.
- Horst, T. W., 1999: The footprint for estimation of atmosphere-surface exchange fluxes by profile techniques. *Bound.-Layer Meteor.* **90**, 171–188.
- Horst, T. W. and Weil, J. C., 1992: Footprint estimation for scalar flux measurements in the atmospheric surface layer. *Bound.-Layer Meteor.* **59**, 279–296.
- Horst, T. W. and Weil, J. C., 1994: How far is far enough?: The fetch requirements for micrometeorological measurements of surface fluxes. *J. Atmos. Oceanic Technol.* **11**, 1018–1025.
- Hutjes, R. W. A., 1996: *Transformation of near-surface meteorology in a small-scale landscape with forests and arable land*. PhD thesis. Rijksuniversiteit Groningen, the Netherlands.

- Jackson, P. S. and Hunt, J. C. R., 1975: Turbulent wind flow over a low hill. *Quart. J. Roy. Meteor. Soc.* **101**, 929–955.
- Jacobs, A. F. G., 1984: The flow around a thin closed fence. *Bound.-Layer Meteor.* **28**, 317–328.
- Jensen, N. O., 1978: Change of surface roughness and the planetary boundary layer. *Quart. J. Roy. Meteor. Soc.* **104**, 351–356.
- Kaimal, J. C., 1977: Horizontal velocity spectra in an unstable surface layer. *J. Atmos. Sci.* **35**, 18–24.
- Kaimal, J. C. and Finnigan, J. J., 1994: *Atmospheric Boundary Layer Flows - Their Structure and Measurement*. Cambridge University Press. New York. 289 pp.
- Kaimal, J. C. and Wyngaard, J. C., 1990: The Kansas and Minnesota experiments. *Bound.-Layer Meteor.* **50**, 31–47.
- Kaimal, J. C., Wyngaard, J. C., Izumi, Y. and Coté, O. R., 1972: Spectra characteristics of surface-layer turbulence. *Quart. J. Roy. Meteor. Soc.* **98**, 563–589.
- Katsaros, K. B., Donelan, M. A. and Drennan, W. M., 1993: Flux measurements from a SWATH ship in SWADE. *J. Marine Sys.* **4**, 117–132.
- Katsaros, K. B., Smith, S. D. and Oost, W. A., 1987: HEXOS—Humidity exchange over sea. A program for research on water-vapor and droplet fluxes from sea to air at moderate to high wind speeds. *Bull. Amer. Meteor. Soc.* **69**, 466–476.
- Kljun, N., Calanca, P., Rotach, M. W. and Schmid, H. P., 2004: A simple parameterisation for flux footprint predictions. *Bound.-Layer Meteor.* **112**, 503–523.
- Korrell, A., Panofsky, H. A. and Rossi, R. J., 1982: Wind profiles at the Boulder tower. *Bound.-Layer Meteor.* **22**, 295–312.
- Kristensen, L., Casanova, M., Courtney, M. S. and Troen, I., 1991: In search of a gust definition. *Bound.-Layer Meteor.* **55**, 91–107.
- Kudryavtsev, V. N., Makin, V. K., Klein Tank, A. M. G. and Verkaik, J. W., 2000: A model of wind transformation over water–land surfaces. *Scientific Report WR-2000-01*. Royal Netherlands Meteorological Institute. 30 pp.
- Kustas, W. P. and Brutsaert, W., 1986: Wind profile constants in a neutral atmospheric boundary layer over complex terrain. *Bound.-Layer Meteor.* **34**, 35–54.
- Large, W. G. and Pond, S., 1981: Open ocean momentum flux measurements in moderate to strong winds. *J. Phys. Oceanogr.* **11**, 324–336.
- Large, W. G. and Pond, S., 1982: Sensible and latent heat flux measurements over the ocean. *J. Phys. Oceanogr.* **12**, 464–482.
- Lumley, J. L. and Panofsky, H. A., 1964: *The structure of atmospheric turbulence*. Interscience. London. 239 pp.

- Ma, J. and Daggupati, S. M., 1998: Stability dependence of height scales and effective roughness lengths of momentum and heat transfer over roughness changes. *Bound.-Layer Meteor.* **88**, 145–160.
- MacCready, P. B., 1966: Mean wind speed measurements in turbulence. *J. Appl. Meteor.* **5**, 219–225.
- MacCready, P. B. and Jex, H. R., 1964: Response characteristics and meteorological utilization of propeller and vane wind sensors. *J. Appl. Meteor.* **3**, 182–193.
- Mahrt, L., 1996: The bulk aerodynamic formulation over heterogeneous surfaces. *Bound.-Layer Meteor.* **78**, 87–119.
- Mahrt, L., Vickers, D., Jensen, N. O., Jørgensen, H., Pardyjak, E. and Fernando, H., 2001: Determination of the surface drag coefficient. *Bound.-Layer Meteor.* **99**, 249–276.
- Makin, V. K., 2003: Note on a parameterization of the sea drag. *Bound.-Layer Meteor.* **106**, 593–600.
- Makin, V. K., Kudryavtsev, V. N. and Mastenbroek, C., 1995: Drag of the sea surface. *Bound.-Layer Meteor.* **73**, 159–182.
- Mason, P. J., 1988: The formation of areally-averaged roughness lengths. *Quart. J. Roy. Meteor. Soc.* **114**, 399–420.
- Miller, C. A., Cook, N. J. and Barnard, R. H., 1998: Calibration of the exposure of UK anemographs. *J. Wind Eng. Ind. Aerodyn.* **74-76**, 153–161.
- Monna, W. A. A., 1983: De KNMI-windtunnel. *Technical Report TR-32*. Royal Netherlands Meteorological Institute. 34 pp.
- Monna, W. A. A. and Driedonks, A. G. M., 1979: Experimental data on the dynamic properties of several propeller vanes. *J. Appl. Meteor.* **18**, 699–702.
- Monna, W. A. A. and Van der Vliet, J. G., 1987: Facilities for research and weather observations on the 213 m tower at Cabauw and remote locations. *Scientific Report WR 87-5*. Royal Netherlands Meteorological Institute. 27 pp.
- Moore, C. J., 1986: Frequency response corrections for eddy correlation systems. *Bound.-Layer Meteor.* **37**, 17–35.
- Mortensen, N. G. and Højstrup, J., 1995: The Solent sonic — response and associated errors. *Preprints, 9th Symp. on Meteorological Observations and Instrumentation*. Amer. Meteor. Soc., Charlotte, NC. pp. 501–506.
- Nieuwstadt, F. T. M., 1978: The computation of the friction velocity  $u_*$  and the temperature  $T_*$  from temperature and wind velocity profiles by least-square methods. *Bound.-Layer Meteor.* **14**, 235–246.
- Nieuwstadt, F. T. M., 1984: The turbulent structure of the stable, nocturnal boundary layer. *J. Atmos. Sci.* **41**, 2202–2216.

- Obukhov, A. M., 1971: Turbulence in an atmosphere with a non-uniform temperature. *Bound.-Layer Meteor.* **2**, 7–29.
- Oemraw, B., 1984: Beschuttingscorrectie wind. *Technical Report TR-52*. Royal Netherlands Meteorological Institute. in Dutch, 65 pp.
- Olesen, H. R., Larsen, S. E. and Højstrup, J., 1984: Modelling velocity spectra in the lower part of the planetary boundary layer. *Bound.-Layer Meteor.* **29**, 285–312.
- Onvlee, J. R. A., 1993: The performance of dragrelations in the WAQUA storm surge model. *Technical Report TR-149*. Royal Netherlands Meteorological Institute.
- Panofsky, H. A. and Dutton, J. A., 1984: *Atmospheric Turbulence, Models and Methods for Engineering Applications*. Jon Wiley & Sons. New York. 397 pp.
- Panofsky, H. A., Tennekes, H., Lenschow, D. H. and Wyngaard, J. C., 1977: The characteristics of turbulent velocity components in the surface layer under convective conditions. *Bound.-Layer Meteor.* **11**, 355–361.
- Parratt, L. G., 1961: *Probability and experimental errors in science*. Wiley. New York. 255 pp.
- Paulson, C. A., 1970: The mathematical representation of wind speed and temperature profiles in the unstable atmospheric surface layer. *J. Appl. Meteor.* **9**, 857–861.
- Philip, J. R., 1997: Blending and internal boundary-layer heights, and shear stress. *Bound.-Layer Meteor.* **84**, 85–98.
- Pino, D., Vilà-Guerau de Arellano, J. and Duynkerke, P. G., 2003: The contribution of shear to the evolution of a convective boundary layer. *J. Atmos. Sci.* **60**, 1913–1926.
- Pond, S., Large, W. G., Miyake, M. and Burling, R. W., 1979: A Gill propeller-vane anemometer for flux measurements during moderate and strong winds. *Bound.-Layer Meteor.* **16**, 351–364.
- Rao, K. S., Wyngaard, J. C. and Coté, O. R., 1974: The structure of the two-dimensional internal boundary layer over a sudden change of surface roughness. *J. Atmos. Sci.* **31**, 738–746.
- Raupach, M. R., 1994: Simplified expressions for vegetation roughness length and zero-plane displacement as function of canopy height and area index. *Bound.-Layer Meteor.* **71**, 211–216.
- Schmid, H. P., 1994: Source areas for scalars and scalar fluxes. *Bound.-Layer Meteor.* **67**, 293–318.
- Schmid, H. P. and Bünzli, D., 1995: The influence of surface texture on the effective roughness length. *Quart. J. Roy. Meteor. Soc.* **121**, 1–21.
- Schmid, H. P. and Lloyd, C. R., 1999: Spatial representativeness and the location bias of flux footprints over inhomogeneous areas. *Agric. Forest Meteor.* **93**, 195–209.

- Schmid, H. P. and Oke, T. R., 1990: A model to estimate the source area contribution to turbulent exchange in the surface layer over patchy terrain. *Quart. J. Roy. Meteor. Soc.* **116**, 965–988.
- Smits, A., Klein Tank, A. M. G. and Können, G. P., 2005: Trends in storminess over the Netherlands, 1962-2002. *Int. J. Climatol.* **25**, 1331–1344.
- Sorbjan, Z., 1986: On similarity in the atmospheric boundary layer. *Bound.-Layer Meteor.* **34**, 377–397.
- Sozzi, R., Favaron, M. and Georgiadis, T., 1998: Method for estimation of surface roughness and similarity function of wind speed vertical profile. *J. Appl. Meteor.* **37**, 461–469.
- Steenefeld, G.-J., Holtslag, A. A. M. and De Bruin, H. A. R., 2005: Fluxes and gradients in the convective surface layer and the possible role of boundary-layer depth and entrainment flux. *Bound.-Layer Meteor.* **116**, 237 – 252.
- Sud, Y. C., Shukla, J. and Mintz, Y., 1988: Influence of land surface roughness on atmospheric circulation and precipitation: a sensitivity study with a general circulation model. *J. Appl. Meteor.* **27**, 1036–1054.
- Taylor, P. A., 1987: Comments and further analysis on effective roughness lengths for use in numerical models. *Bound.-Layer Meteor.* **39**, 403–418.
- Tennekes, H., 1973: The logarithmic wind profile. *J. Atmos. Sci.* **30**, 234–238.
- Townsend, A. A., 1965: The response of a turbulent boundary layer to abrupt changes in surface conditions. *J. Fluid Mech.* **22**, 799–822.
- Troen, I. and Petersen, E. L., 1989: *European Wind Atlas*. Risø National Laboratory. Roskilde, Denmark. 656 pp.
- Undén, P., Rontu, L., Jarvinen, H., Lynch, P., Calvo, J., Cats, G., Cuxart, J., K. Eerola, Fortelius, C., Garcia-Moya, J. A., Jones, C., Lenderink, G., McDonald, A., McGrath, R., Navascues, B., Nielsen, N. W., Odegaard, V., Rodriguez, E., Rummukainen, M., Room, R., Sattler, K., Savijarvi, H., Sass, B. H., Schreur, B., The, H. and Tijn, S., 2002: Hirlam-5 scientific documentation. *Technical report*. SMHI. 144 pp.
- Van der Vliet, J. G., 1998: Elf jaar Cabauw-metingen. *Technical Report TR-210*. Royal Netherlands Meteorological Institute. in Dutch, 79 pp.
- Van Ulden, A. P., 1978: Simple estimates for vertical diffusion from sources near the ground. *Atmos. Environ.* **12**, 2125–2129.
- Van Ulden, A. P. and Wieringa, J., 1996: Atmospheric boundary layer research at Cabauw. *Bound.-Layer Meteor.* **78**, 39–69.
- Van Wijk, A. J. M., Beljaars, A. C. M., Holtslag, A. A. M. and Turkenburg, W. C., 1990: Diabatic wind speed profiles in coastal regions: comparison of an internal boundary layer (IBL) model with observations. *Bound.-Layer Meteor.* **51**, 49–74.

- Verkaik, J. W., 1997: Wind profiles and momentum fluxes in the lower neutral PBL over flat heterogeneous terrain. *Preprints, 12th Symp. on Boundary Layers and Turbulence*. Vancouver, BC, Canada. pp. 546–547. Amer. Meteorol. Soc.
- Verkaik, J. W., 1998: Evaluation of the K-Gill propeller vane. *J. Atmos. Oceanic Technol.* **15**, 901–915.
- Verkaik, J. W., 1999: Estimation of form drag using satellite data. *Preprints, 13th Symp. on Boundary Layers and Turbulence*. Dallas, TX. pp. 286–287. Amer. Meteorol. Soc.
- Verkaik, J. W., 2000: Evaluation of two gustiness models for exposure correction calculations. *J. Appl. Meteor.* **39**, 1613–1626.
- Verkaik, J. W. and Smits, A., 2001: Interpretation and estimation of the local wind climate. *Proceedings of the 3rd European and African conference on wind engineering*. 2–6 July, 2001, Eindhoven, the Netherlands. pp. 43–56.
- Vickers, D. and Mahrt, L., 1999: Monin-Obukhov similarity theory in the coastal zone. *Preprints, 13th Symp. on Boundary Layers and Turbulence*. Dallas, TX. pp. 407–410. Amer. Meteorol. Soc.
- Vogelezang, D. and Holtslag, A., 1996: Evaluation and model impacts of alternative boundary-layer height formulations. *Bound.-Layer Meteor.* **81**, 245–269.
- Wessels, H. R. A., 1983: Distortion of the wind field by the Cabauw meteorological tower. *Scientific Report WR 83-15*. Royal Netherlands Meteorological Institute. 34 pp.
- Wessels, H. R. A., 1984: Cabauw meteorological data tapes 1973-1984; description of instrumentation and data processing for the continuous measurements. *Scientific Report WR 84-6*. Royal Netherlands Meteorological Institute. 23 pp.
- Wieringa, J., 1967: Evaluation and design of wind vanes. *J. Appl. Meteor.* **6**, 1114–1122.
- Wieringa, J., 1973: Gust factors over open water and built-up country. *Bound.-Layer Meteor.* **3**, 424–441.
- Wieringa, J., 1976: An objective exposure correction method for average wind speeds measured at a sheltered location. *Quart. J. Roy. Meteor. Soc.* **102**, 241–253.
- Wieringa, J., 1977: Wind representativity increase due to an exposure correction, obtainable from past analog station records. *WMO-Rep. No. 480 (Proc. TECIMO Conf.)*. pp. 39–44.
- Wieringa, J., 1980a: Representativeness of wind observations at airports. *Bull. Amer. Meteor. Soc.* **61**, 962–971.
- Wieringa, J., 1980b: A revaluation of the kansas mast influence on measurements of stress and cup anemometer overspeeding. *Bound.-Layer Meteor.* **18**, 411–430.
- Wieringa, J., 1986: Roughness-dependent geographical interpolation of surface wind speed averages. *Quart. J. Roy. Meteor. Soc.* **112**, 867–889.

- Wieringa, J., 1993: Representative roughness parameters for homogeneous terrain. *Bound.-Layer Meteor.* **63**, 323–363.
- Wieringa, J., 1996: Does representative wind information exist?. *J. Wind Eng. Ind. Aerodyn.* **65**, 1–12.
- Wieringa, J. and Rijkoort, P. J., 1983: *Windklimaat van Nederland*. Staatsuitgeverij. Den Haag, the Netherlands. in Dutch, 263 pp.
- Wieringa, J. and Van der Veer, P. J. M., 1976: Nederlandse windstations 1971-1974. *Report V-278*. Royal Netherlands Meteorological Institute. in Dutch, 90 pp.
- Wieringa, J. and Van Lindert, F. X. C. M., 1971: Application limits of double-fin and coupled wind vanes. *J. Appl. Meteor.* **10**, 137–145.
- Wolfson, M. M. and Fujita, T. T., 1989: Correcting wind speed measurements for site obstructions. *J. Atmos. Oceanic Technol.* **6**, 343–352.
- Wucknitz, J., 1980: Flow distortion by supporting structures. in F. Dobson, L. Hasse and R. Davids (eds), *Air-Sea interaction: Instruments and methods*. Plenum Press. New York. pp. 605–626.
- Wyngaard, J. C., 1981a: Cup, propeller, vane, and sonic anemometers in turbulence research. *Annu. Rev. Fluid Mech.* **13**, 399–423.
- Wyngaard, J. C., 1981b: The effects of probe-induced flow distortion on atmospheric turbulence measurements. *J. Appl. Meteor.* **20**, 784–794.
- Wyngaard, J. C., Businger, J. A., Kaimal, J. C. and Larsen, S. E., 1982: Comments on ‘A revaluation of the Kansas mast influence on measurements of stress and cup anemometer overspeeding’. *Bound.-Layer Meteor.* **22**, 245–250.
- Yaglom, A. M., 1977: Comments on wind and temperature flux-profile relationships. *Bound.-Layer Meteor.* **11**, 89–102.
- Yumao, X., Chaofu, Z., Zhongkai, L. and Wei, Z., 1997: Turbulent structure and local similarity in the tower layer over the Nanjing area. *Bound.-Layer Meteor.* **82**, 1–21.
- Zhang, S. F., 1988: *A Critical Evaluation of the von Karman Constant from a New Atmospheric Surface Layer Experiment*. PhD thesis. University of Washington. Available from University Microfilms, 300 North Zeeb Road, Ann Arbor, Michigan 48106, USA”.

# Samenvatting

Dit proefschrift gaat over wind en ruwheid boven land.

Wind kan gegenereerd worden door depressies of door thermische circulaties (zeewind). Nabij het aardoppervlak wordt de wind geremd door de oppervlakteruwheid. De ruwheid en de thermische opbouw van de atmosfeer bepalen de mate waarmee de wind met de hoogte toeneemt. Wanneer er veel wind staat is de ruwheid het meeste van belang.

De invloed van het aardoppervlak kan zich uitstrekken van een hoogte van 50 m in stabiele omstandigheden tot  $\sim 1$  km in onstabiele omstandigheden. Het is belangrijk de wind hier te weten, omdat in deze laag vrijwel alle menselijke activiteiten plaatsvinden. De wind belast constructies, veroorzaakt golven, vervoert gassen en stof, etc. Het is daarom belangrijk voor ingenieurs, de lucht- en scheepsvaart en allerlei buitenactiviteiten om over goede informatie te beschikken van de wind en het windklimaat.

Ruwheid veroorzaakt ook wrijving en daardoor ontstaat weer turbulentie. Deze turbulentie versterkt het transport van en naar het Aardoppervlak van warmte, vocht en wat er maar met de lucht wordt meegevoerd. Hoewel het maar een dunne laag is waarin deze processen plaatsvinden, zijn ze van groot belang voor het weer en klimaat, en de chemie van de atmosfeer.

De relatie tussen wind, ruwheid en wrijving in verschillende stabiliteitsomstandigheden is al in de jaren '70 vast gelegd in de Monin-Obukhov (MO) gelijkvormigheids theorie. Deze theorie is afgeleid voor ruimtelijk homogene oppervlakken en bij constante verticale fluxen van impuls en warmte. Dergelijke omstandigheden zijn echter zeldzaam. Vandaag de dag wordt nog steeds onderzoek gedaan naar de toepassing van MO-theorie in inhomogene omstandigheden. Dit proefschrift is daar een voorbeeld van. De centrale vragen zijn: “hoe kan de ruwheid uit het landgebruik worden afgeleid?”, “hoe zijn de wind en ruwheid gerelateerd aan het bovenwindse landgebruik en ruwheid?”, en “kan MO-theorie nog steeds gebruikt worden in inhomogene omstandigheden?”.

De initiële basis voor dit onderzoek is gelegd in een meetcampagne in 1996 te Cabauw. Op Cabauw doet het KNMI al sinds 1973 onderzoek met behulp van een 213-m hoge mast. Langs deze mast worden windsnelheid, temperatuur en vocht gemeten. Aan het oppervlak worden allerlei (stralings-)fluxen gemeten. Tijdens de meetcampagne zijn de standaard metingen van Cabauw aangevuld met metingen van de wrijving en de warmteflux. Het apparaat wat hiervoor gebruikt is, is de K-vaan.

De K-vaan is uitvoerig getest voordat deze op de mast is geplaatst (hoofdstuk 2). Dat is gedaan door de respons van de k-vaan op een turbulent windveld door te rekenen, met behulp van windtunnel tests en een vergelijkingsexperiment. Hieruit is gebleken dat de meetfouten van de k-vaan voor de gemiddelde wind verwaarloosbaar klein zijn. De dynamische respons van de k-vaan kan beschreven worden met één parameter, namelijk de responslengte van de propellers bij een aanstroomhoek van  $45^\circ$ . De meetfouten in de lon-

gitudinale en verticale variantie en de impulsflux kunnen worden beschreven als was de k-vaan een eenvoudig eerste-orde systeem. Zowel standaard spectra als de spectra door de k-vaan zelf gemeten kunnen worden gebruikt om voor deze fouten te corrigeren. In het laatste geval is geen informatie nodig wat betreft de hoogte en stabiliteit van de atmosferische grenslaag. Wat betreft de meting van de laterale component van de turbulentie kan de k-vaan beschreven worden zal een gedempte harmonische oscillator. De meetfouten in laterale variantie zijn doorgaans echter gering doordat de onderschatting van de hoogfrequente variantie wordt gecompenseerd door de overschatting van de variantie met de natuurlijke golflengte van de k-vaan.

De responslengte en de natuurlijke golflengte zoals die bepaald zijn uit het vergelijkingsexperiment zijn beide kleiner dan de waarden die volgen uit de windtunnelproeven. De verschillen worden echter onbeduidend wanneer de k-vaan boven de 20 m hoogte wordt gebruikt aangezien de meetfouten van de k-vaan dan zeer klein worden. De waarden die afgeleid zijn uit het vergelijkingsexperiment zijn 2.9 m voor de responslengte (propeller model 35301) en 7.8 m voor de natuurlijke golflengte en 0.49 voor de dempingsverhouding. Wanneer de k-vaan boven de 20 m wordt gebruikt is de onderschatting van de impulsflux ten gevolge van de traagheid van het instrument kleiner dan 10%. De k-vaan kan dus goed gebruikt worden voor metingen op hoge masten.

In hoofdstuk 3 worden de resultaten van de meetcampagne besproken.

Tijdens de meetcampagne op de Cabauw mast bleek de k-vaan een zeer gevoelig instrument te zijn. Veelvuldig raakte de elektronica van de propellers beschadigd, waarschijnlijk door atmosferische elektriciteit. De verzamelde dataset vertoont daardoor vele gaten.

De dataset is geanalyseerd door met verschillende technieken de omgevingsruwheid als functie van de windrichting te bepalen en deze te relateren aan het landgebruik waardoor deze wordt veroorzaakt, het brongebied. Ook de relatie tussen de windprofielen en impulsflux is onderzocht.

De omgeving van Cabauw is niet homogeen en dat is goed te zien in de windprofielen. Er is een duidelijke knik te zien van ruw (veraf) naar glad (dichtbij). De hoogte van deze knik bereikt alleen in de zuidwest richting de onderste k-vaan op 20 m hoogte. In die richting is het bovenwindse terrein vrij van obstakels tot op 2 km afstand. Door deze ruwheidsovergang is het niet mogelijk een realistische waarde voor de ruwheid af te leiden uit de windprofielen tot 40 m hoogte. Het profiel daarboven komt meer overeen met de grootschalige ruwheid van de omgeving.

De ruwheid die afgeleid wordt uit de variantie van de horizontale windsnelheidsfluctuaties en uit de vlagerigheid van de wind hebben beide een groot brongebied en representeren daarom de grootschalige ruwheid van het gebied. De wrijvingscoëfficiënt wordt meer lokaal bepaald maar representeert nog steeds de grootschalige ruwheid wanneer de meting boven de lokale interne grenslaag plaatsvindt.

Veel van de metingen op 100 en 180 m hoogte zijn gedaan boven de oppervlaktelaag, waar de fluxen met de hoogte afnemen. Mede door de specifieke selectieprocedure die toegepast moest worden zijn voor de onstabiele grenslagen veel gevallen geselecteerd waarbij “entrainment” een grote rol speelt. Dit treedt op wanneer zich 's morgens een dunne, onstabiele grenslaag ontwikkelt nadat 's nachts een stabiele grenslaag is gevormd. Ook hierdoor nemen de fluxen af met de hoogte. Desondanks blijken de flux-profiel relaties die voor stationaire “constante-flux” grenslagen gelden ook in deze situaties nog redelijk te voldoen. Wel is het zo dat de normale flux-profiel relaties aanzienlijk beter opgaan wanneer lokale schaling wordt toegepast. Dat wil zeggen dat de profielen niet worden geschaald met

de oppervlaktefluxen, zoals gebruikelijk, maar met de fluxen op de meethoogte.

Hoofdstuk 4 en 5 gaan over de interpretatie en de schatting van de lokale windsnelheid. De meting van de oppervlaktewind wordt sterk beïnvloed door de bovenwindse ruwheid. Hierdoor is het mogelijk dat twee anemometers zeer verschillende windsnelheden rapporteren zonder dat ze ver van elkaar verwijderd zijn. Dit is een probleem wanneer men het windklimaat probeert af te leiden uit metingen van oppervlaktewind. Het is echter mogelijk te corrigeren voor de invloed van de bovenwindse ruwheid wanneer deze bekend is. Een methode om de ruwheid te bepalen die toegepast kan worden op standaard KNMI meetlocaties is de vlaaganalyse. De vlagerigheid geeft het verloop van de ruwheid als functie van de tijd en windrichting weer. Deze methode wordt al jaren op het KNMI toegepast om de gemeten wind te corrigeren. Het oude vlaagmodel (van Wieringa) sloot echter niet meer aan bij de recente meetmethoden en een nieuw model werd ontwikkeld (door Beljaars). Om te voorkomen dat door de introductie van het nieuwe model een breuk zou ontstaan in de gecorrigeerde windsnelheden, zijn het oude en nieuwe model uitvoerig onderling vergeleken (hoofdstuk 4).

Hieruit is gebleken dat voor uur-registraties de correcties van Wieringa's en Beljaars' model overeenkomen voor gladde terreinen. Over ruwe terreinen levert Beljaars' model kleinere correcties. De verschillen kunnen oplopen tot 10%. Voor 10-minuten registraties zijn de correcties van Beljaars' model 3 tot 10% kleiner dan die van Wieringa. Andere onzekerheden die resulteren uit aannames omtrent de stabiliteit van de atmosfeer en menighoogte zijn kleiner dan 5%.

Huidige numerieke weermodellen zijn niet in staat details van de stroming weer te geven kleiner dan  $\sim 10$  km. Dat heeft tot gevolg dat de wind in weermodellen één en dezelfde waarde heeft binnen een gebied van  $(10 \text{ km})^2$ . In werkelijkheid kunnen binnen zo'n gebied zeer veel verschillende landgebruikstypes aanwezig zijn met hun eigen ruwheid en windsnelheid. Moderne satellieten kunnen gegevens leveren over landgebruik tot op een resolutie van  $\sim 10$  m. Met behulp van deze informatie is het mogelijk zeer gedetailleerde ruwheidskaarten te maken.

Hoofdstuk 5 beschrijft een manier waarop de wind van weermodellen kan worden gecorrigeerd voor de lokale ruwheid met behulp van deze kaarten. Er wordt gebruik gemaakt van een eenvoudig twee-lagen model van de atmosferische grenslaag. De twee lagen zijn de oppervlaktelaag en de Ekmanlaag, elk met hun eigen ruwheidsparameter. Dit model doet, in combinatie met de ruwheidskaarten, een nabewerking van de weermodelwind. Deze techniek wordt downscaling genoemd.

De ruwheidskaart wordt afgeleid uit de landgebruikskaart met behulp van de toepassing van een sterk vereenvoudigd model wat het brongebied van de ruwheid op een zekere locatie weergeeft. Het brongebied voor de oppervlaktelaag is klein en bevindt zich dichtbij, terwijl het brongebied voor de Ekmanlaag zich tot over een grote afstand uitstrekt. De ruwheidsparameters die op die manier afgeleid zijn, zijn vergelijkbaar met waarden die volgen uit een vlaaganalyse. De ontwikkeling van de windsnelheid na een ruwheidsovergang is vergelijkbaar die in interne grenslaag modellen.

De wind van het weermodel en van de downscaling zijn vergeleken met metingen van de wind in het kustgebied, de Westerschelde en op Schiphol. Hieruit blijkt dat de downscaling de gemiddelde fout in de weermodelwind sterk reduceert. Dit blijkt echter wel sterk afhankelijk te zijn van de kwaliteit van de landgebruikskaart: fouten in het landgebruik laten zich gelden als fouten in de downscaling wind.



# Curriculum Vitae

Ik, Jacobus Wouter Verkaik werd geboren op 21 augustus 1969 te Mijdrecht. Ik heb daar de basisschool “De Hoeksteen” doorlopen en de Havo en het Atheneum van “Het Veenlandencollege”.

Van september 1988 tot maart 1994 heb ik gestudeerd aan faculteit natuur- en sterrenkunde van de Vrij Universiteit te Amsterdam. Als student heb ik mij eerst gericht op de experimentele fysica in verschillende vakgebieden. Als bijvak heb ik micro-meteorologie gekozen. Later ben ik afgestudeerd in de werkgroep astronomie op het onderwerp “De spectrale helderheid van horizonlicht”, hetgeen inhield het doen van berekeningen aan de meervoudige verstrooiing van licht in de aardatmosfeer.

Van juni 1994 tot mei 1998 heb ik gewerkt als Onderzoeker in Opleiding aan de vakgroep meteorologie van de Wageningen Universiteit. Als promovendus heb ik onderzoek gedaan aan de atmosferische grenslaag bij de Cabauw mast van het KNMI. De eerste helft van dit proefschrift is daar het resultaat van.

Van mei 1998 tot juli 2001 heb ik gewerkt aan het Hydra-project op het KNMI te De Bilt. Het belangrijkste doel van het Hydra-project was te komen tot een nieuwe beschrijving van het Nederlandse windklimaat ten behoeve van risicoanalyse in de kustzone. De tweede helft van dit proefschrift is daar het resultaat van.

Vanaf juli 2001 heb ik als “wetenschappelijk beheerder klimatologische gegevens” gewerkt bij de Klimatologische Dienst van het KNMI.